modelling

MDPI

Article

Convergence and Stability Analysis of Diametrical Compression in a Linear Elastic Disk Using Smoothed Particle Hydrodynamics

Luis F. Pérez [1,*], Ignacio Carvajal-Mariscal [1], Leonardo Di G. Sigalotti [2,*] and Jaime Klapp [3]

[1] Posgrado en Ingeniería Mecánica, ESIME Zacatenco, Instituto Politécnico Nacional, Av. IPN S/N, Ciudad de México 07738, Mexico; icarvajal@ipn.mx
[2] Departamento de Ciencias Básicas, Universidad Autónoma Metropolitana, Unidad Azcapotzalco (UAM-A), Av. San Pablo 420, Colonia Nueva el Rosario, Alcaldía Azcapotzalco, Ciudad de México 02128, Mexico
[3] Departamento de Física, Instituto Nacional de Investigaciones Nucleares (ININ), Carretera México-Toluca km. 36.5, La Marquesa, Ocoyoacac 52750, Mexico; jaime.klapp@inin.gob.mx
* Correspondence: lperezp2104@alumno.ipn.mx (L.F.P.); leonardo.sigalotti@gmail.com (L.D.G.S.)

Abstract

This work evaluates total Lagrangian Smoothed Particle Hydrodynamics (SPH) in DualSPHysics on a polycarbonate disk under diametrical compression against the Hondros analytical solution and two photoelastic experiments, with the stresses measured once the disk comes to rest. Stability tests reveal a broad optimal range of artificial viscosity above a stability threshold, within which the choice rests mainly on computational cost. A two-decade variation in piston velocity changes the error by at most 1.1%, and hourglass control reduces it by a factor of 7.3–8.5. A Convergence map of 6438 simulations across varying smoothing-length ratios, particle spacings and three kernels indicates that the von Mises error converges to first order in the smoothing length, down to 0.0026–0.0030 at the finest resolution. There, the contact zones account for 51–78% of the total error. Away from contacts, SPH interpolation of the exact field converges to second order, whereas the full simulation remains near first order. Finally, a single staged simulation reproduces the fringe patterns of four experimental photographs, matching dark fringes within 0.07–0.96 mm on average. Thus, concentrated contact loads govern both the error magnitude and, for interpolation, its convergence order. These findings guide SPH simulations of contact-loaded engineering structures.

Keywords: smoothed particle hydrodynamics; convergence; solid dynamics; contact mechanics

Check for updates

Academic Editor: Wei Gao

Received: 3 September 2026
Revised: 28 October 2026
Accepted: 29 October 2026
Published: 31 October 2026

Copyright: © 2026 by the authors. Licensee MDPI, Basel, Switzerland. This article is an open access article distributed under the terms and conditions of the Creative Commons Attribution (CC BY) license.

1. Introduction

Smoothed Particle Hydrodynamics (SPH) is a mesh-free, fully Lagrangian numerical method originally introduced in 1977 by Lucy [1] and Gingold and Monaghan [2] for astrophysical applications. In SPH, the computational domain is discretized into a collection of material points (particles), and the relevant physical fields are reconstructed through kernel-based interpolation over each particle's neighborhood. The influence of neighboring particles is weighted by a Gaussian-like kernel function that depends on the interparticle distance and confines the interactions within a support radius proportional to a characteristic smoothing length, h [3,4].

Traditionally, mesh-based techniques such as the finite element method (FEM) and the finite difference method have been widely used in structural simulations because of their high-order accuracy, computational efficiency and flexibility [5,6]. However, since the

pioneering SPH studies on elastic media by Benz and Asphaug [7], Monaghan [8] and Gray et al. [9], the method has been increasingly applied to the simulation of elastic, hyperelastic, plastic and fracture processes [10,11] and to fluid–structure interaction [12–14]. Owing to its fully Lagrangian formulation, SPH offers clear advantages for problems involving large deformations and complex geometries, while avoiding the substantial remeshing costs typically required by mesh-based approaches [3,15].

Despite its advantages, standard SPH suffers from several well-documented numerical deficiencies, including inconsistency, tensile instability and zero-energy modes [16]. Inconsistency can be alleviated through corrective formulations such as the Corrective Smoothed Particle Method (CSPM), which enhance solution accuracy, particularly near boundaries [17,18]. Tensile instability may be mitigated by adopting a total Lagrangian formulation, where all elastic quantities are evaluated with respect to the reference configuration [19]. Zero-energy modes are a consequence of rank deficiency: they arise from the non-uniqueness of particle arrangements in representing spatial derivatives within the support domain [20,21]. These spurious modes can be effectively controlled using the stabilization approach proposed by Ganzenmüller [21], which is analogous to hourglass control in the finite element method. Furthermore, several studies [22,23] have emphasized the strong coupling between the smoothing length and the spatial resolution in determining the total numerical error, so a careful, case-dependent parameter selection is required. In addition, high-frequency noise and residual vibrations can be attenuated with artificial viscosity, which provides controlled numerical dissipation.

Applications of SPH to elastic solids and structures [24] include hydroelastic fluid–structure interaction in ocean engineering [25] and soil–structure interaction [26]. Many such problems involve concentrated contact loads, as in indentation [27], contact between deformable bodies [28] and the Hertzian contact of grains [29].

The influence of smoothing length and kernel choice on SPH accuracy has been examined for smooth, continuous fields [22,23,30]. Elastic solid modeling has mainly addressed transient collisions, impact problems, fluid–solid interaction and crack propagation [31–33], and the Brazilian test has been used to validate stress boundary conditions [34]. However, the combined effect of convergence, stability and localized stresses under sustained contact loading remains largely unexplored.

This work investigates the mechanical response of a thin polycarbonate disk under diametrical compression between a fixed support and a moving piston with a steel tip, and benchmarks the SPH predictions against the analytical plane-stress solution. This configuration is a classical validation problem that has been extensively analyzed both theoretically and experimentally, including through photoelasticity [35–37]. In contact mechanics, the stress field of a concentrated line load on an elastic half-plane, the two-dimensional Flamant problem, has a first-order singularity at the load point [38]. Because SPH interpolation smooths the field, accuracy is expected to deteriorate near the contacts. We hypothesize that the concentrated contact loads degrade the theoretical second-order convergence of the SPH interpolation, and test it on the SPH operator applied to the exact field and on the full simulation. The present work aims to quantify this error and characterize its dependence on the loading rate and the governing numerical parameters: kernel, smoothing length, artificial viscosity, hourglass control and spatial resolution.

The simulations were performed with a modified version of DualSPHysics 5.2, which was ported to support AMD GPUs. It is an open-source, hardware-accelerated SPH code originally developed for free-surface flow simulations on parallel CPU/GPU architectures and implemented in C++ [39]. The work of Crespo et al. [40] provided its first stable implementation on NVIDIA GPUs using CUDA technology. The neighbor search uses a parallel variant of the Cell Linked List method, in which the domain is partitioned into square cells,

each interacting only with itself and its neighboring cells. Further implementation details are provided in Domínguez et al. [41].

The remainder of the paper is organized as follows. Section 2 describes the numerical formulation for elastic media, the analytical solution and the underlying SPH algorithms. Section 3 presents the physical configuration, the threshold that defines the rest stage of the simulations, and the test cases considered, together with the validation against the analytical solution and two photoelastic experiments. Section 4 reports and discusses the numerical results, with emphasis on the accuracy, stability and validation of the method. Supplementary technical details and data are given in the Appendices. Appendix A presents the three interpolating kernels, while Appendix B derives the half-width of the loaded arcs for the analytical solution based on the disk particles transmitting the wedge loads. Appendix C demonstrates that the rows used for load measurement carry equal force, and Appendix D details the disk lattice at the contact points. Finally, Appendix E provides supplementary stability test results and decay times across the Convergence map, Appendix F gives the minimum stable α, Appendix G evaluates convergence sensitivity to the analytical solution and Appendix H defines the color scales used in the simulated images.

2. Governing Equations and Constitutive Relations

Within a total Lagrangian framework [19], the governing equation for momentum conservation in elastic media is expressed as:

$$\frac{D\mathbf{v}}{Dt} = \frac{1}{\rho_0}\nabla_0 \cdot \mathbf{P}, \tag{1}$$

where ρ_0 is the reference density, $\mathbf{v}$ the velocity, t the time and D/Dt the material derivative. The subscript 0 denotes the reference configuration. The first Piola–Kirchhoff stress tensor, $\mathbf{P}$, is given by:

$$\mathbf{P} = \mathbf{F}\,\mathbf{S}, \qquad \mathbf{F} = \nabla_0 \mathbf{x}, \tag{2}$$

where $\mathbf{F}$ is the deformation gradient tensor, $\mathbf{x}$ and $\mathbf{x}_0$ are the current and reference positions, and $\mathbf{S}$ is the second Piola–Kirchhoff stress tensor. For small strains, the plane-stress law is linear [42]:

$$\mathbf{S} = \mathbf{C} : \mathbf{G}, \qquad \mathbf{C} = E^* \begin{bmatrix} 1 & \nu & 0 \\ \nu & 1 & 0 \\ 0 & 0 & \frac{1-\nu}{2} \end{bmatrix}, \qquad \mathbf{G} = \frac{1}{2}(\mathbf{F}^T\mathbf{F} - \mathbf{I}), \qquad E^* = \frac{E}{1-\nu^2}, \tag{3}$$

where $\mathbf{C}$ is the isotropic stiffness tensor, which in Voigt notation acts on $(G_{xx}, G_{zz}, 2G_{xz})$; $\mathbf{G}$ is the Green–Lagrange strain, $\mathbf{I}$ the identity tensor, E the Young modulus, ν the Poisson ratio and E^* the plane-stress modulus. In DualSPHysics, $\mathbf{C}$ is the in-plane block of a 6×6 Voigt matrix whose other entries are zero. The two-dimensional simulations were performed in the XZ plane.

2.1. Analytical Solution

For a disk of radius R and thickness b loaded over two opposite arcs of half-angle ψ centered on the loading axis, Z, each arc, of half-width $R\psi$, represents a wedge-disk contact region. The radial pressure on each arc, χ, transmits the normal load on the disk, F_N, as:

$$\chi = \frac{F_\mathrm{N}}{2Rb\sin\psi}. \tag{4}$$

This pressure generates a stress field given by the solution of Hondros [35]:

$$\begin{aligned}
\sigma_r &= -\frac{2\chi}{\pi}\left\{\psi + \sum_{n=1}^{\infty}\left[1-\left(1-\frac{1}{n}\right)\left(\frac{r}{R}\right)^2\right]\left(\frac{r}{R}\right)^{2n-2}\sin(2n\psi)\,\cos(2n\theta)\right\},\\
\sigma_\theta &= -\frac{2\chi}{\pi}\left\{\psi - \sum_{n=1}^{\infty}\left[1-\left(1+\frac{1}{n}\right)\left(\frac{r}{R}\right)^2\right]\left(\frac{r}{R}\right)^{2n-2}\sin(2n\psi)\,\cos(2n\theta)\right\},\\
\sigma_{r\theta} &= \frac{2\chi}{\pi}\sum_{n=1}^{\infty}\left[1-\left(\frac{r}{R}\right)^2\right]\left(\frac{r}{R}\right)^{2n-2}\sin(2n\psi)\,\sin(2n\theta),
\end{aligned} \tag{5}$$

where r is the distance from the center, θ the polar angle from the loading axis, n the index of the series and σ_r, σ_θ and $\sigma_{r\theta}$ are the polar components of the Cauchy stress tensor. This tensor follows from $\mathbf{P}$ and the Jacobian determinant J of $\mathbf{F}$ as

$$\boldsymbol{\sigma} = \frac{1}{J}\mathbf{P}\mathbf{F}^T, \qquad J = \det(\mathbf{F}). \tag{6}$$

In plane stress, the von Mises stress, σ_{vM}, is related to the principal stresses σ_1 and σ_2 by

$$2\,\sigma_{\mathrm{vM}}^2 = (\sigma_1-\sigma_2)^2 + \sigma_1^2 + \sigma_2^2. \tag{7}$$

The series expansions of Equation (5) are geometric and logarithmic in $\hat{r}^2 w_\pm$, with $\hat{r} = r/R$, $w_\pm = e^{2\mathrm{i}(\theta\pm\psi)}$ and i denoting the imaginary unit. They are summed exactly and the analytical values in this work are computed with the following closed form:

$$\begin{aligned}
\sigma_r &= -\frac{2\chi}{\pi}\left[\psi + \left(1-\hat{r}^2\right)S_0 + S_1\right], & S_0 &= \frac{1}{2}\,\mathrm{Im}\left[\frac{w_+}{1-\hat{r}^2 w_+} - \frac{w_-}{1-\hat{r}^2 w_-}\right],\\
\sigma_\theta &= -\frac{2\chi}{\pi}\left[\psi - \left(1-\hat{r}^2\right)S_0 + S_1\right], & S_1 &= \frac{1}{2}\,\mathrm{Im}\left[\ln\frac{1-\hat{r}^2 w_-}{1-\hat{r}^2 w_+}\right],\\
\sigma_{r\theta} &= \frac{2\chi}{\pi}\left(1-\hat{r}^2\right)T_0, & T_0 &= \frac{1}{2}\,\mathrm{Re}\left[\frac{w_-}{1-\hat{r}^2 w_-} - \frac{w_+}{1-\hat{r}^2 w_+}\right].
\end{aligned} \tag{8}$$

2.2. SPH Discretization

The SPH discretizations of the momentum equation and the deformation gradient tensor for particle i, using the kernel W^{ij}, are given by:

$$\frac{D\mathbf{v}^i}{Dt} = \frac{1}{m^i}\mathbf{f}^i_{\mathrm{HG}} + \sum_j m^j\left(\frac{\mathbf{P}^i\,(\boldsymbol{\Gamma}_0^i)^{-1}}{(\rho_0^i)^2} + \frac{\mathbf{P}^j\,(\boldsymbol{\Gamma}_0^j)^{-1}}{(\rho_0^j)^2}\right)\cdot\nabla_0^i W_0^{ij} - \sum_j m^j\,\Pi^{ij}\,\nabla^i W^{ij}, \tag{9}$$

$$\mathbf{F}^i = \sum_j \frac{m^j}{\rho_0^j}\mathbf{x}^{ji}\otimes(\boldsymbol{\Gamma}_0^i)^{-1}\nabla_0^i W_0^{ij}, \tag{10}$$

where m^i is the mass of particle i, $\mathbf{f}^i_{\mathrm{HG}}$ is the hourglass control term used to suppress the zero-energy (rank-deficiency) modes [21], $\mathbf{x}^{ji} = \mathbf{x}^j - \mathbf{x}^i$ is the separation vector of particles i and j, $\mathbf{x}^{ij} = -\mathbf{x}^{ji}$, $x^{ij} = |\mathbf{x}^{ij}|$ is the interparticle distance, $\mathbf{v}^{ij} = \mathbf{v}^i - \mathbf{v}^j$ is the relative velocity between particles and $\boldsymbol{\Gamma}_0^i$ is the correction matrix. The artificial viscosity term, Π^{ij}, is given by [43,44]:

$$\Pi^{ij} = -\frac{\alpha c_0 \mu^{ij}}{\bar{\rho}^{ij}}, \qquad \mu^{ij} = h\frac{\mathbf{v}^{ij}\cdot\mathbf{x}^{ij}}{(x^{ij})^2 + 0.01h^2}, \tag{11}$$

where α denotes the artificial viscosity coefficient, $\bar{\rho}^{ij} = (\rho^i + \rho^j)/2$ is the pair-averaged density, $c_0 = 5000$ m s^{-1} is a numerical reference sound speed, not a property of the disk, h is the smoothing length and $\nabla^i W^{ij}$ is the kernel gradient in the current configuration,

without the correction matrix. The viscous term uses the current positions and densities, $\rho^i = \rho_0^i / J^i$, and corresponds to an artificial kinematic viscosity

$$\alpha_{\text{eff}} = \frac{\alpha\, c_0\, h}{8} \tag{12}$$

in two dimensions [3], which damps the velocity differences between neighboring particles.

To restore first-order consistency of the kernel gradient near the boundaries of structural bodies, the correction matrix is formulated in the reference configuration [45]:

$$\boldsymbol{\Gamma}_0^i = \sum_j \frac{m^j}{\rho_0^j} \mathbf{x}_0^{ji} \otimes \nabla_0^i W_0^{ij}. \tag{13}$$

The hourglass control term adopted in this work follows the formulation of Ganzenmüller [21] and is expressed as:

$$\mathbf{f}_{\text{HG}}^i = -\frac{1}{2}\, \gamma_{\text{HG}}^i\, E^i \sum_j \frac{m^i\, m^j\, W^{ij}}{\rho_0^i \rho_0^j\, (x_0^{ij})^2} \left(\delta_i^{ij} + \delta_j^{ij}\right) \frac{\mathbf{x}^{ij}}{x^{ij}}, \tag{14}$$

$$\delta_i^{ij} = \left(\mathbf{x}^{ij} - \mathbf{F}^i\, \mathbf{x}_0^{ij}\right) \cdot \frac{\mathbf{x}^{ij}}{x^{ij}}, \tag{15}$$

where δ_j^{ij} is obtained in the same way with $\mathbf{F}^j$; E^i and γ_{HG}^i are, respectively, the Young modulus and the hourglass control coefficient, γ_{HG}, of the body of particle i. Following O'Connor and Rogers [46], W^{ij} is evaluated at the current configuration.

The structural particles are advanced with a symplectic predictor–corrector scheme [46], which evaluates the acceleration $\mathbf{a}^i = D\mathbf{v}^i/Dt$ twice per time step. Stability of this explicit scheme requires an adaptive time step [47], set by the acceleration (Δt_a), acoustic–viscous (Δt_{cv}), structural (Δt_{s}) and viscous (Δt_α) limits:

$$\Delta t_a = \min_i \left\{ \sqrt{\frac{h}{|\mathbf{a}^i|}} \right\}, \qquad \Delta t_{\text{s}} = \frac{h}{c'_{\text{s}}}, \qquad c_{\text{s}}'^{\,i} = c_{\text{s}}^i \left(1 + \gamma_{\text{HG}}^i\right)^{1/2}, \tag{16}$$

$$\Delta t_{\text{cv}} = h \min_i \left\{ c_0 + h \max_j \left(\frac{\mathbf{v}^{ij} \cdot \mathbf{x}^{ij}}{(x^{ij})^2 + 0.01 h^2} \right) \right\}^{-1}, \qquad \Delta t_\alpha = \frac{1}{8}\frac{h^2}{\alpha_{\text{eff}}} = \frac{h}{\alpha\, c_0}, \tag{17}$$

$$\Delta t = \max[\Delta t_{\min},\, \min(C_{\text{CFL}} \min(\Delta t_a, \Delta t_{\text{cv}}, \Delta t_{\text{s}}),\, \Delta t_\alpha)], \tag{18}$$

where $\Delta t_{\min} = 0.01\, h / c'_{\text{s}}$ is a numerical lower bound that prevents the step from vanishing, ρ_0^i and ν^i are the reference density and Poisson ratio, C_{CFL} is the Courant number, $(c_{\text{s}}^i)^2 = E^i / [\rho_0^i (1 - (\nu^i)^2)]$ is the plane-stress speed of sound of particle i and $c'_{\text{s}} = \max_i c_{\text{s}}'^{\,i}$. Because the hourglass force in Equation (14) is proportional to $\gamma_{\text{HG}}^i E^i$, the time step treats $E^i(1 + \gamma_{\text{HG}}^i)$ as the effective Young modulus for the particle-scale modes stiffened by the control. Thus, $c_{\text{s}}'^{\,i}$ estimates the speed of these controlled modes, whereas c_{s}^i is the speed of sound of the material alone. Δt_α is the diffusive stability limit of Morris et al. [48] for the explicitly integrated viscous term of Equation (11), and it is not multiplied by C_{CFL}.

Three kernels are compared: the cubic spline [49], the Wendland C^2 [50] and the hyperbolic kernel [51]. The first two are among the most widely used in the literature [52]. The hyperbolic kernel has a non-negative second derivative, which, according to the stability analysis of Swegle et al. [16], stabilizes particle motion under the high compression that dominates near the contacts of the loaded disk [51]. The kernel expressions are given in Appendix A.

Convergence

For a given initial interparticle spacing, Δp, the smoothing length is defined by:

$$h = \beta \, \Delta p, \tag{19}$$

where β sets the number of neighbors, n_{nb}, within the support radius $k\,h$, with $k = 2$ for the three kernels considered. Zhu et al. [22] and Sigalotti et al. [23] showed that the total error depends strongly on the number of particles, N, the number of neighbors and the particle distribution. The theoretical consistency of SPH requires the simultaneous limits $N \to \infty$, $h \to 0$, and $n_{\mathrm{nb}} \to \infty$ to be satisfied.

For uncorrected kernels, branches of constant β in the β–Δp map reach a floor below which the error cannot decrease. The correction matrix of Section 2.2 makes the kernel gradient exact for linear fields and should remove the zeroth-order error term that sets this floor along these branches (Section 7 of Zhu et al. [22]). Section 4.2 tests whether such a floor appears.

As the loaded arcs of the Hondros solution narrow, the pressure χ from Equation (4) scales as $1/\psi$. This creates a stress concentration that a kernel with a support radius of kh cannot resolve. Local stresses of order $F_{\mathrm{N}}/(bh)$ over an area of order h^2 thus introduce a relative error term of order h/R per contact. This term decays more slowly than the interpolation error away from the contacts, which decreases as h^{ζ}, where ζ is the convergence order ($\zeta = 2$ for standard kernel interpolation of a smooth field). These contact-induced errors are therefore expected to dominate at small Δp.

3. Methodology

The elastic bodies are modeled with FlexStruc, the module for flexible structures of DualSPHysics [46]. It uses two particle sets: *flexstruct* particles, which carry the elastic quantities of Section 2, and *clamp* particles, which impose fixed or moving displacements on the flexstruct bodies attached to them.

3.1. System Configuration

The studied system is a polycarbonate disk in the XZ plane, centered at the origin, without gravity, placed between two vertically aligned wedges: a fixed lower support and an upper piston with a steel tip that moves downward, as shown in Figure 1a.

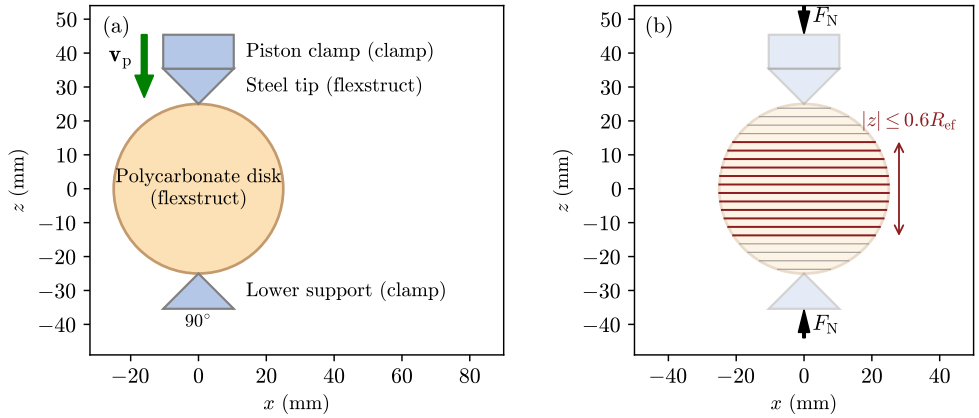


Figure 1. (**a**) Initial configuration in the XZ plane: polycarbonate disk, fixed lower support and piston clamp with steel tip moving downward at velocity $\mathbf{v}_{\mathrm{p}}$. (**b**) Horizontal rows of disk particles, drawn 2.5 mm apart; the load F_{N} is measured on the red ones, $|z| \leq 0.6R_{\mathrm{ef}}$, with R_{ef} the effective radius of Equation (21).

The disk has a radius $R = 25$ mm and nominal properties of polycarbonate, $E = 2.5$ GPa, $\nu = 0.38$ and $\rho = 1200$ kg m^{-3} [53]. It matches the disks of the two photoelastic experiments used later for validation: the polycarbonate disk of Lei et al. [36] and the disk of Wan et al. [37], printed in a resin with similar nominal constants [54]. The analytical solution does not depend on E or ν (Section 7.5 of Sadd [55]), but the dynamic response of the SPH model does, for instance, through the speed of the elastic waves.

The disk is modeled as a flexible structural body discretized with SPH particles. The lower support (clamp) is represented by a fixed, upward-pointing triangular boundary built on the particle lattice, with a 90° aperture, a base of 20 mm and a height of 10 mm. Its apex lies one Δp from the nearest particle of the disk. The steel tip of the piston, a flexible structural body, is an inverted triangle that mirrors the lower support. Its material properties are $E = 200$ GPa, $\nu = 0.25$, and $\rho = 7700$ kg m^{-3}. As no contact algorithm is used, the disk and the steel tip interact only through the particle pairs within each other's kernel support at $t = 0$, which transmit the load through a layer of one support radius $k\,h$ that sets the loaded arcs of the analytical solution (Appendix B). This coupling has no friction or contact law, and its pairs form a fixed list that is built at the start of the simulation and never updated, a limitation of the computational platform that hinders more dynamic contact models. The tip can still bend, slide or separate, which would invalidate a run if it were appreciable, and the settings used here keep this tip in place. The results therefore apply to contacts that neither slip nor separate, and frictional or sliding contacts would require an explicit contact algorithm. The disk is instead attached to the fixed particles of the lower support clamp, and the steel tip to the piston clamp. The piston clamp is a rigid rectangular body 10 mm tall that spans the base of the steel tip and translates vertically downward at a constant velocity $\mathbf{v}_\mathrm{p} = -v_\mathrm{p}\,\hat{\mathbf{z}}$ from $t = 0$ to t_p and then stays at rest. This motion is called the *push*. The piston displacement, $u_\mathrm{p} = v_\mathrm{p} t_\mathrm{p}$, is computed for each Δp so that F_N/b approaches 53.3 kN m^{-1} at the disk, equivalent to the 400 N that Wan et al. [37] applied to a disk 7.5 mm thick.

3.2. Amplitude of the Theoretical Solution

To compare the numerical solution with its analytical counterpart, the radial pressure on each loaded arc, χ, must be computed using the normal load, F_N, and the half-angle, ψ, as shown in Equation (4).

The load is measured in each simulation from the vertical force Q_ℓ across each horizontal row ℓ of disk particles, or chord, shown in Figure 1b:

$$Q_\ell = -b\,\Delta p \sum_{i \in \ell} P^i_{zz}, \qquad F_\mathrm{N} = \underset{|z| \le 0.6 R_\mathrm{ef}}{\mathrm{median}}\, Q_\ell, \tag{20}$$

where P^i_{zz} is the vertical normal component of the first Piola–Kirchhoff stress of particle i of row ℓ, Δp is the reference width of each particle along the row and b the thickness of the disk. Once the disk is nearly at rest, every chord away from the contacts transmits the same force: the reaction of the clamp support. The rows with $|z| \le 0.6 R_\mathrm{ef}$ are chords at least 0.8 diameters long. This band deliberately excludes the shorter rows near the contact points $(0, \pm R)$, where stresses concentrate and the rows intersect the layer bonded to each wedge; its choice is explained in Appendix C. Unlike the mean, the median stays within the range of the regular rows as long as fewer than half of the rows are anomalous [56].

In the discretization, the disk is filled with a rectangular grid of square cells of side Δp, with one particle at the center of each cell. For an arbitrary Δp, the ratio $R/\Delta p$ is not always a half-integer and the real edge of the discrete circle is not at R (see Appendix D). To improve the error estimation, an effective radius, R_ef, is measured directly from the

simulation. The edge of the disk lies $\Delta p/2$ (in the reference configuration) beyond its outermost particles, and R_{ef} is

$$R_{\mathrm{ef}} = \frac{z_{\max} - z_{\min}}{2} + \frac{\Delta p}{2}, \tag{21}$$

where $z_{\max}/z_{\min}$ are the reference positions of the highest/lowest disk particles which lie on the loading axis. R in Equations (4), (5), (8) and (A6) stands for R_{ef}.

A perfect circle and a sharp triangular tip are rounded off at the scale of the initial interparticle spacing, Δp, which fixes the spatial resolution. As a result, wedge-disk contacts have a finite width and can be modeled by the half-width of the Hondros [35] arc, $R_{\mathrm{ef}}\psi \propto \Delta p$ at fixed β. The proportionality factor defines the dimensionless parameter ξ given by:

$$\xi = \frac{R_{\mathrm{ef}}\psi}{\Delta p}. \tag{22}$$

Because the apex of each wedge contains a single particle, a first estimate yields $\xi = 1/2$. However, this approximation assumes a hard-sphere contact system, whereas SPH inherently smooths the contact zones. This smoothing affects not only the surface particles but also the bulk ones as the kernel support radius, kh, increases. Therefore, ξ must be determined from the width of the disk particle layer; its computation is described in Appendix B.

3.3. Reading Threshold

The SPH predictions Φ_{n} are compared with the analytical von Mises stresses Φ_{t} (see Equation (7)) using a relative L_1 norm calculated over all disk particles i:

$$\varepsilon(\Phi) = \frac{\sum_{i\in\mathrm{disk}} \left|\Phi_{\mathrm{t}}^i - \Phi_{\mathrm{n}}^i\right|}{\sum_{i\in\mathrm{disk}} \left|\Phi_{\mathrm{t}}^i\right|}. \tag{23}$$

For each simulation, the analytical values come from the Hondros solution of Equation (5), with the radius R_{ef} of Equation (21), the load F_{N} of Equation (20) and the effective half-width $\xi\,\Delta p$ of Equation (A6).

The analytical solution is static, so this error is evaluated over the instants saved once the disk has come nearly to rest after the piston stops at t_{p}. How close the disk is to rest is measured by the dimensionless kinetic energy, the kinetic energy of the disk divided by its rigid-body value at piston velocity v_{p}:

$$\hat{K}(t) = \frac{K(t)}{\frac{1}{2}Mv_{\mathrm{p}}^2}, \qquad K = \frac{1}{2}\sum_{i\in\mathrm{disk}} m^i \left|\mathbf{v}^i\right|^2, \tag{24}$$

where $M = \rho_0\,\pi R^2$ is the mass of the disk per unit thickness. After the stop, the vertical velocity of the center of mass of the disk, v_{cm}, oscillates with period $T = 1/f$, where the frequency f is taken in each simulation from the peak of its Fourier spectrum. Owing to the artificial kinematic viscosity of Equation (12), $\hat{K}$ decays as it oscillates. The means $\bar{K}$ of $\hat{K}$ over consecutive windows of length T are free of the oscillation and decay exponentially; they are fitted with

$$\bar{K}(t) = \Theta\, e^{-(t-t_{\mathrm{p}})/\tau}, \tag{25}$$

where the amplitude Θ is the value of the fit at the stop and τ is the decay time of the kinetic energy. The rest time t_{r} is the time at which the fitted curve decays to the reading threshold of 0.01,

$$t_r = \begin{cases} t_p + \tau \ln\left(\dfrac{\Theta}{0.01}\right), & \Theta \geq 0.01, \\ t_p, & \Theta < 0.01, \end{cases} \tag{26}$$

and the instants saved in the interval $t_r \leq t \leq t_{end}$, with t_{end} the last saved instant, form the *rest stage*.

In the stability tests, ε is defined as the mean of its values across all saved instants of the rest stage, so t_r marks only the onset of this interval. For the Convergence map, the SPH and analytical fields, the latter built at each saved instant with the current load $F_N(t)$, are first averaged particle by particle over the rest stage, and ε is computed from these time-averaged fields.

A simulation whose fit $\bar{K}$ does not decay to 0.01 before t_{end} is called censored: it has no rest stage and is not used. Unless stated otherwise, the stresses are averaged over the outputs saved 0.05 ms apart in the rest stage.

The kinetic energy K is also compared with the internal energy of the disk per unit thickness,

$$U = \frac{1}{2} \sum_{i \in \text{disk}} \mathbf{S}^i : \mathbf{G}^i \, \frac{m^i}{\rho_0^i}. \tag{27}$$

The lower the ratio K/U, the closer the system is to mechanical equilibrium.

To ensure that evaluating the stresses during the rest stage does not introduce bias, the principal stress difference, the quantity measured via photoelasticity, is compared at each saved instant t with its value at the last saved instant, t_{end}, using the norm of Equation (23):

$$\Psi_\sigma(t) = \frac{\sum_{i \in \text{disk}} \left| \Delta\sigma^i(t) - \Delta\sigma^i(t_{end}) \right|}{\sum_{i \in \text{disk}} \left| \Delta\sigma^i(t_{end}) \right|}, \qquad \Delta\sigma = \sigma_1 - \sigma_2. \tag{28}$$

3.4. Tests

Each of the four tests varies one or more parameters relative to a reference configuration called the *baseline* and, unless stated otherwise, uses the three kernels described in Section 2.2. Three of them, the stability tests, share a baseline and verify that the state during the rest stage is close to equilibrium and independent of the loading path. They are also used to select α and γ_{HG}. In every simulation, the steel tip is assigned the same γ_{HG} value as the disk. The baseline resolution of the stability tests, $\Delta p = 0.4$ mm with $\beta = 1.04$, was selected through preparatory parametric sweeps of α, γ_{HG}, β and Δp. The fourth test—the Convergence map—consists of a joint sweep over β and Δp. Table 1 lists the parameters for both baselines, while Table 2 outlines the four test configurations, where the notation $[start, end, step]$ defines a range varying from start to end with an increment of step. Supplementary results for the stability tests are provided in Appendix E. Two further sets complement them: the Resolution–damping test, which repeats the Damping test at four resolutions (12 simulations, Appendix E), and short runs that check the stability limits of the time step (10 simulations, Section 4.1.1) and of α (588 simulations, Appendix F).

Table 1. Baseline parameters of the stability tests and of the Convergence map. With Wendland C^2 at $\beta \geq 1.5$, $C_{CFL} = 1$ made the disk unstable (Section 4.1.1).

Parameter	Stability Tests	Convergence Map
Δp (mm)	0.4	swept
$\beta = h/\Delta p$	1.04	swept
α	1.8	1.8
γ_{HG}, disk/steel tip	2/2	2/2
Push duration t_p (ms)	5	5

Table 1. *Cont.*

Parameter	Stability Tests	Convergence Map
Piston velocity v_p (mm s^{-1})	33.3	19.9–39.8
Displacement u_p (mm)	0.1665	0.0997–0.199
Target load F_N/b (kN m^{-1})	53.3	53.3
C_{CFL}; c_0 (m s^{-1})	1; 5000	0.95; 5000
Output interval (ms)	0.05	1, then 0.05 at rest

Table 2. Numerical tests: expected result, varied and fixed parameters, and number of simulations.

Name	Expected to Show	Varied	Fixed	Simulations
Damping test	α sets how fast the disk comes to rest	$\alpha \in [0.1, 0.8, 0.05] \cup \{0.9, 1.0, 1.1, 1.2, 1.5, 2, 3, 5\}$; three kernels	baseline of the stability tests	69
Loading-rate test	the state in the rest stage does not depend on the piston velocity	11 values of v_p, five per decade on a logarithmic scale, from 0.761 to 76.1 mm s^{-1}, so t_p from 218.8 to 2.19 ms; three kernels	$u_p = 0.1665$ mm; the others at the baseline of the stability tests	33
Hourglass test	the control lowers the error and stiffens the disk, without damping it; choice of γ_{HG}	γ_{HG} of the disk and the steel tip $\in [0, 0.3, 0.05] \cup [0.4, 0.6, 0.1] \cup \{0.8, 1, 1.5, 2, 3, 4, 5\}$; three kernels	baseline of the stability tests	51
Convergence map	the error against β and Δp; its order of convergence along branches of constant β	$\beta \in [0.54, 2.00, 0.02]$; 29 values of Δp from 0.15 to 3 mm; three kernels	baseline of the Convergence map	6438

3.5. Stability Tests

Artificial viscosity damps the vibration left in the structure by the push. Its magnitude typically requires case-by-case calibration [4], although values around $\alpha = 1$ are commonly used in fluid simulations [3]. For the hourglass control, Ganzenmüller [21] found $\gamma_{HG} = 50$ optimal for a beam in bending and O'Connor and Rogers [46] found an optimal value of $\gamma_{HG} = 0.1$ for fluid–structure interaction, but neither study calibrated it for the stress concentrations of contact problems. After the stop, the simulations continue for 16, 12 and 17 ms with the cubic spline, Wendland C^2 and hyperbolic kernels, respectively, in both the Loading-rate and Hourglass tests. In the Damping test, the remaining runtime ranges from 10 to 35 ms, scaling up as α decreases; it reaches up to 85 ms at the smallest values of α, where the simulations ultimately fail (Section 4.1.1).

3.5.1. Damping Test

The disk is modeled as purely elastic; consequently, once the piston stops, the artificial viscosity alone dissipates the kinetic energy induced by the initial loading. The Damping test sweeps α over the 23 values listed in Table 2 to measure how α sets the relaxation rate of the disk via the decay time τ (Equation (25)). The values from 0.1 to 0.8, evaluated at intervals of 0.05, are used to identify the stability threshold for α. Because α also constrains the viscous time step Δt_α in Equation (17), this test quantifies the computational cost of the simulation (compared in Appendix E) and ultimately guides the selection of α.

3.5.2. Loading-Rate Test

Under the baseline of the stability tests, the disk is loaded within $t_p = 5$ ms, a duration significantly shorter than that of the experiments it reproduces. Because the equilibrium state of an elastic disk is governed solely by displacement, the Loading-rate test verifies that the load, the resulting error and the final stress field within the rest stage remain independent of the loading velocity. This test sweeps v_p over two orders of magnitude

at a fixed displacement, as listed in Table 2. Each quantity is evaluated against that of the slowest push with the same kernel. The von Mises fields at the last saved instant are compared particle by particle with the norm of Equation (23):

$$\Psi_{\mathrm{vM}} = \frac{\sum_{i\in\mathrm{disk}} \left|\sigma^i_{\mathrm{vM}} - \sigma^i_{\mathrm{vM,ref}}\right|}{\sum_{i\in\mathrm{disk}} \left|\sigma^i_{\mathrm{vM,ref}}\right|}. \tag{29}$$

Here σ^i_{vM} and $\sigma^i_{\mathrm{vM,ref}}$ are the von Mises stresses of particle i in the compared simulation and in the slowest push.

3.5.3. Hourglass Test

The control term of Equation (14) suppresses zero-energy modes – the particle-scale patterns in which neighboring particles are displaced in alternating directions without changing the deformation gradient $\mathbf{F}^i$, so that no elastic force opposes them. Without the control, the error is therefore expected to be larger. Since the term depends only on the δ^{ij}_i and δ^{ij}_j (see Equation (15)), it vanishes for a homogeneous deformation and should stiffen the smooth deformation of the disk. It depends on the positions of the particles, not on their velocities, so it should not damp the disk. The Hourglass test sweeps γ_{HG} across the 17 values listed in Table 2, applying identical values to both the disk and the steel tip; the baseline γ_{HG} is subsequently selected based on these results.

3.6. Convergence Map

The Convergence map gives the relative L_1 error as a function of the smoothing-length ratio β and the initial interparticle spacing Δp, with the other parameters at its baseline in Table 1. It locates the optimal β at each Δp and measures the order of convergence along branches of constant β. Two practical relationships are considered: one linking N to Δp and another relating the number of neighbors n_{nb} to β:

$$N \approx \lfloor A_{\mathrm{eff}}/\Delta p^2 \rfloor, \tag{30}$$

$$n_{\mathrm{nb}}(d) \approx \lfloor \varsigma_d (k\beta)^d \rfloor, \tag{31}$$

where $A_{\mathrm{eff}} = 2113 \pm 49$ mm^2. This value, the mean and standard deviation of $N\,\Delta p^2$ over the spacings of the map, represents the effective area of the flexible particles (disk and steel tip) and ς_d is the volume of the unit ball in d dimensions ($\varsigma_1 = 2$, $\varsigma_2 = \pi$ and $\varsigma_3 = 4\pi/3$).

The von Mises stress field of the analytical solution has a stress concentration under the loaded arcs around $(0, \pm R)$. For a finite arc, it is bounded by the pressure χ (Equation (4)), which diverges as the arc narrows with Δp. The presence of these stress concentrations is expected to degrade the SPH accuracy and alter the order of convergence near the contacts, since most error analyses assume smooth fields [30].

The smoothing-length ratio is varied over $\beta \in [0.54, 2.00]$ in increments of 0.02, corresponding to a bulk neighbor count n_{nb} between 3 and 50. The initial interparticle spacing takes 29 values from 0.15 to 3 mm, which gives 246 to 9.2×10^4 particles. A β–Δp error map is generated for each kernel, yielding a total of 6438 simulations.

The simulations of the Convergence map save outputs 1 ms apart (Table 1) up to a final time beyond their rest time t_{r}, and are then continued at rest for at least 2 ms to read the stresses as in Section 3.3. Since α_{eff} (Equation (12)) is proportional to h, the disk takes longer to come to rest at fine resolutions. Every simulation is monitored to ensure it reaches the rest stage; any that fail to do so are resumed with an extended maximum duration.

The reading threshold is verified using Ψ_σ from Equation (28) across 441 simulations selected at random from the Convergence map. These simulations span the three kernels,

with ranges of $\beta = 0.72$–2.00 and $\Delta p = 0.15$–3.00 mm, and are restricted to cases that terminate with $\hat{K} \leq 0.003$. The evaluation encompasses a total of 4230 saved instants, 1 ms apart, recorded after the piston stops, with t_{end} in Equation (28) the last of each simulation.

The order of convergence is measured along three branches of constant β (equivalent to a constant number of neighbors), $\beta = 0.98$, 1.48 and 1.98, just below the values $\beta = 1$, 1.5 and 2 at which the support radius reaches an axial layer of the initial lattice and the error jumps (Section 4.2). Along each branch, the error of Equation (23) is fitted with a power of h plus a constant floor, $\varepsilon = \mathcal{A}\, h^{\zeta} + \varepsilon_{\infty}$. The disk is also split into contact zones, rim and interior by a distance set as a fixed fraction of R_{ef}. The order is then measured for each region and for the SPH operator applied to the exact displacement of the analytical solution, which isolates the interpolation error. Appendix G examines how the order changes when the analytical solution uses a loaded arc that does not depend on the discretization or another definition of its radius.

3.7. Validation

3.7.1. Theoretical Validation

The theoretical validation reveals the specific regions within the disk where the error $\varepsilon(\sigma_{\text{vM}})$ is most pronounced. For this analysis, a single simulation is used, with the hyperbolic kernel, $\beta = 1.28$, $\Delta p = 0.15$ mm and the other parameters at the baseline of the Convergence map in Table 1. Its outputs, 0.05 ms apart, are averaged from 22 to 25 ms after the piston first stops, when the disk is at rest at the load of the 400 N photograph of Wan et al. [37]. This averaged state is then compared against the analytical solution from Section 2.1 in terms of the global von Mises stress field, as well as through localized profiles. These profiles are extracted along the loaded diameter $x = 0$, the transverse diameter $z = 0$ and near the contact zones along both the axis and the boundary.

3.7.2. Experimental Validation

The simulated isochromatic fringes are compared independently of the analytical solution, with two photoelastic experiments on disks of the same diameter, 50 mm. Lei et al. [36] loaded a polycarbonate disk of thickness $b_{\text{e}} = 5$ mm, with a fringe value $f_{\sigma} = 7.334$ N mm^{-1}, and photographed it at 392 N. Wan et al. [37] loaded a disk of VeroClear™ resin, with $b_{\text{e}} = 7.5$ mm and $f_{\sigma} = 34.95$ N mm^{-1}, photographed it at 400, 800 and 1300 N and gave the profile of $\sigma_1 - \sigma_2$ along the horizontal diameter at 1300 N. In a circular dark-field polariscope, the fringe order and the transmitted intensity are

$$N_{\text{f}} = \frac{b_{\text{e}}\,(\sigma_1 - \sigma_2)}{f_{\sigma}}, \qquad \mathcal{I} = \sin^2(\pi N_{\text{f}}). \tag{32}$$

The intensity vanishes at the integer fringe orders and forms dark fringes. The simulated images show $\mathcal{I}$, with the b_{e} and f_{σ} of each experiment.

Since the stresses of a plane disk loaded only at its boundary do not depend on the elastic constants [57], one simulation of the polycarbonate disk serves both experiments, each at its load per unit thickness $F_{\text{e}}/b_{\text{e}}$, with F_{e} the load of the experiment. Its load is staged. The piston advances at 76.1 mm s^{-1}, stops for 25 ms while the disk comes to rest, and advances again. The load of Equation (20) thus holds plateaus close to 53.3, 78.4, 106.7 and 173.3 kN m^{-1}, equivalent to Wan et al. [37] at 400 N, Lei et al. [36] at 392 N and Wan et al. [37] at 800 and 1300 N, respectively. Each plateau is evaluated at a single saved instant, 0.25 ms before the end of its rest. The simulation is the one used in the theoretical validation.

Along two perpendicular diameters, the dark fringes of each photograph, the minima of its smoothed intensity numbered from the center, are compared with the positions where

the simulated order reaches the same integer. The whole disk is compared in images painted with the color scale of each photograph, extracted from the photograph itself; for the overexposed photograph of Lei et al. [36], the simulated image is drawn through a tone curve estimated from that photograph (Appendix H). At 1300 N the simulated $\sigma_1 - \sigma_2$ is also compared with the profile of Wan et al. [37], digitized from their Figure 12a.

3.8. Hardware

The simulations ran on a cluster with dual Intel(R) Xeon(R) Gold 6148 CPUs @ 2.40 GHz, 1024 GB of RAM, and 8x AMD Instinct^{TM} MI210 GPUs, with access provided by the Instituto Nacional de Investigaciones Nucleares (ININ) of Mexico.

4. Results and Discussion

This section gives the results of the stability tests, the Convergence map and the validation against the analytical solution and photoelastic experiments.

4.1. Stability Tests

4.1.1. Damping Test

For the cubic spline kernel (this behavior holds for the other kernels), the window means of $\hat{K}$ decay exponentially after the stop, faster at larger α: the rest stage starts at $t_r = 22.6$, 13.5 and 6.9 ms for $\alpha = 0.55$, 1.1 and 5, respectively, as shown in Figure 2. At t_r, where the fit of $\bar{K}$ has just fallen to 0.01, the kinetic energy is 3.2×10^{-6} of the internal energy from Equation (27), $U = 4.11$ J m^{-1}, the same for the three values of α, as seen in Figure 3a: the disk is effectively at rest.

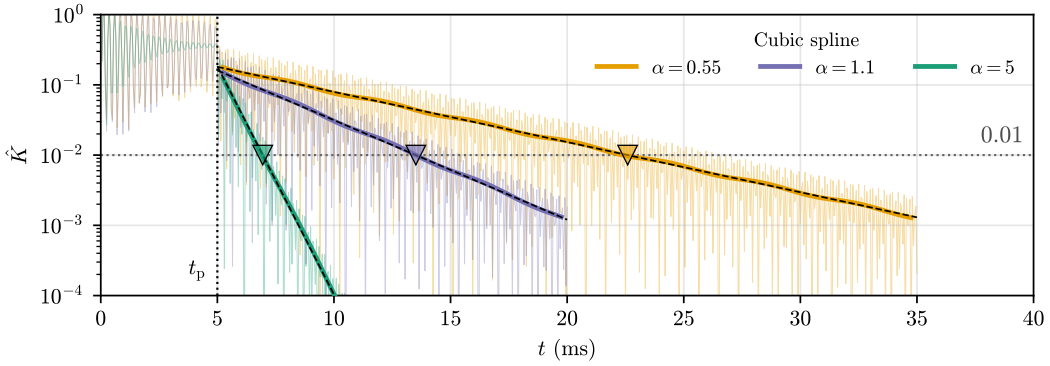


Figure 2. Damping test: cubic spline kernel at three values of α, the other parameters at the baseline of the stability tests. Dimensionless kinetic energy $\hat{K}$ against time t. $\hat{K}$ at every output (thin lines), its window means $\bar{K}$ (thick lines) and their exponential fits (black dashed lines). Vertical dotted line: piston stop, $t_p = 5$ ms. Horizontal dotted line: $\hat{K} = 0.01$; triangles: rest times t_r, start of the rest stage.

The decay rate $1/\tau$ grows linearly with α (Figure 3b),

$$\frac{1}{\tau} = \lambda_0 + \lambda_1 \alpha, \tag{33}$$

with slopes $\lambda_1 = 0.2964 \pm 0.0007$, 0.287 ± 0.006 and 0.2785 ± 0.0006 ms^{-1} for the cubic spline, Wendland C^2 and hyperbolic kernels, respectively, which differ by up to 6%. Since λ_0 is small (0.0012 ± 0.0006, 0.008 ± 0.005 and 0.0015 ± 0.0005 ms^{-1}, at most 2% of the decay rate at $\alpha = 1.8$), almost all the damping comes from the artificial viscosity.

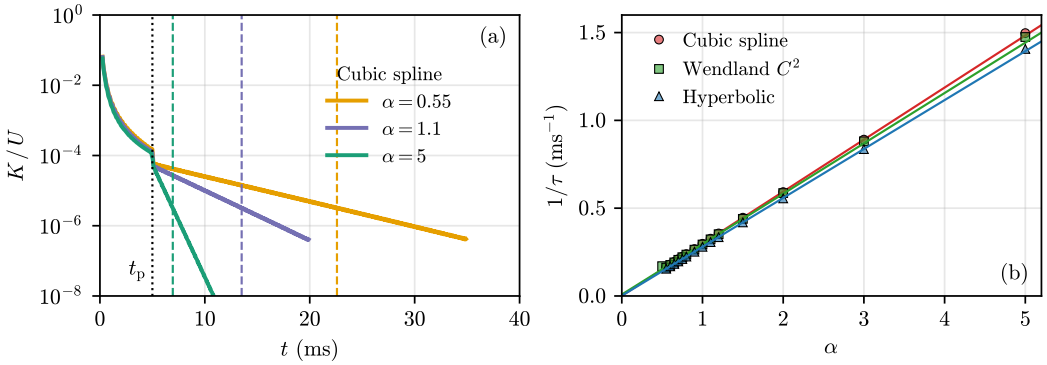


Figure 3. Damping test, continued. (**a**) Ratio of the kinetic to the internal energy of the disk, K/U, averaged over a sliding window one oscillation period long, against time t, on a logarithmic vertical axis, for the cubic spline kernel at the three α of Figure 2; vertical dotted line: piston stop; dashed vertical lines: t_r. (**b**) Decay rate after the piston stop, $1/\tau$, against α for the three kernels, at the values of α at which $\hat{K}$ decays after the stop; lines: linear fits.

The artificial viscosity is also needed for stability. Below $\alpha = 0.55$ with the cubic spline and hyperbolic kernels, and below $\alpha = 0.5$ with Wendland C^2, none of the 26 simulations of the Damping test come to rest. Of these, 20 abort between 0.08 and 56.5 ms, when the Jacobian J^i (Equation (6)) of a particle falls to $J^i \leq 0$; the other six become unstable during the push, with $\hat{K} > 10$ from 0.4–3.3 ms on and $\hat{K} = 3 \times 10^4$–8×10^5 at the end. In all 43 simulations at or above these thresholds, $\hat{K}$ decays exponentially after the stop, and the baseline, $\alpha = 1.8$, lies well above them.

In short runs at the baseline resolution, the lower stability limit for α grows roughly as $\gamma_{HG}/4$, almost equally for the three kernels (Appendix F). It also grows as the spacing is refined, roughly as $\Delta p^{-0.35}$ (Appendix F), as the Resolution–damping test of Appendix E suggests.

Positioned just below the computational-cost optimum given by the elbow $\alpha = c_s'/(C_{CFL} c_0)$ in Equation (A8), the baseline value of $\alpha = 1.8$ ensures that the viscous time step Δt_α (Equation (17)) remains only $c_s'/(C_{CFL} \alpha c_0) - 1 = 1.3\%$ above the Courant time step $C_{CFL} \Delta t_s$ (Equation (16)) at $C_{CFL} = 1$. $C_{CFL} = 1$ suffices at the baseline, $\beta = 1.04$, and for the cubic spline and hyperbolic kernels, but not for the Wendland C^2 kernel at $\beta \geq 1.5$. With that kernel, the disk becomes unstable within the first 0.1 ms at $\Delta p \geq 1.5$ mm, with $\hat{K}$ rising to 10^3–10^8, whereas at $\Delta p = 0.4$–0.8 mm, $\hat{K}$ peaks between 10 and 900 before decaying. Introducing a 6.6% safety margin by setting $C_{CFL} = 0.95$ ensures the stability of every case evaluated in the short runs. This includes the Wendland C^2 kernel at $\beta = 2$ for $\Delta p = 0.4$ to 2.5 mm. The Convergence map was therefore computed mostly with $C_{CFL} = 0.95$ (Table 1).

Across the full Convergence map, however, some simulations with the Wendland C^2 kernel at $\beta = 1.30$–1.72 reached the stability limit at $C_{CFL} = 0.95$, triggering element inversion ($J^i \leq 0$) or failing to reach the rest stage. Lowering the Courant number only shortens the time step and leaves the dynamics unchanged, so these simulations were rerun with $C_{CFL} = 0.80$, or with 0.60 at $\beta = 1.72$. Reaching the stability limit at these points is expected, since the settings of the map were estimated from power-law fits, whose errors leave some points of the β–Δp plane closer to that limit than predicted. The reruns are 205 of the 6438 simulations (3.2%); in all, 9.4% of the map ran with a Courant number below 0.95, and between 4.6% and 8.4% of the map is estimated to be unstable at $C_{CFL} \geq 0.95$.

Because the error during the rest stage is largely insensitive to α, as demonstrated by the Resolution–damping test in Appendix E, this parameter is selected by cost. The same appendix shows that the cost is minimized within the range $\alpha = 1.78$–1.85 when the steel

tip is set to $\gamma_{HG} = 2$. A baseline value of $\alpha = 1.8$ was therefore chosen, whereas a lower value of $\alpha = 1.1$ increases the cost by 37–41%.

4.1.2. Loading-Rate Test

Regardless of the piston velocity, the load scales proportionally with the piston displacement and stabilizes at the same plateau (Figure 4a). Its initial rise deviates from linearity by a mere 0.4–0.9% of the final load, while the results from the highest-velocity cases scatter around the slowest loading curve by at most 0.7%. The final load, computed as the mean over the last 1 ms, varies by less than 0.04% across the entire sweep; this minor discrepancy arises solely from the rounding of t_p, which slightly alters u_p (the load per unit displacement changes by less than 0.002%). During the rest stage at the baseline, for all three kernels, the forces Q_ℓ of the 75 rows within $|z| \leq 0.6R_{ef}$ deviate from their median F_N by no more than 0.2%, confirming that the disk has effectively reached mechanical equilibrium.

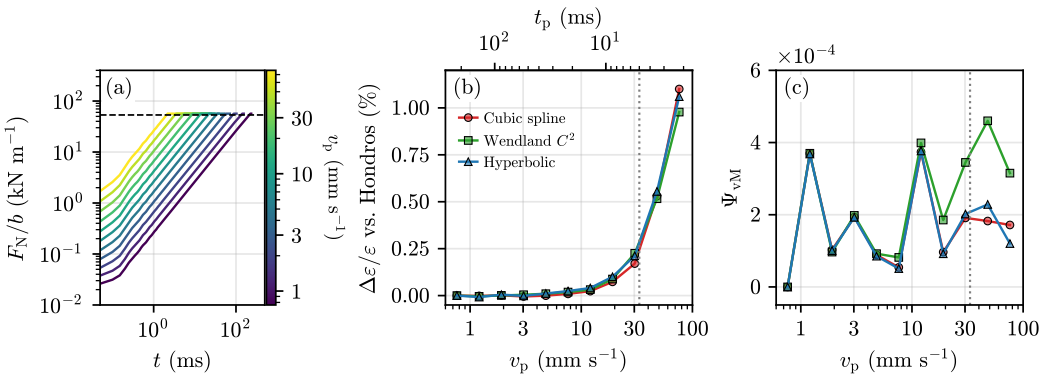


Figure 4. Loading-rate test: 11 piston velocities v_p from 0.761 to 76.1 mm s^{-1}, all with the displacement $u_p = 0.1665$ mm and the other parameters at the baseline of the stability tests. (**a**) Load per unit thickness, F_N/b, against time t for the cubic spline kernel. Color: v_p; dashed line: target load, 53.3 kN m^{-1}. (**b**) Change of the error $\varepsilon(\sigma_{vM})$ averaged from t_r, relative to the slowest push of each kernel, against v_p. (**c**) Same for the final von Mises field, Ψ_{vM}. Top axis of (**b**): push duration t_p; dotted vertical lines: baseline velocity.

The error changes by less than 0.03% up to 7.6 mm s^{-1} and by at most 1.1% over the sweep (Figure 4b), as obtained by the cubic spline kernel at 76 mm s^{-1}. Figure 4c shows that Ψ_{vM} (Equation (29)) is at most 4.0×10^{-4} up to 12 mm s^{-1}, comparable with the relative change of u_p caused by rounding t_p, 3.7×10^{-4}, and at most 4.6×10^{-4} over the sweep, as obtained by Wendland C^2 at 48 mm s^{-1}. The pushes of the Convergence map, listed in Table 1, lie within the swept range, although the test was run only at $\Delta p = 0.4$ mm and $\beta = 1.04$. Neither the error nor the stress field in the rest stage depends appreciably on v_p.

Because the piston velocity acts as a negligible factor across the swept range, its baseline value is selected strictly to optimize computational efficiency. For instance, a simulation requires approximately 2 h at 0.76 mm s^{-1} but only 6 to 9 min at 76 mm s^{-1}. Above approximately 30 mm s^{-1}, the wall-clock time stabilizes between 6.3 and 10.4 min at $\Delta p = 0.4$ mm. At these high values of v_p, the post-stop simulation phase ($t_{end} - t_p$) dominates the overall execution, causing the total computational cost to asymptotically approach a lower bound dictated by the duration of this stabilization period.

During the push, the center of mass of the disk follows the piston at $0.60\, v_p$ at every velocity (Figure 5a, three of the velocities), and over the second half of the pushes of 21.9 ms or longer this translation carries all but 0.012–0.014 of the kinetic energy. The mean of $\hat{K}$ there is 0.360–0.362, against $(v_{cm}/v_p)^2 = 0.356$–0.357 for a rigid translation; the disk moves almost as a rigid body.

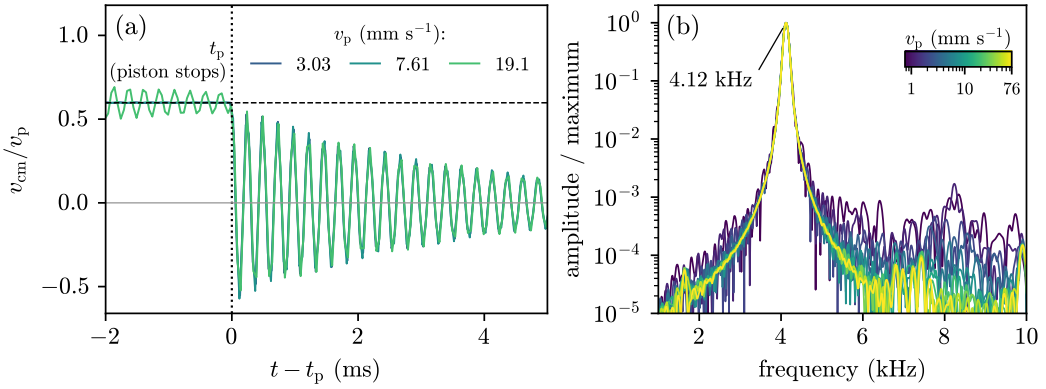


Figure 5. Oscillation of the disk in the Loading-rate test, cubic spline kernel. (**a**) Vertical velocity of the center of mass of the disk divided by the piston velocity, v_{cm}/v_p, against the time from the piston stop, $t - t_p$, at $v_p = 3.03$ (dark blue), 7.61 (teal) and 19.1 mm s^{-1} (green), colored as in (**b**). Dashed line: $v_{cm}/v_p = 0.60$; dotted vertical line: piston stop. (**b**) Fourier spectrum of v_{cm}/v_p after the stop, divided by its maximum, from 1 to 10 kHz (Nyquist limit for the time sampling), for the 11 velocities. Color: v_p, as in Figure 4a.

When the piston stops, the disk oscillates on its contacts at a single frequency, as Figure 5b shows for the cubic spline kernel. With the three kernels, the frequency is $f = 4.07$–4.12 kHz, the same at all eleven velocities within 0.3%. The kinetic energy metric $\hat{K}$ oscillates at $2f$, corresponding to the high-frequency oscillation observed in Figure 2. A single loading phase encompasses $n_T = f\,t_p$ periods: this ranges from 9 to 900 in the Loading-rate test, with $n_T \approx 20$ for the 5 ms push at the baseline, $\Delta p = 0.4$ mm, compared to $n_T \sim 10^6$ at the experimental rate of 0.05 mm min^{-1} ([37], Section 2.2).

The primary artifact of the loading rate is the residual oscillation remaining after the piston stops, which is subsequently dissipated by the artificial viscosity. Its amplitude Θ is 0.11–0.19 for $n_T \gtrsim 56$, but fluctuates between 0.035 and 0.34 for the shorter, faster pushes. There, the oscillations excited at the start of the push have not yet decayed at t_p, so they add to those excited at the stop, reinforcing or partly canceling them depending on the exact value of n_T. At the baseline ($n_T \approx 20$), $\Theta = 0.16$–0.28.

4.1.3. Hourglass Test

The hourglass control term of Equation (14) reduces the error by a factor of 7.3–8.5 at $\gamma_{HG} = 2$ relative to $\gamma_{HG} = 0$, and by 7.1–8.9 over the whole range from 2 to 5 (Figure 6a). Most of this improvement is already achieved at $\gamma_{HG} = 0.5$. In contrast, at $\gamma_{HG} = 0.1$, the optimal value reported by O'Connor and Rogers [46] for fluid–structure interaction, the error is still 2.1–2.6 times higher than at $\gamma_{HG} = 2$. Furthermore, the Wendland C^2 kernel yields a mean error approximately 22% higher than the other two kernels, though this discrepancy is not uniform, decreasing from +40% at $\gamma_{HG} = 0.05$ to +11% at $\gamma_{HG} = 2$ and +5% at $\gamma_{HG} = 5$.

The hourglass control term stiffens both the disk and the steel tip of the piston. Figure 6b shows that, at the same piston displacement, the load is higher than at $\gamma_{HG} = 0$ by 16.2–17.1% at $\gamma_{HG} = 2$ and by 25.4–26.4% at $\gamma_{HG} = 5$. The disk alone accounts for 53–83% of that rise, and the steel tip for the rest. To reach a given load F_N/b, the piston velocity v_p must be recalibrated with γ_{HG} as

$$v_p = \frac{u_p}{t_p}, \qquad u_p = \frac{u^*}{2}\left[1 - \left(1 - \frac{4\,F_N/b}{\kappa(\gamma_{HG})\,u^*}\right)^{1/2}\right], \qquad \kappa(\gamma_{HG}) = k_2\,\frac{1 + a_p\,\gamma_{HG}^{\epsilon_p}}{1 + a_p\,2^{\epsilon_p}}, \quad (34)$$

where $u^* = 4950 \pm 90$ µm and $k_2 = 0.3312 \pm 0.0001$ kN m^{-1} µm^{-1}, fitted on the staged simulation of Section 3.7.2 ($\Delta p = 0.15$ mm, $\gamma_{HG} = 2$), and $a_p = 0.116 \pm 0.004$ and $\epsilon_p = 0.510 \pm 0.011$, fitted on the Hourglass test with the three kernels.

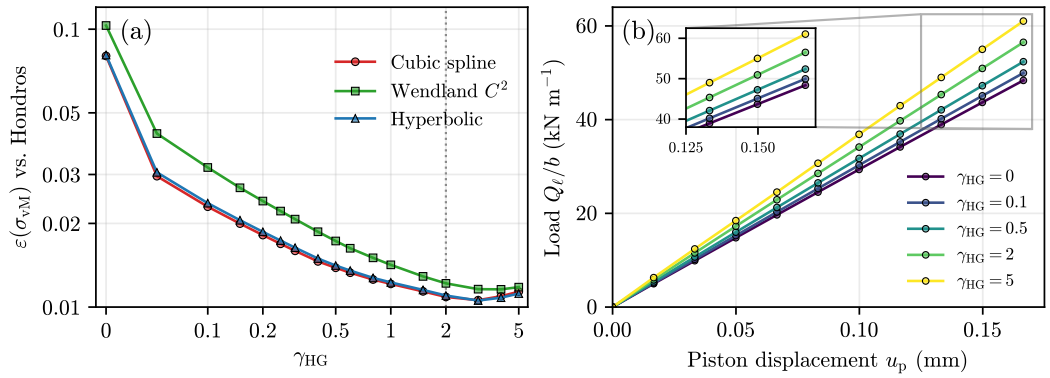


Figure 6. Hourglass test: 17 values of the hourglass control coefficient γ_{HG}, the same for the disk and the steel tip, with the other parameters at the baseline of the stability tests. (**a**) Error $\varepsilon(\sigma_{vM})$ averaged from t_r against γ_{HG} for the three kernels; vertical axis logarithmic, horizontal linear below 0.1, logarithmic above; dotted line: baseline, $\gamma_{HG} = 2$. (**b**) Load per unit thickness of the chord on the horizontal diameter, Q_ℓ/b, against the piston displacement u_p during the push, for the cubic spline kernel at $\gamma_{HG} = 0$, 0.1, 0.5, 2 and 5; inset: the end of the push.

This hardening adds no damping but raises the oscillation frequency and slows its decay. Figure 7a shows that the frequency, relative to its value at $\gamma_{HG} = 0$, increases with γ_{HG} by up to 12.9–13.3% at $\gamma_{HG} = 5$, almost identically for the three kernels. In Figure 7b, τ grows from 0.81–1.10 ms without control to 1.87–1.98 ms at $\gamma_{HG} = 2$ for the three kernels.

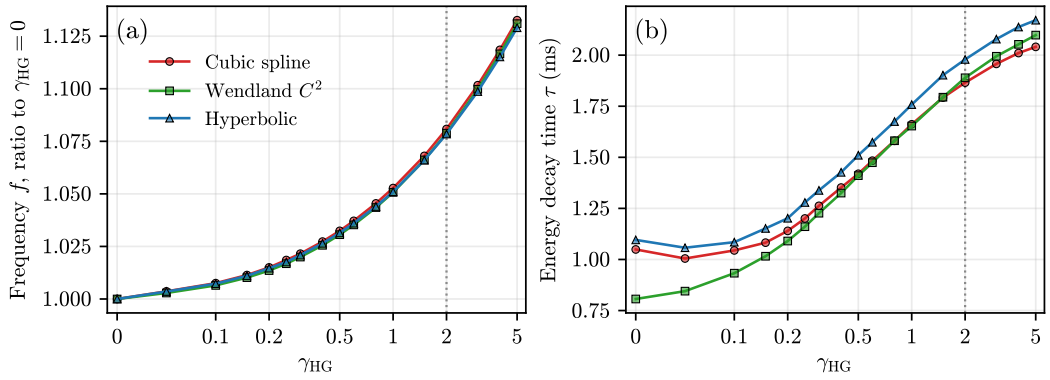


Figure 7. Hourglass test, continued, for the three kernels, with the horizontal axis and dotted line of Figure 6a. (**a**) Frequency f of the oscillation after the stop, divided by its value at $\gamma_{HG} = 0$. (**b**) Decay time τ of $\hat{K}$ after the stop.

The baseline keeps $\gamma_{HG} = 2$, the value of the Convergence map. At this value, the errors are 2.7, 5.1 and 4.2% above their minima, at $\gamma_{HG} = 3$, 4 and 3, for the cubic spline, Wendland C^2 and hyperbolic kernels, respectively. This choice was made because the maximum error reduction from $\gamma_{HG} = 2$ to 3 or 4 is ∼5%, but the standard GPU runs of Appendix E cost ∼10–16% more time at their own elbows of Equation (A8). These results were obtained at the baseline resolution only; the Convergence map keeps $\gamma_{HG} = 2$ at every β and Δp.

4.2. Convergence Map

4.2.1. The Rest Stage over the Convergence Map

Over the Convergence map, the decay time τ, the rest time t_r and the rest stage are obtained with the same methodology as in the stability tests (Section 3.3); what changes is what is varied, here β, Δp and the kernel. The decay time τ follows a power law of the smoothing length h with exponent -1.209 ± 0.004, as shown in Appendix E. This explains why the simulations at fine resolution need a longer time after the stop (Section 3.6). In the rest stage, the principal stress difference changes little. In the 441 simulations selected in Section 3.6, Ψ_σ (Equation (28)) is at most 3.6×10^{-3} from t_r on.

As shown in Figure 8, below the reading threshold $\hat{K} = 0.01$, the median of Ψ_σ is 2.6×10^{-4} and at most 7.3×10^{-4} in each decade of $\hat{K}$; it reaches only 1.8×10^{-3} at $\hat{K} = 0.10$–0.54. Evaluated against the last saved instant, Ψ_σ systematically shrinks toward the end of each simulation. Over the first 70% of the post-stop period, its median below the threshold is still a low 4.3×10^{-4}. Its maximum value, 1.1×10^{-2}, occurs prior to t_r, specifically 2 ms after the piston stops, where $\hat{K} = 0.058$.

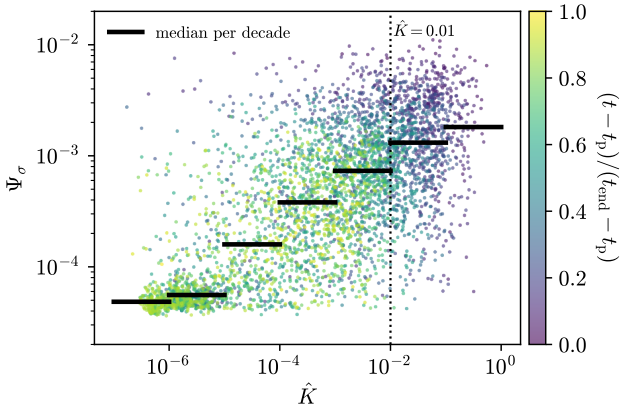


Figure 8. Relative L_1 distance Ψ_σ between the principal stress difference at each output t, 1 ms apart, and at the last one, t_{end}, against the dimensionless kinetic energy $\hat{K}$, on logarithmic axes. Dots: saved instants after the piston stop, $t > t_p$, in 441 simulations of the Convergence map, colored by the time from the stop, $(t - t_p)/(t_{end} - t_p)$; black segments: median of Ψ_σ in each decade of $\hat{K}$. Dotted line: reading threshold, $\hat{K} = 0.01$. Varied: β, Δp and the kernel. Other parameters at the baseline of the Convergence map.

4.2.2. Analytical Solution and Error

Numerical stresses are validated against the analytical solution of Hondros [35] for a disk of radius R_{ef}, which corresponds to the measured radius of the discrete disk (Equation (21)). The load is applied across two arcs whose half-width $R\psi$ matches that of the band of disk particles bonded to the steel tip and the support (Appendix B), with the normal load F_N measured in each simulation on the chords (Equation (20), Appendix C). Alternative conventions for the radius and a fixed-width loaded arc are evaluated in Appendix G.

The stress error $\varepsilon(\sigma_{vM})$ is defined by Equation (23) over every particle of the disk—referred to below as *all zones* to contrast with the localized regions in Section 4.2.5. It compares the SPH and analytical fields averaged particle by particle over the rest stage, as described in Section 3.3, with a median of 40 outputs per simulation. The L_1 norm of Equation (23) is used throughout this work. With an L_2 norm, the zones within 0.1 R_{ef} of the contact points would carry almost all of the error at $\Delta p = 0.15$ mm, artificially dropping the convergence order to 0.19–0.24.

The Convergence map spans three kernels, 74 values of β (from 0.54 to 2.00) and 29 particle spacings Δp (from 0.15 to 3 mm). This configuration yields a total number of

flexible particles N (including both the disk and the steel tip) ranging from 246 to 9.2×10^4. The total count N is derived from a power-law fit to the empirical particle counts, given by $N \propto \Delta p^{-1.98}$ (exponent -1.977 ± 0.002; cf. Equation (30)). All 6438 simulations performed successfully reached the rest stage and are included in the analysis. Notably, the spacing $\Delta p = 0.80$ mm yields an error below that of its immediate neighbors, sitting at a median of 5% below the geometric mean of the errors at $\Delta p = 0.75$ mm and 0.85 mm, for $\beta \geq 0.9$.

4.2.3. Error over the β–Δp Plane

Figure 9 shows $\varepsilon(\sigma_{\mathrm{vM}})$ over the β–Δp plane. Three regimes appear at every resolution. Below $\beta \approx 0.8$, where the support holds too few neighbors, the error is 0.32–0.34 for $\Delta p \geq 0.5$ mm and still 0.11–0.14 at $\Delta p = 0.15$ mm. It falls steeply to a valley at $\beta \approx 1.1$–1.3, and then rises slowly with β. The lowest error at each spacing decreases as Δp decreases, from 0.06–0.07 at $\Delta p = 3$ mm to 0.0026–0.0030 at 0.15 mm.

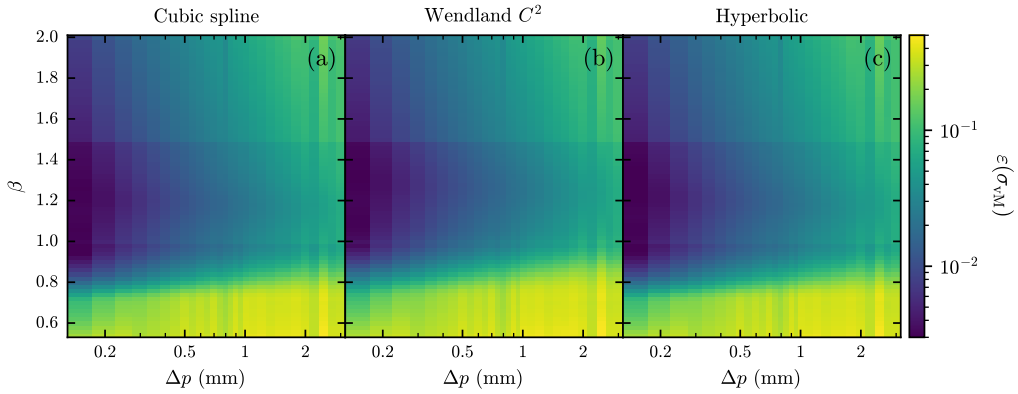


Figure 9. Convergence map: β and Δp varied, the other parameters at the baseline of the Convergence map. Relative von Mises error $\varepsilon(\sigma_{\mathrm{vM}})$ over the β–Δp plane, on a logarithmic horizontal axis and a logarithmic color scale, for the (**a**) cubic spline, (**b**) Wendland C^2 and (**c**) hyperbolic kernels.

When plotted against β at a fixed Δp (Figure 10), the error exhibits sharp jumps wherever the support radius $kh = 2\beta\,\Delta p$ reaches an axial layer of the initial lattice (i.e., particles located at an integer number of spacings along a lattice axis). It increases by 13%, 24% and 10% at $\beta = 1.00$, 1.50 and 2.00, respectively. In contrast, it varies by only 2% (median; 3% at the 90th percentile) between neighboring values of β elsewhere, including across the off-axis layers.

At a constant smoothing length h (evaluated at $h = 0.3$, 0.5, 1 and 2 mm), the influence of β depends heavily on the interval: for $\beta \in [1.00, 1.48]$, where the error minimum is located, the error varies by a factor of 1.6–2.3; for $\beta \in [1.50, 1.98]$, it changes by at most 11% and depends primarily on h.

The minimum at each spacing (stars in Figure 10) lies at a median β of 1.18 for the cubic spline and hyperbolic kernels and 1.26 for the Wendland C^2 kernel. For the cubic spline and hyperbolic kernels, the jump at $\beta = 1$ splits the error valley into two nearly equal local minima, which explains why the global minimum shifts to $\beta = 0.98$ at 4 of the 29 spacings. Over the other minima, weighted by $1/\varepsilon(\sigma_{\mathrm{vM}})$, the optimal β follows a power law of the spacing, $\beta_{\mathrm{opt}} \propto \Delta p^{\eta}$, with $\eta = -0.014 \pm 0.002$ for the cubic spline, -0.025 ± 0.003 for the Wendland C^2 and -0.019 ± 0.002 for the hyperbolic kernel. Over the swept spacings, the optimal β stays between 1.16 and 1.20–1.22 for the cubic spline and hyperbolic kernels and between 1.22 and 1.30 for the Wendland C^2 kernel. The number of neighbors that gives the lowest error therefore grows with the number of particles, but slowly: by Equations (30) and (31), $n_{\mathrm{nb}} \propto N^{0.014 \pm 0.002}$, $N^{0.025 \pm 0.003}$ and $N^{0.020 \pm 0.002}$, respectively. The Wendland C^2 kernel needs more neighbors to reach its region of lowest

error, $n_{\mathrm{nb}} \approx$ 19–22, against 17–19 for the other two kernels. This growth follows the trend $n_{\mathrm{nb}} \to \infty$ as $N \to \infty$ required for convergence, but it is far slower than the scaling $n_{\mathrm{nb}} \propto N^{0.5}$ estimated by Zhu et al. [22]. Two possible causes are the contacts, which set the error at fine spacings, and the corrected kernel gradient of Section 2.2, which removes the zeroth-order error that this scaling balances.

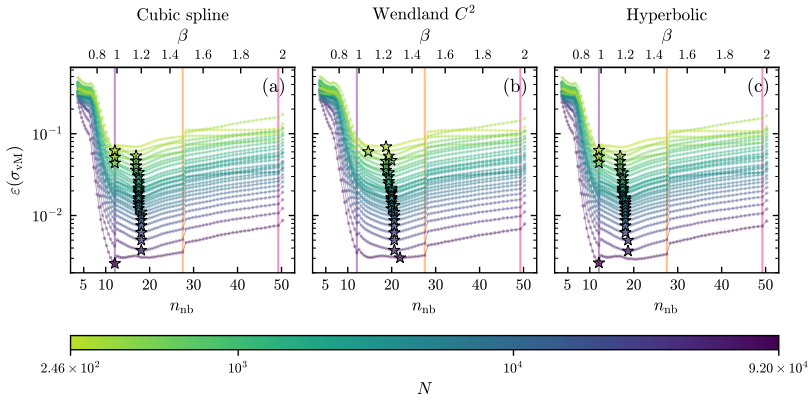


Figure 10. Error $\varepsilon(\sigma_{\mathrm{vM}})$ over all zones against the number of neighbors, $n_{\mathrm{nb}} = \pi(2\beta)^2$, Equation (31) without its integer part (bottom axis, linear), and the smoothing-length ratio, β (top axis); 29 curves, one per spacing, colored by the number of particles, N; stars: the minimum of each curve; vertical lines: $\beta = 0.98$ (purple), 1.48 (orange) and 1.98 (magenta), the branches of constant β studied below. Kernels: (**a**) cubic spline, (**b**) Wendland C^2, (**c**) hyperbolic.

In addition to the simultaneous limits recalled in Section Convergence, the consistency of standard SPH requires that $n_{\mathrm{nb}}/N \to 0$ (Sections 5 and 6.1 of Sigalotti et al. [30]); both conditions are formulated for uncorrected kernel sums. Since the optimal n_{nb} grows only slowly with N, the condition $n_{\mathrm{nb}}/N \to 0$ is met here. Using the relations from Equations (31) and (30), this ratio can be expressed as:

$$\frac{n_{\mathrm{nb}}}{N} \approx \frac{4\pi h^2}{A_{\mathrm{eff}}}, \tag{35}$$

up to the integer parts of Equations (31) and (30). Consequently, for a fixed domain, the condition $n_{\mathrm{nb}}/N \to 0$ is equivalent to $h \to 0$, meaning that the error plotted against n_{nb}/N reflects the error as a function of h^2 (Figure 11).

A single power-law fit to all simulations with $\beta \geq 1$ yields $\varepsilon(\sigma_{\mathrm{vM}}) \propto (n_{\mathrm{nb}}/N)^{0.520\text{–}0.528}$ (± 0.003), which corresponds to $\varepsilon(\sigma_{\mathrm{vM}}) \propto h^{1.04\text{–}1.06}$ (± 0.006; with a root-mean-square residual of $\ln \varepsilon(\sigma_{\mathrm{vM}})$ between 0.17 and 0.18). Below $\beta \approx 0.8$, the error is dominated by the deficiency of neighboring particles. Since the current parameter sweep reaches at most $n_{\mathrm{nb}} \approx 50$, it does not explicitly test the asymptotic limit $n_{\mathrm{nb}} \to \infty$.

The best results of the three kernels are similar: the hyperbolic kernel has its minimum on the branch $\beta = 0.98$, with $\varepsilon(\sigma_{\mathrm{vM}}) = 0.00264$, and the Wendland C^2 kernel at $\beta = 1.32$, with $\varepsilon(\sigma_{\mathrm{vM}}) = 0.00304$. All kernels therefore perform well at their best β; the cubic spline has the lowest error, $\varepsilon(\sigma_{\mathrm{vM}}) = 0.00259$, at $\beta = 0.98$, but the difference is small.

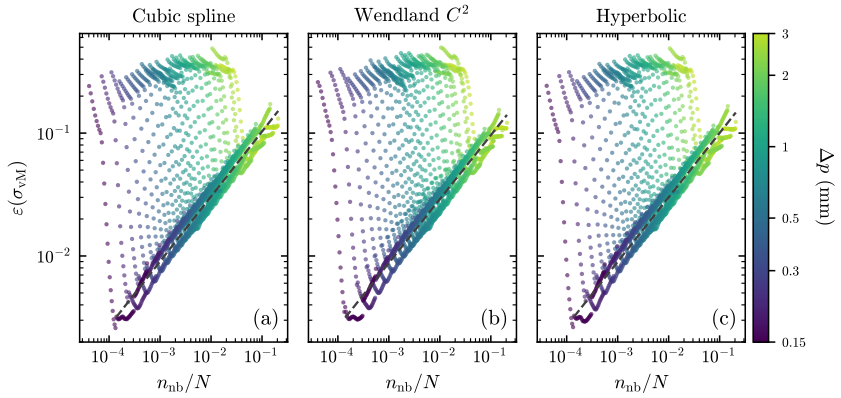


Figure 11. Error $\varepsilon(\sigma_{\mathrm{vM}})$ over all zones against the ratio of the number of neighbors to the number of particles, n_{nb}/N, on logarithmic axes; one semi-transparent point per simulation, colored by its spacing Δp; here $n_{\mathrm{nb}} = \pi(2\beta)^2$, Equation (31) without its integer part, and N from the fitted particle count. Gray dashed line: power-law fit over $\beta \geq 1$. Kernels: (**a**) cubic spline, (**b**) Wendland C^2, (**c**) hyperbolic.

4.2.4. Convergence at Constant β

The order of convergence ζ is the exponent of the error in h, $\varepsilon \propto h^{\zeta}$; for the kernel interpolation of a smooth field away from boundaries $\zeta = 2$ (Section Convergence). It is measured along branches of constant β, on which the number of neighbors is fixed and $h = \beta\,\Delta p$ (Equation (19)) shrinks with the resolution. Three branches are taken just below the three axial jumps of Figure 10: $\beta = 0.98$, 1.48 and 1.98, with nominal $n_{\mathrm{nb}} = 12$, 27 and 49 (8, 24 and 44 particles inside the support on the initial lattice), a low, an intermediate and a high number of neighbors.

Along each branch (Figure 12), the error over all zones is fitted by least squares on $\ln \varepsilon(\sigma_{\mathrm{vM}})$, with $\varepsilon(\sigma_{\mathrm{vM}}) = \mathcal{A}\,N^{-\zeta/1.98} + \varepsilon_\infty$, $\varepsilon_\infty \geq 0$, where $\mathcal{A}$ is an amplitude; since $N \propto \Delta p^{-1.98}$ and $h \propto \Delta p$, this is $\varepsilon(\sigma_{\mathrm{vM}}) \propto h^{\zeta}$ plus a constant. Table 3 lists the fits. The standard errors are multiplied by $\sqrt{(1+r_1)/(1-r_1)}$, where r_1 is the lag-one autocorrelation of the residuals between neighboring spacings (no correction when $r_1 < 0$); the interval of ε_∞ is a profile-likelihood interval with the same correction.

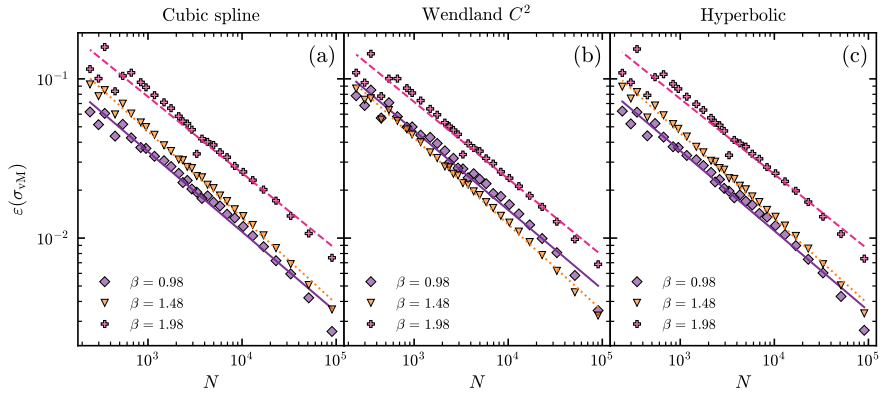


Figure 12. Error $\varepsilon(\sigma_{\mathrm{vM}})$ over all zones against the number of particles, N, on logarithmic axes, along the branches $\beta = 0.98$ (purple diamonds), 1.48 (orange triangles) and 1.98 (magenta pluses), with the power-law fits (solid, dotted and dashed lines), where the slope is $-\zeta/1.98$. Kernels: (**a**) cubic spline, (**b**) Wendland C^2, (**c**) hyperbolic.

Table 3. Fit of the error over all zones along the three branches of constant β, $\varepsilon(\sigma_{\mathrm{vM}}) = \mathcal{A}\, N^{-\zeta/1.98} + \varepsilon_\infty$, over the 29 spacings: order ζ with its standard error; and the constant term ε_∞: its best fit, its one-standard-deviation profile-likelihood interval, and its 95% upper bound, where the scaled profile sum of squared residuals rises by 3.84.

Kernel	β	ζ	ε_∞ (10^{-4})		
			Best Fit	**Interval**	**Upper Bound**
Cubic spline	0.98	1.00 ± 0.04	0.0	[0.0, 2.3]	8.2
	1.48	1.07 ± 0.02	0.0	[0.0, 1.1]	3.9
	1.98	0.95 ± 0.04	0.0	[0.0, 6.8]	22.9
Wendland C^2	0.98	0.98 ± 0.04	0.0	[0.0, 3.0]	10.9
	1.48	1.07 ± 0.02	0.0	[0.0, 0.8]	3.3
	1.98	0.95 ± 0.03	0.0	[0.0, 5.1]	17.8
Hyperbolic kernel	0.98	0.99 ± 0.04	0.0	[0.0, 2.2]	7.8
	1.48	1.06 ± 0.02	0.0	[0.0, 1.2]	4.2
	1.98	0.94 ± 0.04	0.0	[0.0, 7.1]	23.8

The best constant term is zero on all nine branches, and $\zeta = 0.94$–1.07: over all zones the error converges at first order in h. The same holds for every constant value of $\beta \geq 1$ of each kernel, 51 per kernel, with $\zeta = 0.93$–1.08 and a median standard error of 0.020–0.022. Along the optimal β of each spacing, given by the power law $\beta_{\mathrm{opt}} \propto \Delta p^{\eta}$ of Section 4.2.3 rounded to the nearest β of the map, the error also converges at first order, with $\zeta = 1.04 \pm 0.01$ for the cubic spline and Wendland C^2 kernels and 1.04 ± 0.02 for the hyperbolic kernel. A zero constant term is what Section Convergence anticipates. Uncorrected kernel sums reach a floor at a constant neighbor count [22,30], whereas the corrected gradient of Section 2.2, exact for linear fields, removes the zeroth-order term that sets it (Section 7 of Zhu et al. [22]).

To quantify this, the 95% upper bound of the asymptotic error ε_∞ was evaluated relative to the error at the finest particle spacing across the 51 values of β of each kernel. This relative upper bound exhibits a median of 0.12–0.13 and a 90th percentile of 0.22–0.28. Consequently, within the resolution range examined and assuming a constant convergence order, any potential error floor remains below 28% of the finest-resolution error for 90% of these values of β. Notably, this upper bound reflects the resolution limits of the investigated parameter sweep, rather than definitive proof that an error floor does not exist at even smaller values of Δp.

4.2.5. Excluding a Neighborhood of the Contacts

To locate the sources of error, the disk is split into three regions by the distance s to the nearer contact point, $(0, \pm R_{\mathrm{ef}})$, and by the distance $R_{\mathrm{ef}} - r$ from the boundary, both compared with a threshold $s_{\min}$ set as a fixed fraction of the radius (Figure 13):

- the *contact zones*, $s < s_{\min}$;
- the *rim*, $R_{\mathrm{ef}} - r < s_{\min}$ outside the contact zones;
- the *interior*, the rest.

Since $s_{\min}$ scales with the radius, each region covers the same portion of the disk at all resolutions. The error of a region, Equation (23) restricted to its particles, is denoted ε_{c}, $\varepsilon_{\mathrm{rim}}$ and $\varepsilon_{\mathrm{int}}$ for the contact zones, the rim and the interior, respectively; $\varepsilon(\sigma_{\mathrm{vM}})$ is kept for the error over all zones.

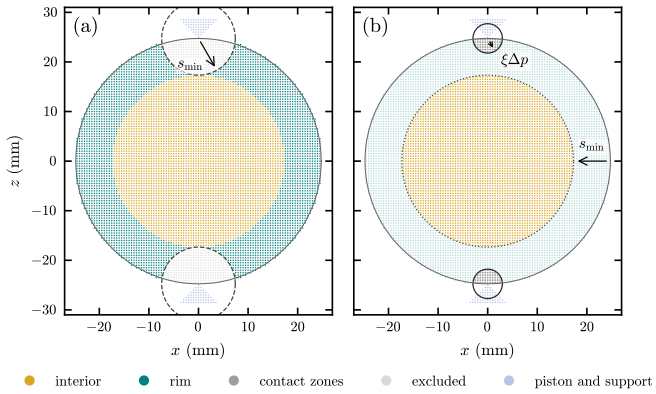


Figure 13. Regions and exclusions on the reference lattice of a disk with $\Delta p = 0.5$ mm, piston on top, at $s_{\min}/R_{\text{ef}} = 0.3$: interior (gold), rim $R_{\text{ef}} - r < s_{\min}$ (teal) and contact zones (silver); each excluded region is drawn in its own color, translucent. (**a**) The contact zones $s < s_{\min}$ excluded (dashed circles). (**b**) The circular band $R_{\text{ef}} - r < s_{\min}$ excluded except the loaded arcs, $s < \xi\Delta p$ (solid circles), drawn enlarged in the color of the contact zones.

To evaluate the spatial distribution of these errors, we define two metrics:

- The *contribution* of a region is the sum of its absolute errors divided by the global denominator of Equation (23), meaning that the individual contributions of the three regions sum up exactly to $\varepsilon(\sigma_{\text{vM}})$.
- The *share* of a region is its relative contribution, calculated as its absolute contribution divided by $\varepsilon(\sigma_{\text{vM}})$.

If the contact zones degrade the convergence order, the remaining portions of the disk should converge faster once a neighborhood surrounding the contact points is excluded. To test this hypothesis, $s_{\min}$ is widened progressively from 0 to 0.95 R_{ef}, and three distinct exclusions are compared along the three branches (Figure 14):

1. Excluding the contact zones, which leaves the interior and the rim.
2. Excluding both the contact zones and the rim, which isolates the interior.
3. As a control, excluding the circular band $R_{\text{ef}} - r < s_{\min}$ except for the loaded arcs ($s < \xi\Delta p$), thereby retaining the 1–8 particles per contact point inside the equivalent loaded arc of the analytical solution.

The convergence order along each branch is the slope of $\ln \varepsilon$ against $\ln h$ across its 29 particle spacings for each kernel, averaged over the three kernels; its standard deviation comes from a bootstrap over Δp.

The same exclusions are then applied to the SPH operator alone, evaluated on the exact displacement field of the analytical solution, with no dynamics, no contact model and no rest stage. Its error is the interpolation error alone and gives the accuracy that the method would reach if the discrete displacement were exact. The operator is the corrected kernel gradient of the structural solver (Section 2.2) using the correction matrix of Liu and Liu [45], which is equivalent to the gradient formulation of the corrective smoothed particle method (CSPM), Equation (15) of Chen et al. [58]. This operator is applied exclusively to the initial lattice of the disk, omitting the particles of the steel tip and support. It takes the exact displacement from the analytical solution defined on the same R_{ef} and loaded arcs; the corresponding von Mises stress is then computed via the plane-stress Hooke's law, and its error is evaluated using Equation (23).

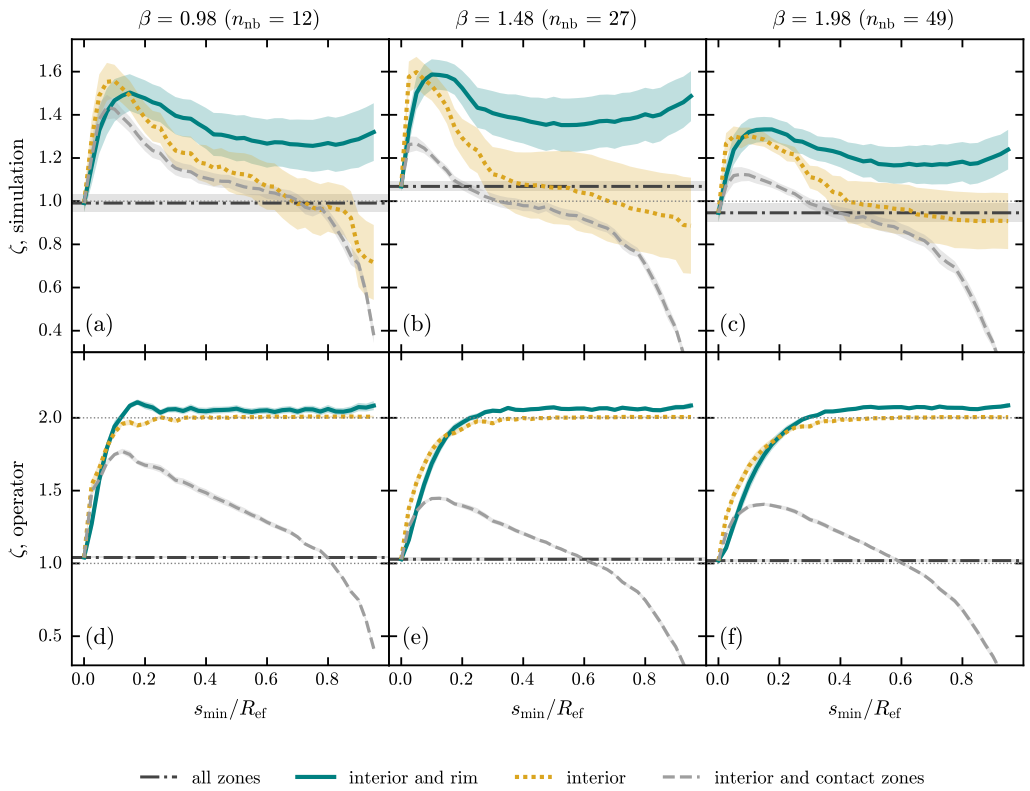


Figure 14. Order of the error, ζ, along the branches $\beta = 0.98$, 1.48 and 1.98 (columns; 29 spacings from 0.15 to 3 mm), against the width of the excluded zone over the radius, s_{min}/R_{ef}; mean of the three kernels, with one standard deviation from a bootstrap over Δp (bands). Top row, (**a**–**c**): simulation; bottom row, (**d**–**f**): the SPH operator on the exact field. Dark gray, dash-dotted: all zones; teal, solid: interior and rim, the contact zones excluded; gold, dotted: interior, the contact zones and the rim excluded; silver, dashed: interior and contact zones, the circular band excluded except $s < \xi \Delta p$. Each curve has the color of the outermost zone it keeps.

Over all zones, the convergence order of the three branches ranges from 0.95 to 1.07 in the simulation, compared to 1.02–1.04 for the operator alone. The slope computed without a constant term agrees, within its statistical error, with the value of ζ reported in Table 3.

For the operator alone, excluding the contact zones raises the convergence order to 2 once s_{min} reaches approximately 0.10, 0.17 and 0.25 R_{ef} on the respective branches. Beyond these thresholds, the quadratic convergence is maintained, demonstrating that away from the contact points, the interpolation error is strictly of second order (including at the free boundary). Under these conditions, isolating the interior region yields identical scaling behavior. In the control, the few particles kept at the contact points are enough to hold the order of the operator at or below 1.75, 1.45 and 1.39 on the three branches.

In contrast, the full simulation does not reach this theoretical bound. Excluding the contact zones increases the convergence order to 1.32–1.59 at $s_{min} \approx 0.1$–$0.175\, R_{ef}$, after which it plateaus between 1.2 and 1.4. When the rim is also excluded, the convergence order of the interior reaches a peak of 1.30–1.60 at $s_{min} = 0.050$–$0.100\, R_{ef}$ before decreasing to 0.9–1.2 beyond $0.3\, R_{ef}$. Meanwhile, the control configuration yields values of 1.12–1.38 at $0.05\, R_{ef}$ and 0.9–1.1 at $0.5\, R_{ef}$. The bands of Figure 14 give the standard deviation of the orders: $\pm$0.02–0.13 in the simulation and $\pm$0.01–0.06 for the operator.

Consequently, away from the contact regions, the full simulation exhibits first-order convergence. The higher orders found when only the contact zones are excluded come from the rim, which converges faster than the interior at these wide exclusion radii (the

teal curve lies above the gold one in Figure 14a–c), and from a quadratic component near the contacts, quantified below.

This first order does not come from the loss of consistency of the corrected gradient at a boundary. For the corrected gradient, the truncation error is of second order where the neighborhood is symmetric and of first order within one support radius, kh, of a boundary (pp. 235 and 240 of Chen et al. [58]). Such a band contributes to the L_1 norm (Equation (23)) at order h^2, and at order $h^{3/2}$ to a root-mean-square norm, consistent with the rates measured for corrected gradients without boundary treatment by Sigalotti et al. [23]. The operator reaches order 2 even with the free boundary kept (teal curves in Figure 14d–f). A concentrated load limits the order of finite elements in the same way [59], and the optimal order is recovered on subdomains that exclude it [60].

A scaling analysis, which extends the argument presented in Section Convergence, explains why the contact regions restrict the interpolation error to first order over all zones. Near a contact point, the analytical solution closely approximates the field of a point load, $|\sigma| \sim F_\mathrm{N}/(\pi b\, s)$, whose second-order derivatives grow as s^{-3}. Under a second-order interpolation scheme, the pointwise error scales as $h^2|\sigma|/s^2$. Integrating this error outside a characteristic distance $s_* \gg h$ from the contact points yields $\int_{s_*} h^2 s^{-3}\, s\, ds \sim h^2/s_*$, while the denominator of Equation (23) remains finite. A fixed cutoff distance, $s_* = s_\mathrm{min}$, therefore results in an error scaling of $\varepsilon(\sigma_\mathrm{vM}) \sim h^2$, consistent with the second-order convergence achieved by the operator in Figure 14d–f.

Conversely, when evaluated over all zones, the fields are effectively bounded only by the half-width of the loaded arc, $s_* \sim R\psi \propto h$ (Appendix B). Within this loaded arc, the relative error is of order unity over an area scaling as $(R\psi)^2$, where the stress magnitude is $|\sigma| \sim F_\mathrm{N}/(bR\psi)$. Both the integration outside the arc and the core contribution within it lead to $\varepsilon(\sigma_\mathrm{vM}) \sim h$, explaining the first-order convergence measured for the operator across all zones. Note that this derivation constitutes a purely theoretical scaling estimate of the interpolation error rather than an empirical fit.

The interpolation error is therefore not what limits the simulation away from the contacts. The operator alone isolates the interpolation, whereas the simulation also carries the error of its discrete solution, which is set by the whole disk. Two mechanisms are consistent with its first-order component in the interior. The large errors generated at the contacts spread through the disk by global equilibrium (pollution), and the circular boundary and the two wedges are mapped onto a rectangular lattice, so the radius and the load points are known only to within Δp (Appendix G.2). A shift of a load point by a fraction of Δp changes the stress at a distance s by a relative amount of order $\Delta p/s$, which is of first order in h at any fixed distance. Both act at a distance, so excluding a neighborhood of the contacts does not remove them, and the present data do not separate them.

4.2.6. Linear and Quadratic Parts of the Error

Along each branch, both the error over all zones, $\varepsilon(\sigma_\mathrm{vM})$, and the localized error within the interior, ε_int, are fitted using the polynomial form $\varepsilon = C_1 h + C_2 h^2$. This fit is performed via relative least squares across the 29 particle spacings, with standard errors corrected following the procedure outlined in Section 4.2.4. Within the interior region, the quadratic coefficient C_2 reaches its maximum magnitude at $s_\mathrm{min}/R_\mathrm{ef} = 0.050$, 0.025 and 0.025 for the respective branches; for $\beta = 1.48$ and 1.98 the interior order levels off in this interval, whereas for $\beta = 0.98$ it keeps rising up to 0.1 (Figure 15).

Table 4 lists both coefficients and the ratio of the quadratic term to the linear one, $|C_2|h/C_1$.

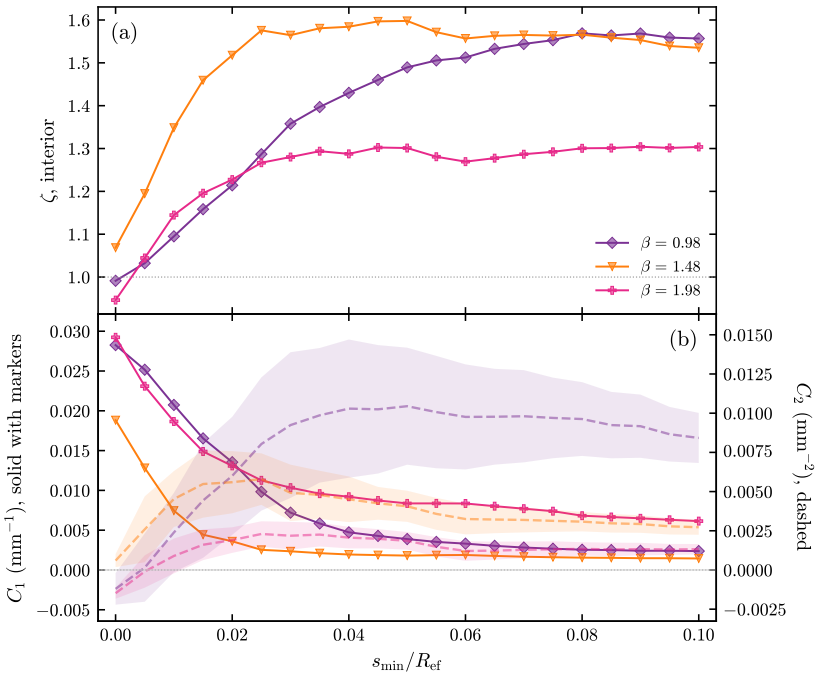


Figure 15. Convergence of the interior error (the contact zones and the rim excluded) against the width of the excluded zone, $s_{\min}/R_{\mathrm{ef}}$, from 0 to 0.1 in steps of 0.005, along the branches $\beta = 0.98$, 1.48 and 1.98, with the colors and markers of Figure 12; simulation, mean of the three kernels, 29 spacings. (**a**) Order of the error, ζ. (**b**) Coefficients of $\varepsilon_{\mathrm{int}} = C_1 h + C_2 h^2$: C_1 (left axis, solid lines with markers) and C_2 (right axis, dashed, with one standard error shaded).

Table 4. Linear and quadratic coefficients of $\varepsilon = C_1 h + C_2 h^2$ (h in mm) in the simulation along the three branches, over all zones ($\varepsilon = \varepsilon(\sigma_{\mathrm{vM}})$) and in the interior at the exclusion radius where C_2 is largest ($\varepsilon = \varepsilon_{\mathrm{int}}$); mean of the three kernels, with one standard error corrected as in Section 4.2.4. Last columns: quadratic-to-linear ratio, $|C_2|h/C_1$, at the finest spacing, $h = 0.15\beta$ mm, and at $h = 1$ mm.

β	Region	C_1 (10^{-3} mm^{-1})	C_2 (10^{-3} mm^{-2})	$\lvert C_2\rvert h/C_1$ (%)	
				Finest	$h = 1$ **mm**
0.98	All zones	28.3 ± 1.4	-1.21 ± 1.01	0.63	4.3
	Interior, $s_{\min} = 0.050\,R_{\mathrm{ef}}$	3.9 ± 2.5	10.40 ± 3.73	40	270
1.48	All zones	18.8 ± 0.8	0.60 ± 0.42	0.71	3.2
	Interior, $s_{\min} = 0.025\,R_{\mathrm{ef}}$	2.5 ± 1.6	5.80 ± 1.64	51	230
1.98	All zones	29.2 ± 1.1	-1.48 ± 0.35	1.5	5.1
	Interior, $s_{\min} = 0.025\,R_{\mathrm{ef}}$	11.3 ± 1.7	2.30 ± 0.81	6.0	20

At the exclusion radius where C_2 is largest, C_2 is 2.7–3.7 times its standard error for the individual kernels, and the quadratic term is 6–51% of the linear one at the finest spacing. Over all zones it is at most 1.5% there and 5% at $h = 1$ mm, so the error is linear in h to within a few percent. Restricted to $\Delta p \leq 0.5$ mm, the fit of Table 3 gives $\zeta = 1.10$–1.34 (± 0.03–0.06) over all zones; with a quadratic part of at most a few percent, the error stays linear in h.

4.2.7. Effect of the Contact Zones

On each branch, the disk is partitioned once at the exclusion radius where the interior quadratic coefficient is largest (Section 4.2.6): $s_{\min} = 0.050\,R_{\mathrm{ef}} \approx 1.25$ mm for $\beta = 0.98$, and $s_{\min} = 0.025\,R_{\mathrm{ef}} \approx 0.62$ mm for both $\beta = 1.48$ and $\beta = 1.98$. The resulting three regions correspond to those defined in Section 4.2.5.

The number of particles in each contact zone varies with the branch and the spacing: at $\Delta p = 0.15$ mm it is approximately 110, 28 and 28 for $\beta = 0.98$, 1.48 and 1.98, respectively, falling to 3, 1 and 1 at $\Delta p = 1$ mm. Because the contact point lies half a spacing outside the outermost particle centers (Equation (21)), the nearest particle is situated roughly $\Delta p/2$ away from it. A contact zone therefore holds particles only when $\Delta p < 2s_{\min}$, that is, below about 2.5, 1.2 and 1.2 mm for the respective branches. At coarser spacings, the particle nearest each contact point would count as interior, so the three regions are compared only at $\Delta p < 2s_{\min}$. Figure 16 illustrates the error within each region (ε_c, ε_{rim}, and ε_{int}) along the three branches, while Table 5 lists their respective convergence orders and error shares.

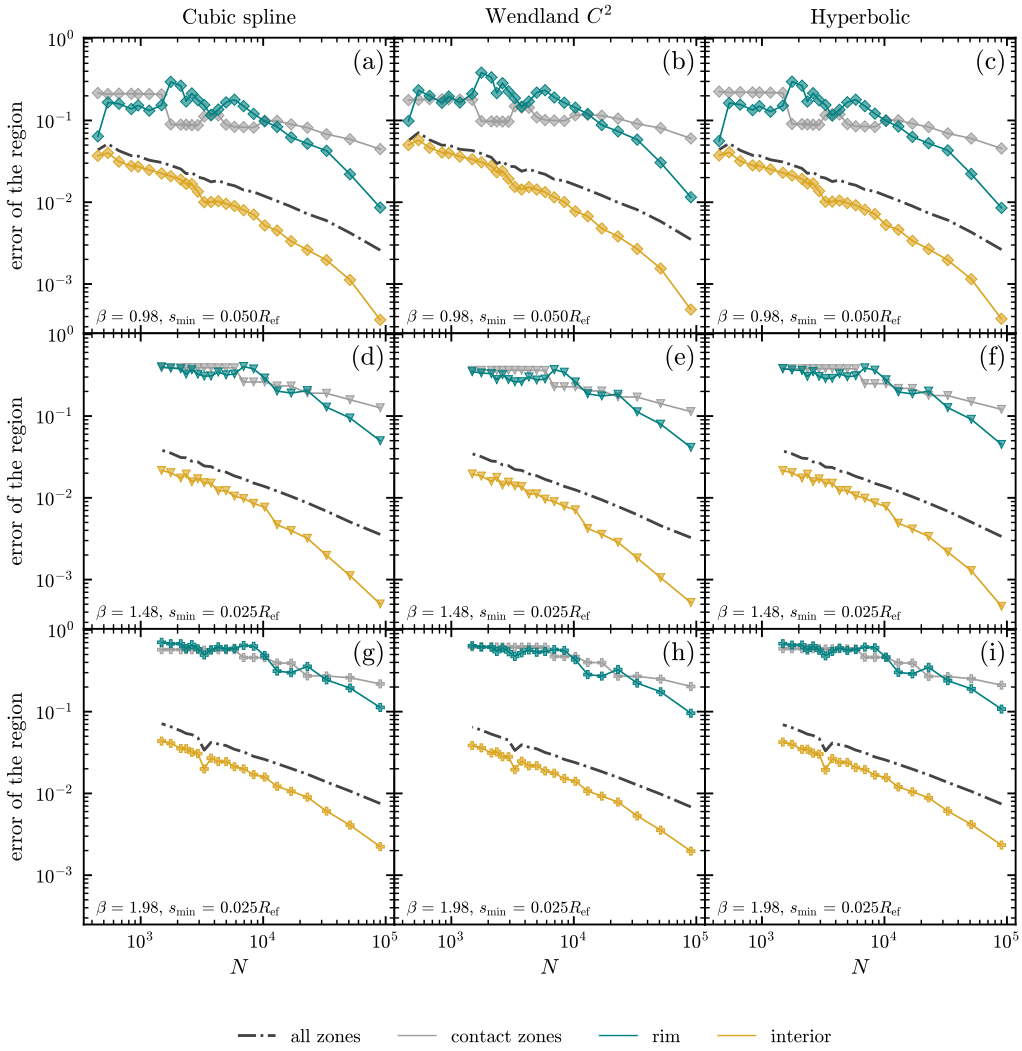


Figure 16. Error of each region with its own denominator, Equation (23) restricted to its particles, against the number of particles, N, on logarithmic axes, where the slope is $-\zeta/1.98$: contact zones (silver, ε_c), rim (teal, ε_{rim}) and interior (gold, ε_{int}), colored as in Figure 13; each branch has a different marker: $\beta = 0.98$ (diamonds), 1.48 (triangles) and 1.98 (pluses); and all zones (dark gray, dash-dotted, $\varepsilon(\sigma_{\text{vM}})$). Rows, (**a**–**c**), (**d**–**f**) and (**g**–**i**): the branches $\beta = 0.98$, 1.48 and 1.98, each cut at its own $s_{\min}$ and drawn at $\Delta p < 2s_{\min}$; columns: the cubic spline, Wendland C^2 and hyperbolic kernels.

The relative errors in the contact zones and the rim are significantly higher than those in the interior. Specifically, the median errors are 0.09–0.11, 0.36–0.39 and 0.57–0.61 in the contact zones of the three branches, 0.14–0.58 in the rim and 0.010–0.021 in the interior.

Table 5. Order ζ of the error of each region with its own denominator, with one standard error corrected as in Section 4.2.4, and median share of each region in the error over all zones, along the three branches, each cut at its own $s_{\min}$. The three regions are fitted over the same spacings, those at which the contact zones hold particles, $\Delta p < 2s_{\min}$. The shares are medians over the spacings, so they need not add up to 1; at the finest spacing, the contact zones carry 51–78% of the error (Figure 17).

		Order, ζ			Median Share		
Kernel	β ($s_{\min}/R_{\text{ef}}$)	ε_{c}	ε_{rim}	ε_{int}	**Contact Zones**	**Rim**	**Interior**
Cubic spline	0.98 (0.050)	0.55 ± 0.15	0.79 ± 0.38	1.57 ± 0.15	0.20	0.20	0.53
	1.48 (0.025)	0.59 ± 0.07	0.84 ± 0.24	1.74 ± 0.21	0.11	0.31	0.55
	1.98 (0.025)	0.52 ± 0.08	0.78 ± 0.16	1.33 ± 0.09	0.08	0.32	0.59
Wendland C^2	0.98 (0.050)	0.34 ± 0.11	0.77 ± 0.36	1.58 ± 0.16	0.18	0.19	0.57
	1.48 (0.025)	0.62 ± 0.08	0.83 ± 0.27	1.70 ± 0.20	0.12	0.29	0.55
	1.98 (0.025)	0.60 ± 0.09	0.80 ± 0.15	1.35 ± 0.09	0.09	0.32	0.57
Hyperbolic kernel	0.98 (0.050)	0.55 ± 0.15	0.77 ± 0.38	1.56 ± 0.14	0.20	0.19	0.53
	1.48 (0.025)	0.61 ± 0.08	0.83 ± 0.24	1.71 ± 0.19	0.11	0.29	0.56
	1.98 (0.025)	0.56 ± 0.09	0.77 ± 0.15	1.31 ± 0.08	0.08	0.31	0.59

All three regions exhibit convergence:

- The contact zones converge with $\zeta \approx 0.3$–0.6.
- The rim converges with $\zeta \approx 0.8$ for $\Delta p < 2s_{\min}$, increasing to 2.1 for $\beta = 0.98$, 1.5–1.6 for $\beta = 1.48$ and 1.2 for $\beta = 1.98$ when $\Delta p \leq 0.5$ mm.
- The interior converges with $\zeta \approx 1.3$–1.7, reflecting the mixture of linear and quadratic components discussed in Section 4.2.6.

The contribution of the contact zones to $\varepsilon(\sigma_{\text{vM}})$ decreases more slowly than their own error ($\zeta = 0.0$ to 0.2, ± 0.1, for $\Delta p < 2s_{\min}$, and 0.1–0.4, ± 0.06–0.17, for $\Delta p \leq 0.5$ mm). This occurs because the analytical stress within these zones increases as the spacing decreases. As the spacing decreases, the analytical field, that of a load distributed over a width proportional to h (Appendix B), never becomes singular but approaches that of a point load. Consequently, a zone of fixed size converges because it contains an increasing number of particles situated away from the contact point. Conversely, a zone that shrinks with the resolution does not converge. Within the loaded arc itself ($s < \xi \Delta p$), its own error barely changes with spacing, remaining at 0.16–0.32 for $\Delta p = 0.15$ and 1 mm ($|\zeta| = 0.00$–0.11, ± 0.01), and at 0.08–0.23 ($|\zeta| = 0.03$–0.12, ± 0.02) within $s < kh$.

The convergence order of this contribution depends directly on the partition boundary, varying from 0.12 ± 0.07 to 0.77 ± 0.04 as $s_{\min}/R_{\text{ef}}$ ranges from 0.025 to 0.2 (cubic spline, $\beta = 1.48$); thus, it does not reflect an intrinsic contact order. In contrast, the contributions of the rim and the interior decrease significantly faster ($\zeta \approx 1.3$–2.4, ± 0.07–0.39, for $\Delta p \leq 0.5$ mm).

The contact zones therefore take a growing share of the error as the resolution increases (Figure 17): from 7–12% at $\Delta p = 1$ mm to 51–78% at 0.15 mm over the three branches. At 0.15 mm the rim carries 9–19% and the interior 13–30%. The shares depend on the cut: with $s_{\min}/R_{\text{ef}}$ from 0.025 to 0.2, the median share of the contact zones over the spacings goes from 11 to 64% (cubic spline, $\beta = 1.48$).

Both the radius and the loaded arcs of the analytical solution depend on the discretization, and the error is sensitive to them (Appendix G). Shifting the radius of Equation (21) by $\Delta p/2$ raises the error at the finest spacing by a factor of 1.4–5.6, depending on the branch, and no choice of radius raises the order over all zones appreciably above 1. With loaded arcs of fixed half-width, the orders change little, but the error over all zones is 2.0–2.7 times larger. Fixing the offset at $\Delta p/2$ is consistent with these results (Appendix G.2).

Across the Convergence map, the error over all zones converges at first order in h, and the contact zones carry 51–78% of it at the finest spacing. Once a fixed neighborhood of the

contacts is excluded, the operator alone converges at second order, whereas the simulation stays at first order (Section 4.2.5).

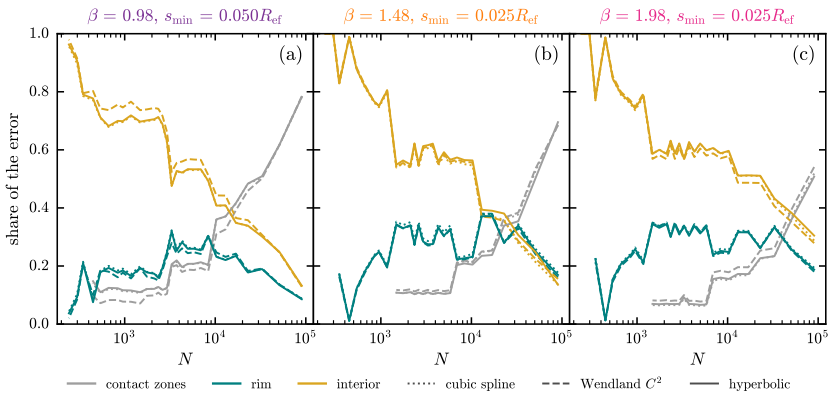


Figure 17. Share of the error over all zones carried by the contact zones (silver), the rim (teal) and the interior (gold), against the number of particles, N, on a logarithmic axis, for the cubic spline (dotted), Wendland C^2 (dashed) and hyperbolic (solid) kernels, along the branches (**a**) $\beta = 0.98$, (**b**) 1.48 and (**c**) 1.98, each cut at its own $s_{\min}$. Where the contact zones hold no particle, their share is not drawn.

4.3. Validation

The first plateau of the staged simulation, selected for the theoretical validation in Section 3.7 and averaged over its outputs 0.05 ms apart in its last 3 ms, yields an error of $\varepsilon(\sigma_{\mathrm{vM}}) = 0.0028$ against the Hondros solution. This comparison is evaluated at a measured load of $F_{\mathrm{N}}/b = 53.7$ kN m^{-1} using the loaded arcs defined by Equation (A6) with $R\psi = 0.201$ mm. The simulation is conducted with a hyperbolic kernel, $\Delta p = 0.15$ mm and $\beta = 1.28$. Over the Convergence map at $\Delta p = 0.15$ mm, $\beta = 0.98$ gives the lowest error, $\varepsilon(\sigma_{\mathrm{vM}}) = 2.6 \times 10^{-3}$ with the cubic spline, against 2.9×10^{-3} with the hyperbolic kernel at $\beta = 1.28$. At $\beta = 0.98$, however, the element of the disk at the pole of the support inverts, $J^i \leq 0$, once the piston has moved about 0.45 mm, before the 1300 N of Wan et al. [37] are reached. With more neighbors, the hyperbolic kernel at $\beta = 1.28$ avoids this inversion, so the validations use it, at the price of a slightly larger error. The experimental validation uses the four plateaus of the same simulation.

4.3.1. Theoretical Validation

Figure 18 illustrates the characteristic patterns of the numerical von Mises stress and its corresponding local error relative to the analytical solution of [35]. The local error is defined as $|\Phi_{\mathrm{t}}^i - \Phi_{\mathrm{n}}^i|$ normalized by the mean of $|\Phi_{\mathrm{t}}|$ over the entire disk, such that its spatial average corresponds to ε in Equation (23). As shown in Figure 18b, the local error has a median of 2×10^{-4} and exceeds 0.1 only within 2.6 mm of the contact points. This localized amplification occurs in only 0.2% of the particles, where the error reaches values of order 10.

As shown in Figure 19a,b, the simulated von Mises stress matches the analytical solution along both diameters. Near the contacts, Figure 19c shows that along the loading axis the two solutions agree within 5% from 0.53 mm, about three and a half particle spacings, from the contact point. Within the contact zone, the Hondros solution is bounded by the pressure of the loaded arc ($\chi = 133$ MPa). At the particle nearest to the contact point (0.075 mm away), where the analytical solution yields 114 MPa, the simulation predicts 95 MPa at the piston and 167 MPa at the support. This asymmetry arises because the two contacts differ. In FlexStruc, each flexible body is attached to a single clamp, so the disk is bonded to a rigid support (whose particles remain fixed) and coupled to the steel tip of

the piston (which deforms elastically). As a result, the actual boundary conditions in the numerical model differ from the frictionless, uniform pressure profile assumed by Hondros.

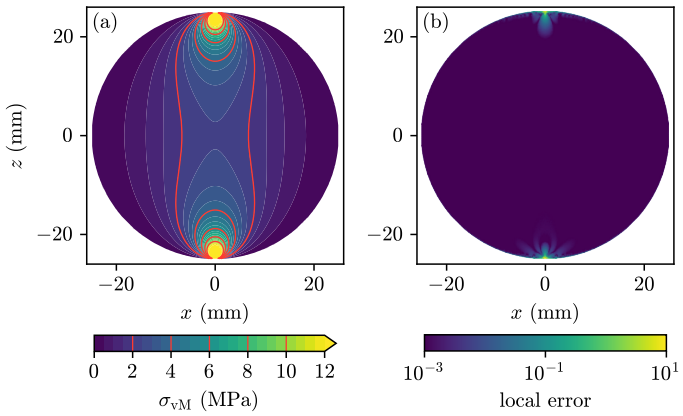


Figure 18. Theoretical validation at the first plateau (400 N) of the staged simulation ($\Delta p = 0.15$ mm, hyperbolic kernel, $\beta = 1.28$, $\gamma_{HG} = 2$ in the disk and the steel tip), averaged over its outputs 0.05 ms apart in the last 3 ms of the plateau; piston at the top. (**a**) Von Mises stress of the simulation; color scale saturated at its upper end; red isolines every 2 MPa, marked on the color bar. (**b**) Local error against the solution of Hondros with the loaded arcs of Equation (A6), on a logarithmic color scale.

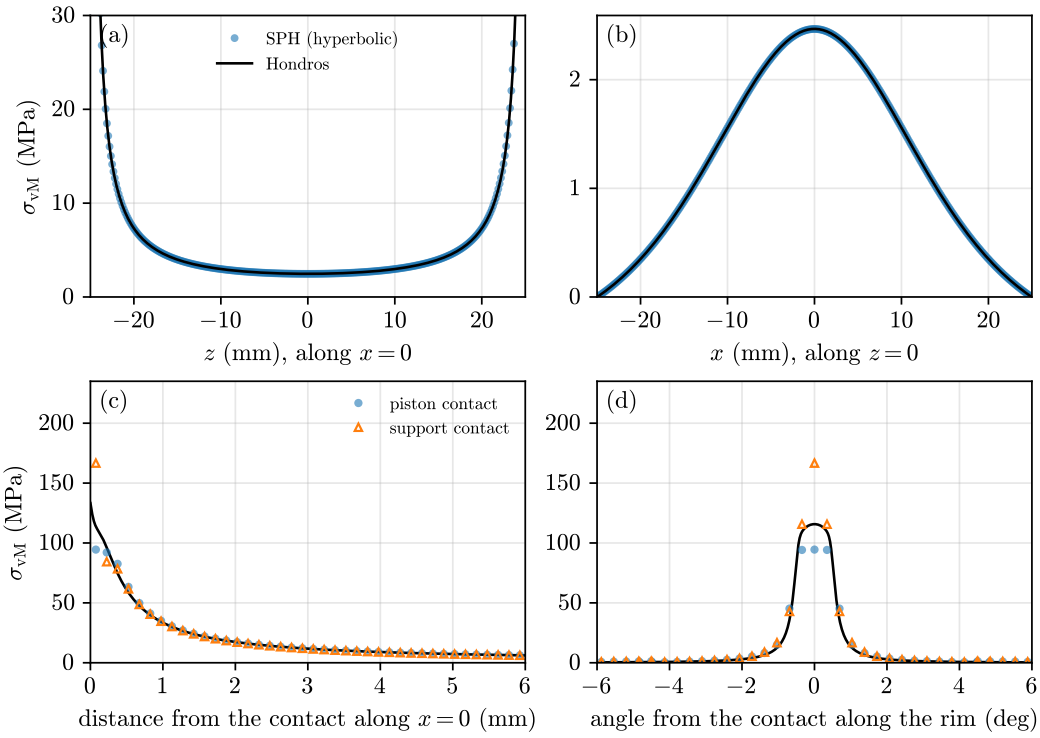


Figure 19. Theoretical validation: von Mises stress of the simulation of Figure 18 (symbols) and of the solution of Hondros with the loaded arcs of Equation (A6) (black line): (**a**) along $x = 0$; (**b**) along $z = 0$; near the contacts, (**c**) along $x = 0$, against the distance from the contact point, and (**d**) along the outermost particles, against the signed angle from the contact point seen from the center, with the solution at their mean radius. In (**c**,**d**), blue filled circles: piston contact; orange open triangles: support contact.

According to Saint-Venant's principle [57], statically equivalent loads produce identical stress fields away from the loaded region. Consequently, along the loading axis, these localized discrepancies stay within about two and a half arc half-widths of each contact point; farther into the domain, the simulated field depends primarily on the net load

F_N. Along the outermost particles, Figure 19d illustrates the stress concentration beneath the loaded arc (which has a half-angle of 0.46°). This stress falls below 10% of its peak value at approximately 1° from the contact point. The simulation accurately captures this profile, except within about 1° of the contact points, at the five particles closest to the piston contact and the three closest to the support. As expected, the error is heavily localized at the contacts, with 75% of the total error contained within 1 mm of the contact points and 84% within 2 mm, regions that encompass only 0.16% and 0.64% of the total particles, respectively. Consequently, the precise error magnitude is highly sensitive to the arc width assumed for the analytical solution, which is analyzed in Appendix B; with an arc of fixed width the error is about twice as large (Appendix G).

4.3.2. Experimental Validation

The staged load of Section 3.7.2, shown in Figure 20, has four plateaus, 53.7, 78.8, 107.0 and 173.1 kN m^{-1}, within 0.7% of the load per unit thickness recorded for each photograph.

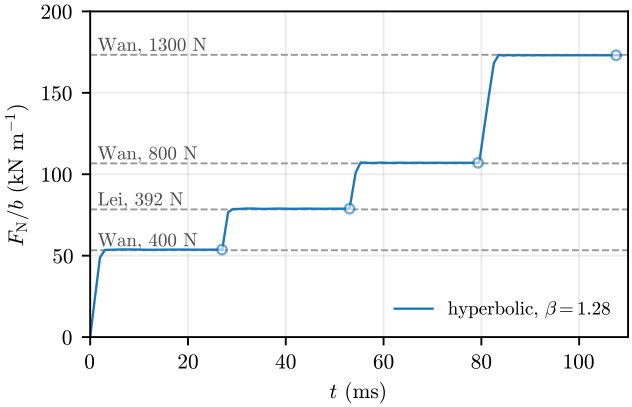


Figure 20. Experimental validation: load per unit thickness, F_N/b, against time t in the staged simulation, hyperbolic kernel, $\beta = 1.28$ and $\Delta p = 0.15$ mm, with the other parameters at the baseline of the Convergence map. Dashed lines: loads per unit thickness of the four photographs; circles: evaluation instants.

Figure 21 presents a comparison between the experimental photograph from Lei et al. [36] at 392 N (Figure 21a) and the simulated image (Figure 21b). The fringes coincide closely from the center outward, except near the edge of the disk where Lei et al. [36] reported residual stresses in the specimen. Along the horizontal and vertical diameters, the dark fringes in the photograph deviate on average by 0.07 and 0.23 mm from the simulated ones, which is comparable to the 0.12 mm pixel resolution of the published image. Because Lei et al. [36] calibrated the photoelastic material fringe value f_σ, which scales every fringe order, using this same photograph, the agreement is partly built-in, meaning this comparison primarily validates the fringe shapes. In contrast, f_σ in Wan et al. [37] was calibrated before their benchmark comparison, so their photographs also validate the fringe orders.

In the red channel, 39.9% of the pixels of the experimental photograph are saturated (Figure 21a). To ensure a more accurate comparison, the simulated image was processed using a tone curve estimated from the photograph itself; the details of this procedure are provided in Appendix H.

Similarly, the three experimental photographs from Wan et al. [37] and their corresponding numerical comparisons are presented in Figure 22. The number, shape and load-dependent evolution of the fringes coincide closely, except for minor discrepancies. As summarized in Table 6, the fringe positions agree within 0.23 mm along the horizontal diameter at 1300 N, and within 0.32–0.96 mm across the other comparisons. This variation likely arises because the published figure of Wan et al. [37] is a compressed composite

image with insets and because, at 400 and 800 N, the fringes are fewer and broader, so their minima are located less precisely. The ratio of the central fringe order to the plateau load F_N remains constant across the three loading stages of Wan et al. [37] to within 0.2%. The experiment itself deviates from linearity by 1% to 2.5% [37], which accounts for part of the discrepancy.

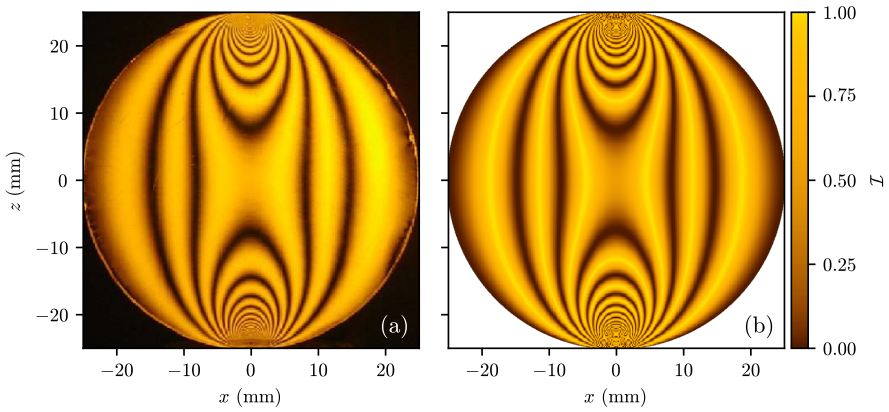


Figure 21. Experimental validation against Lei et al. [36]. (**a**) Photograph at 392 N, Figure 3a of that work, cropped. (**b**) The dark-field image of the staged simulation at the plateau nearest to the load per unit thickness of the photograph, with $b_e = 5$ mm and $f_\sigma = 7.334$ N mm^{-1}, painted with the colors of the photograph through a tone curve estimated from it (Appendix H). Color bar: the intensity $\mathcal{I}$ of Equation (32). Reprinted with permission from Ref. [36]. Copyright 2009 Elsevier.

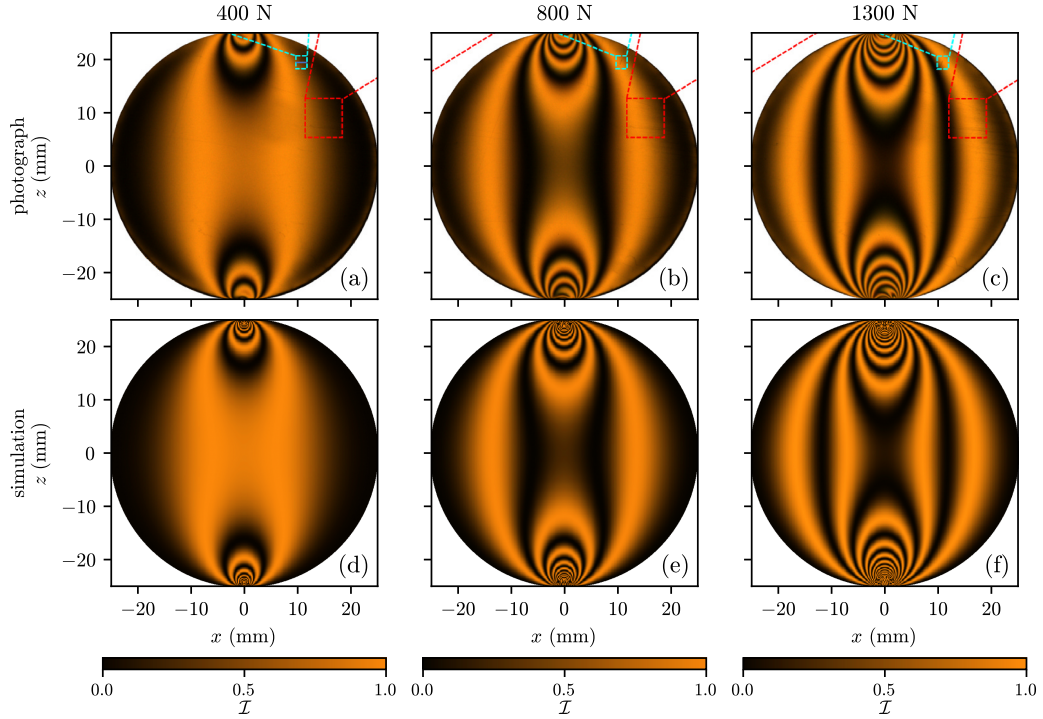


Figure 22. Experimental validation against Wan et al. [37]. (**a**) 400, (**b**) 800 and (**c**) 1300 N: their photographs, Figure 2a–c of that work, cropped; the red boxes, dashed lines and cyan marks belong to its insets. (**d**–**f**) The dark-field image of the staged simulation at the plateau nearest to the load per unit thickness of the photograph above, with $b_e = 7.5$ mm and $f_\sigma = 34.95$ N mm^{-1}, painted with the colors of the photograph (Appendix H). Color bars: the intensity $\mathcal{I}$ of Equation (32). Reprinted with permission from Ref. [37]. Copyright 2026 Elsevier.

Near the contacts, the agreement degrades. Within 1.5–3.4 mm of these regions, the simulated images exhibit a Moiré pattern [61]. In this area, the fringe spacing is less than

two particle widths, falling below the Shannon sampling limit [62], which prevents the images from resolving the fringes.

Table 6. Staged simulation (hyperbolic kernel, $\beta = 1.28$) against the photographs, at the plateau nearest to the load per unit thickness of each photograph, F_e/b_e; rows in that order. Central order: simulated fringe order N_f at the center of the disk, used to check its linearity with the load (Section 4.3.2). Fringe position: mean distance between the dark fringes of the photograph and the simulated ones along the horizontal (h) and vertical (v) diameters, leaving out 3.5 mm next to each contact; at 400 N the horizontal diameter has no dark fringe.

Photograph	F_e (N)	Central Order	Fringe Position (mm)
Wan et al. [37], Figure 2a	400	0.588	v: 0.72
Lei et al. [36], Figure 3a	392	2.741	h: 0.07; v: 0.23
Wan et al. [37], Figure 2b	800	1.172	h: 0.96; v: 0.32
Wan et al. [37], Figure 2c	1300	1.898	h: 0.23; v: 0.70

A more quantitative comparison is shown in Figure 23, where the simulation reproduces the profile of $\sigma_1 - \sigma_2$ measured along the horizontal diameter at 1300 N. In the central 26×26 mm^2 square where Wan et al. [37] evaluate their measurement, it departs from the measured profile by 0.053 MPa on average and 0.15 MPa at most. The other differences are ascribed to the measurement: steps next to the fringes, which Wan et al. [37] attribute to their reconstruction, and a rise of 0.5–0.8 MPa within 2 mm of the boundary, where the simulated difference vanishes.

In the experiments, the load is transmitted over a finite width set by the contact between the disk and the fixtures of the testing machine. In contrast, in the numerical model the loads are applied through 90° wedges, with the support bonded to the disk and the steel tip coupled to it (Section 4.3.1), and the load is applied faster and read at rest, which the Loading-rate test supports (Section 4.1.2). These differences act only near the contacts, within the Moiré zone, where the fringes are too dense for the simulated images to resolve and are also the hardest to locate in the photographs. Away from the contacts, they leave the field practically unchanged (Section 4.3.1), as shown for the contact width and for the friction at the fixtures in the diametral compression test [63,64], and as Wan et al. [37] also note for the analytical solution. The comparison therefore leaves out 3.5 mm next to each contact (Table 6), and the profile is compared within the central square of Wan et al. [37].

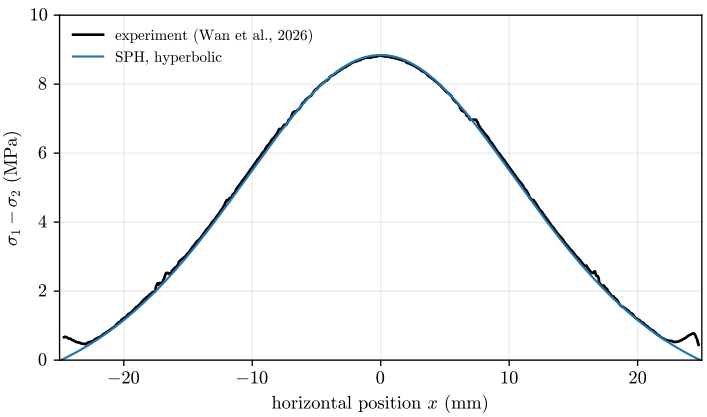


Figure 23. Experimental validation: principal stress difference at 1300 N against the position x along the horizontal diameter ($x = 0$ at the center of the disk), measured by Wan et al. [37] and digitized from their Figure 12a (black), and from the staged simulation with the hyperbolic kernel, $\beta = 1.28$ (blue).

5. Conclusions

The analytical solution is static, so the stresses are read in the rest stage, from the rest time t_r at which the fit of the dimensionless kinetic energy falls to the reading threshold of 0.01. The disk is then effectively at rest: in the Damping test its kinetic energy at t_r is 3.2×10^{-6} of its internal energy, and in the checked simulations of the Convergence map the principal stress difference departs from its final value by at most 3.6×10^{-3} in relative L_1 norm. This state is practically independent of how it is reached: in the Loading-rate test, over two decades of piston velocity, the error changed by at most 1.1%, which supports loading the disk much faster than in the experiments, and in the Resolution–damping test (Appendix E), with the Wendland C^2 kernel, α changed it by less than 0.2%.

The artificial viscosity governs how quickly the disk reaches rest, with a decay rate linear in α. This parameter is also critical for numerical stability: below $\alpha = 0.55$ for the cubic spline and hyperbolic kernels, and below $\alpha = 0.5$ for the Wendland C^2 kernel, no simulation of the damping test reached equilibrium. This minimum stable α grows with γ_{HG} roughly as $\gamma_{HG}/4$ in short runs, almost equally for the three kernels, and grows as the spacing is refined, roughly as $\Delta p^{-0.35}$. Above these thresholds, α is selected by computational cost, which is minimized within $\alpha = 1.78$–1.85. The baseline therefore uses $\alpha = 1.8$, whereas $\alpha = 1.1$ increases the cost by 37% to 41%. Additionally, the Wendland C^2 kernel requires a Courant number below 1 when $\beta \geq 1.5$, and some of its simulations at $\beta = 1.30$–1.72 used 0.80 or 0.60.

Unlike the loading rate and the artificial viscosity, the hourglass control alters the error substantially. At $\gamma_{HG} = 2$, the error is 7.3–8.5 times lower than without control; even at $\gamma_{HG} = 0.1$, the optimum reported for fluid–structure interaction [46], the error remains 2.1–2.6 times higher than that obtained at $\gamma_{HG} = 2$. This control strategy stiffens the loaded system: at $\gamma_{HG} = 2$, the load at a given piston displacement is 16.2–17.1% higher than without control, 9.9–13.4% from the disk itself. Because of this artificial stiffness, introduced without adding measurable damping, the piston displacement must be recalibrated to achieve a target load. At $\gamma_{HG} = 2$, the error for every kernel stays within 5.1% of its minimum, which occurs at $\gamma_{HG} = 3$–4, where a standard run increases the computational cost by approximately 10% to 16%.

With these settings, all 6438 simulations of the Convergence map reach the rest stage, and their error over all zones converges to first order in h along branches of constant β: $\zeta = 0.94$–1.07 on $\beta = 0.98$, 1.48 and 1.98 and 0.93–1.08 on every constant value of $\beta \geq 1$; at the finest spacing the error is linear in h to within 1.5%. The optimal constant term is zero for all nine branches fitted, as expected for the corrected kernel gradient. Within the evaluated resolutions and assuming a constant convergence order, any potential error floor lies below 28% of the error at the finest resolution for 90% of the values of $\beta \geq 1$; this value reflects a limitation of the swept range rather than definitive proof that no floor exists. At a given resolution h, the error depends on β primarily when $\beta < 1.5$. Specifically, the error exhibits discontinuities, increasing by 13%, 24% and 10% where the support domain intersects an axial layer of the lattice at $\beta = 1$, 1.5 and 2, respectively. The optimal β lies between 1.16 and 1.20–1.22 for the cubic spline and hyperbolic kernels and between 1.22 and 1.30 for the Wendland C^2 kernel, with medians of 1.18 and 1.26, respectively. The lowest error at each spacing decreases from 0.06–0.07 at $\Delta p = 3$ mm to 0.0026–0.0030 at $\Delta p = 0.15$ mm.

The contact zones dictate the error over all zones. Their localized errors, with medians of 0.09–0.61 compared to 0.010–0.021 in the interior, converge within zones of fixed size. However, because the analytical stress inside these zones amplifies as the loaded arcs narrow, their relative contribution to the total error increases from 7–12% at $\Delta p = 1$ mm to 51–78% at $\Delta p = 0.15$ mm. This share is highly sensitive to the chosen partition boundary.

For the interpolation operator alone, the contacts also govern the convergence order. The SPH operator applied to the exact displacement field converges to first order over all zones, but recovers second-order convergence once a fixed neighborhood around the contact points is excluded, even with the free boundary included. This confirms the hypothesis proposed in the Introduction for the interpolation. The full simulation, however, does not attain this theoretical bound. Away from the contacts, it converges to first order, yielding an order of 0.9–1.2 in the interior beyond $0.3\,R_{\mathrm{ef}}$. The higher convergence orders observed when only the contact zones are excluded originate from the rim and a quadratic component near the contacts. This first-order behavior stems from the discrete solution itself rather than the interpolation. This outcome is consistent with error pollution propagating from the contacts, potentially combined with effects from the geometry discretization, which the current data cannot decouple. These conclusions remain unaltered with a loaded arc of fixed width, and no definition of the radius raises the order over all zones appreciably above 1 (Appendix G).

For the theoretical validation, the first plateau of the staged simulation, conducted at $\Delta p = 0.15$ mm using the hyperbolic kernel and $\beta = 1.28$, yields an error of $\varepsilon(\sigma_{\mathrm{vM}}) = 0.0028$ against the Hondros solution. Along the loading axis, both solutions agree within 5% from a distance of 0.53 mm outward from the contact points. The error is heavily localized at the contacts, with 84% of the total error concentrated within 2 mm of these regions, where only 0.64% of the particles reside; consequently, its magnitude is highly sensitive to the arc width assumed for the analytical solution.

In the experimental validation, a single staged simulation accurately reproduces the photoelastic fringe patterns reported by Lei et al. [36] and Wan et al. [37] across the four photographed loading conditions, with dark fringe positions deviating on average by 0.07–0.96 mm from the experimental data. At a load of 1300 N, the numerical profile of $\sigma_1 - \sigma_2$ along the horizontal diameter departs from the measured values by an average of 0.053 MPa within the central square region. The comparison with Lei et al. [36] primarily validates the fringe shapes because their material fringe value was calibrated using the same photograph; discrepancies near the disk edge are consistent with the residual stresses reported by the authors. In contrast, the comparison with Wan et al. [37] additionally validates the fringe orders. Within 1.5–3.4 mm of the contacts, the simulated fringes are separated by less than two particle widths, falling below the resolution limit. Furthermore, the idealized 90° wedges used in the numerical model differ from the actual experimental fixtures.

The artificial viscosity and the hourglass control transfer to other elastic contact problems to different extents. The cost-optimal α lies at the elbow of Equation (A8) when Δt_α enters the adaptive time step, and it is otherwise model dependent [4], while its stability threshold depends on the problem (Appendix F). The optimal hourglass coefficient depends on the system studied. Ganzenmüller [21] found $\gamma_{\mathrm{HG}} = 50$ for a beam in bending, with the highest convergence rate and the lowest error, and O'Connor and Rogers [46] found $\gamma_{\mathrm{HG}} \approx 0.1$ for fluid–structure interaction, whereas for plane-stress bodies under concentrated loads this work found $\gamma_{\mathrm{HG}} \approx 2$, with a low error at a moderate cost, so the hourglass control should be checked in each elastic configuration. Finally, β within the optimal ranges given above avoids the error jumps at $\beta = 1$, 1.5 and 2, and the contacts, which carry most of the error, are where refinement pays most.

The three stability tests, and consequently the selection of α and γ_{HG}, were performed exclusively at their baseline resolution, with the Resolution–damping test of Appendix E checking α at four resolutions with Wendland C^2 alone. Similarly, the Convergence map was evaluated solely at $\gamma_{\mathrm{HG}} = 2$. Because the parameter sweep only reaches $n_{\mathrm{nb}} \approx 50$, it does not assess the asymptotic limit $n_{\mathrm{nb}} \to \infty$. Future work should investigate this limit

by considering $\beta > 2$ and finer resolutions reaching $\Delta p < 0.15$ mm. Additionally, further research is required to explain the resolution dependence of the minimum stable α, and to decouple the two potential sources of the first-order convergence observed away from the contacts. Finally, implementing adaptive resolution strategies or specialized boundary treatments could mitigate the local loss of accuracy near concentrated contact loads.

Author Contributions: Conceptualization, L.F.P. and L.D.G.S.; methodology, L.F.P. and I.C.-M.; software, L.F.P.; validation, L.F.P. and L.D.G.S.; formal analysis, L.F.P.; investigation, L.F.P.; resources, I.C.-M. and J.K.; data curation, L.F.P.; writing—original draft preparation, L.F.P.; writing—review and editing, L.D.G.S., I.C.-M. and J.K.; visualization, L.F.P.; supervision, J.K.; project administration, I.C.-M.; funding acquisition, I.C.-M. and J.K. All authors have read and agreed to the published version of the manuscript.

Funding: The research work described in this paper was supported by the Secretaría de Ciencia, Humanidades, Tecnología e Innovación (SECIHTI) through a doctoral scholarship (CVU No. 1180978). The resources employed were provided by the Laboratorio de Investigación de la Eficiencia Energética en Sistemas Térmicos of the Instituto Politécnico Nacional of Mexico, LIEEST—IPN (Grant No. SIP-20260151).

Data Availability Statement: The original contributions presented in this study are included in the article. Further inquiries can be directed to the corresponding author.

Acknowledgments: Financial support from SECIHTI and the Instituto Politécnico Nacional (ESIME-Zacatenco) through the provision of resources and facilities is gratefully acknowledged. Access to the facilities of the Universidad Autónoma Metropolitana, Azcapotzalco Campus (UAM-A), and to the computing cluster of the Instituto Nacional de Investigaciones Nucleares (ININ), is also appreciated. The authors further thank Franklin Peña-Polo for his valuable advice and guidance. During the preparation of this work, the authors used Google Gemini 3.1 Pro to assist with the generation of auxiliary Python 3.14 scripts (.py). These scripts managed the remote execution queue, local data downloading, and curation for thousands of simulations. The authors also used Claude Opus 5.5 (Anthropic) to draft and edit parts of the text, to write the analysis and plotting scripts of the figures, and to check the consistency of the manuscript. The authors have reviewed and edited the output and take full responsibility for the content of this publication.

Conflicts of Interest: The authors declare no conflicts of interest. The funders had no role in the design of the study; in the collection, analyses, or interpretation of data; in the writing of the manuscript; or in the decision to publish the results.

Appendix A. Interpolating Kernels

The three SPH kernel functions considered in this work are the cubic spline [49], the Wendland C^2 [50] and the hyperbolic kernel [51]. The first two are among the most widely used smoothing kernels in the literature [52]. The hyperbolic kernel has a non-negative second derivative throughout its support domain. This property prevents the repulsive interparticle force from weakening as particles approach under compression, thereby mitigating particle clustering. For the momentum equation with the kernel evaluated at the current positions, the stability analysis of Swegle et al. [16] shows that the particle motion becomes unstable when $\sigma W'' > 0$, where σ is the one-dimensional Cauchy stress, and W'' is the second derivative of the kernel. The cubic spline and Wendland C^2 kernels change the sign of W'' within their support, so they can be unstable under tension or compression. The hyperbolic kernel, with $W'' \geq 0$, is stable under compression [16,51], which is the dominant state near the contacts of a diametrically loaded disk. The present model defines the elastic force in the reference configuration, and the total Lagrangian form of Equation (1) helps mitigate this instability [19].

In d-dimensional space, the cubic spline kernel has the form:

$$W(q,h) = \frac{\Lambda_d}{\pi h^d} \begin{cases} 1 - \frac{3}{2}q^2 + \frac{3}{4}q^3 & q < 1, \\ \frac{1}{4}(2-q)^3 & 1 \le q < 2, \\ 0 & q \ge 2, \end{cases} \tag{A1}$$

where $q = x^{ij}/h$, $x^{ij} = |\mathbf{x}^i - \mathbf{x}^j|$ is the interparticle distance, and Λ_d is the normalization factor given by $\Lambda_2 = 10/7$ and $\Lambda_3 = 1$ in 2D and 3D, respectively. The Wendland C^2 function has the form:

$$W(q,h) = \frac{\Lambda_d}{\pi h^d} \begin{cases} (1 - \frac{1}{2}q)^4(1+2q) & q < 2, \\ 0 & q \ge 2, \end{cases} \tag{A2}$$

with $\Lambda_2 = 7/4$ and $\Lambda_3 = 21/16$. Last, the hyperbolic kernel is given by:

$$W(q,h) = \frac{\Lambda_d}{\pi h^d} \begin{cases} q^3 - 6q + 6 & q < 1, \\ (2-q)^3 & 1 \le q < 2, \\ 0 & q \ge 2, \end{cases} \tag{A3}$$

where $\Lambda_2 = 1/3$ and $\Lambda_3 = 15/62$. As shown in Figure A1, the first derivatives of the cubic spline and Wendland C^2 kernels peak in magnitude at $q = 2/3$ and $q = 1/2$, respectively.

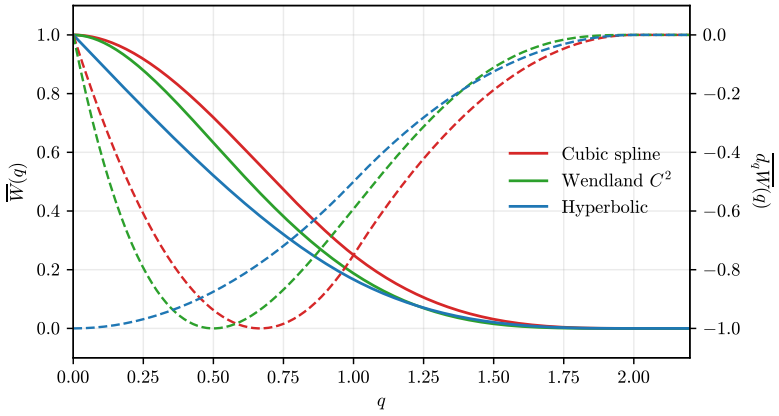


Figure A1. Interpolation kernels divided by their value at $q = 0$, $\overline{W}(q)$ (solid lines, left axis), and their derivatives with respect to q divided by their largest magnitude, $\overline{d_q W}(q)$ (dashed lines, right axis), against q.

Appendix B. Half-Width of the Loaded Arcs

The solution of Hondros [35] loads the disk on two arcs of half-width, $R\psi$, centered on the loading axis. In the model, the load is not applied on a prescribed arc: the steel tip and the support transmit it through the nearest disk particles around them, so $R\psi$ is not a free parameter.

The structural solver fixes its list of interacting pairs at $t = 0$, with every pair at $x_0^{ij} \le 2h$ and no filter by body (Section 3.1). The wedge and the disk therefore stay linked across a band, the region through which the model transmits the load. Each disk particle i is weighted by

$$\tilde{W}^i = \sum_{j \in \mathcal{W},\ x_0^{ij} \le 2h} \overline{W}\left(\frac{x_0^{ij}}{h}\right), \tag{A4}$$

where $\mathcal{W}$ is the set of particles of the steel tip, or of the support for the lower contact, and $\overline{W}$ the kernel divided by its value at $q = 0$. Each disk particle bonded to the wedge is the center of an element of side Δp, whose projection on the boundary is an interval of width Δp centered at x^i, the coordinate of particle i along the boundary measured from the loading axis. Spreading its share of the load uniformly over that interval adds $\Delta p^2/12$ to the variance, so the standard deviation w_b of the band along the boundary is

$$w_\mathrm{b}^2 = \frac{\sum_i \tilde{W}^i \, (x^i)^2}{\sum_i \tilde{W}^i} + \frac{\Delta p^2}{12}. \tag{A5}$$

A uniform load on an arc of half-width $R\psi$ has standard deviation $R\psi/\sqrt{3}$; equating the two,

$$R\psi = \sqrt{3}\, w_\mathrm{b}, \qquad \xi = \frac{R\psi}{\Delta p} = \frac{\sqrt{3}\, w_\mathrm{b}}{\Delta p}. \tag{A6}$$

A single bonded particle gives $\xi = 1/2$; a pair at exactly $2h$ has zero weight, so ξ is continuous at the cut; and ξ grows with β to 2.1–2.2 at $\beta = 2$, almost independently of Δp (Figure A2). Since the band is about $2h$ wide, $R\psi \propto h$ at fixed β.

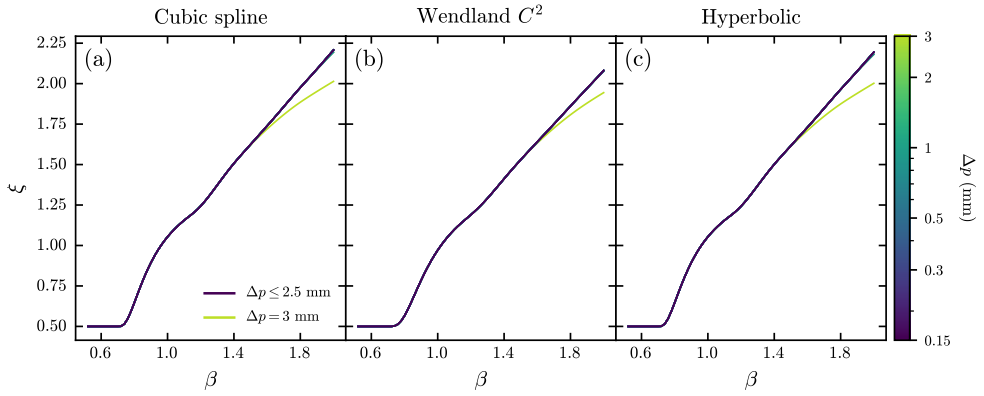


Figure A2. Half-width of the loaded arc in particle spacings, ξ, Equation (A6), against the smoothing-length ratio, β, one curve per spacing Δp, for the (**a**) cubic spline, (**b**) Wendland C^2 and (**c**) hyperbolic kernels; the curves for $\Delta p \leq 2.5$ mm coincide.

Appendix C. The Load Carried by the Chords

The amplitude of the solution of Hondros [35] depends on the normal load, F_N, which is obtained directly from each simulation. Each chord, a horizontal row of disk particles, transmits the vertical force Q_ℓ of Equation (20). The difference between the forces of two chords is the inertia of the part of the disk between them, which the artificial viscosity damps out. As the system reaches equilibrium, every chord away from the contacts carries the same force, whatever its length, and that force is the load on the upper arc. The load is the median of Q_ℓ over the chords with $|z| \leq 0.6R_\mathrm{ef}$:

$$F_\mathrm{N} = \underset{|z| \leq 0.6R_\mathrm{ef}}{\mathrm{median}}\, Q_\ell, \tag{A7}$$

where z is the height of chord ℓ. A simulation is discarded when the spread of those chords, $(\max Q_\ell - \min Q_\ell)/F_\mathrm{N}$, exceeds 0.75.

Figure A3 shows Q_ℓ/F_N over the whole height of the disk, averaged over the outputs saved 0.05 ms apart in the rest stage, for six initial spacings.

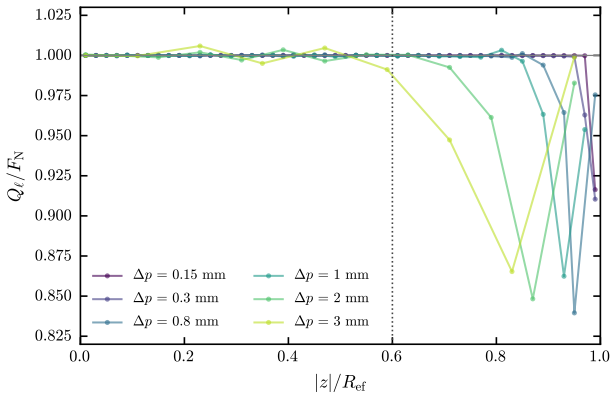


Figure A3. Vertical force carried by each row of the reference lattice over the load, Q_ℓ/F_N (Equations (20) and (A7)), against the height of the row, $|z|/R_{ef}$ (upper and lower halves together), averaged over the rest stage of each simulation. Each curve is one spacing Δp: the median over the simulations with $\beta \geq 0.9$ of the three kernels. The dotted line bounds the rows used for F_N, $|z| \leq 0.6R_{ef}$.

Away from the poles, the rows carry the same force to within 2×10^{-4}, between the 5th and 95th percentiles of the simulations with $\beta \geq 0.9$ and $\Delta p \leq 0.5$ mm, up to $|z| = 0.74\, R_{ef}$. The force departs from F_N by more than 0.1% only within about $6\,\Delta p$ of each pole, where the rows cross the band bonded to the wedge or lie within a support radius of it. This region extends 0.8 mm from the pole at $\Delta p = 0.15$ mm and 5.5 mm at $\Delta p = 1$ mm, and covers most of the disk at $\Delta p = 2$ and 3 mm, which have about twelve and eight rows, respectively, on each side of the center.

Table A1 compares bands $|z|/R_{ef}$ against the median of the central rows, $|z| \leq 0.3R_{ef}$. The band $|z| \leq 0.6R_{ef}$ is the widest one whose chords all carry the same force to within 0.13% up to $\Delta p = 1$ mm; wider selections take in rows near the bonded band, up to 0.43%, 1.4% and 23% off at $0.7R_{ef}$, $0.8R_{ef}$ and $0.9R_{ef}$. At the coarsest spacings, no band is free of them: at $\Delta p = 3$ mm the worst row of $|z| \leq 0.6R_{ef}$ is 11% off, and the median still keeps F_N within 0.82%.

Averaged over the outputs saved 0.05 ms apart in the rest stage, the spread of the rows used has a median of 0.14% over the 6438 map simulations, a 99th percentile of 5.8% and a maximum of 11.8% (at $\Delta p = 3$ mm). Because the spread never reaches the threshold of 75% at any recorded instant, no simulation is discarded.

Table A1. Bands of rows up to $|z|/R_{ef}$ against the median of the central rows, $|z| \leq 0.3R_{ef}$: largest relative change of F_N/largest departure of a row, over the simulations with $\beta \geq 0.9$ of the three kernels.

$\|z\|/R_{ef}$	$\Delta p = 0.5$ mm	1 mm	2 mm	3 mm
0.5	0.003%/0.03%	0.01%/0.13%	0.21%/0.7%	0.76%/1.5%
0.6	0.003%/0.03%	0.01%/0.13%	0.27%/1.4%	0.82%/11%
0.7	0.006%/0.03%	0.03%/0.43%	0.21%/1.7%	0.82%/11%
0.8	0.008%/0.04%	0.03%/1.4%	0.27%/22%	0.95%/19%
0.9	0.01%/1.5%	0.03%/23%	0.42%/27%	0.95%/27%

Appendix D. Lattice of the Disk at the Contact Points

The particles of the disk and the two wedges are generated on a square lattice of spacing Δp, aligned with the axes and centered on the disk, and a site (a particle location) belongs to the disk when it lies inside the circle of radius R. The tip of each wedge is a single particle, one lattice row above/below the disk. The row of the disk nearest each contact point therefore lies a distance $\mathrm{frac}(R/\Delta p)\,\Delta p$ below R, where frac

is the fractional part, and holds n_{pole} particles; both change irregularly from one spacing to the next, as shown in Figure A4a for the distance at the 29 spacings of the Convergence map. Unless $\mathrm{frac}(R/\Delta p) = 1/2$, the edge of the discrete disk is not at R; this is why the solution of Hondros [35] is evaluated on the effective radius defined by Equation (21).

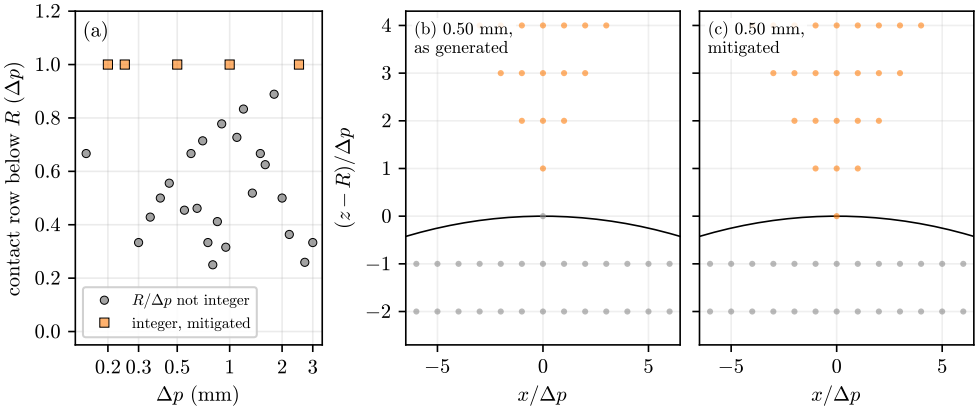


Figure A4. Lattice of the disk at the upper contact point. (**a**) Distance of the contact row below R, in units of Δp, against Δp, for the 29 spacings of the Convergence map: $\mathrm{frac}(R/\Delta p)$ when $R/\Delta p$ is not an integer (gray), and 1 at the five integer spacings, after the mitigation (orange). (**b**,**c**) Disk particles (gray), upper wedge (orange) and circle of radius R (line) near the contact at $\Delta p = 0.50$ mm ($R/\Delta p = 50$), in units of Δp: (**b**) as generated, with one particle on the circle; (**c**) with the mitigation.

When $R/\Delta p$ is an integer, which happens at Δp of 0.20, 0.25, 0.50, 1.0 and 2.5 mm, the outermost sites in the lattice lie exactly on the circle at R and the particle generator (GenCase v5.0.278c, the pre-processing tool of DualSPHysics that generates the initial particle distribution) includes them or not depending on rounding. At these spacings, the disk keeps a single particle at R at one contact (Figure A4b) and a full row one spacing below R at the other, and the two wedges are no longer mirror images of each other: they differ by 22 to 206 sites.

Before each simulation, a pre-run script accepts the geometry only if (i) the whole disk is symmetric left to right and top to bottom, (ii) both wedges are triangles with a half-angle of 45° and mirror images site by site, (iii) each wedge lies one spacing from the disk, and (iv) the piston clamp covers the base of the steel tip. When the check fails, the radius of the disk is reduced by $0.01\,\Delta p$ and the tip of each wedge is placed one row above/below the disk. This mitigation removes the rounding ties. A geometry that still fails is not run.

With the mitigation, the disk is symmetric at the five integer spacings: its contact row lies one full spacing below R (Figure A4c) and it holds more particles than at the neighboring spacings, $n_{\mathrm{pole}} = 19$ at 0.50 mm against 15 at 0.45 mm and 13 at 0.55 mm. Shifting the lattice by $\Delta p/2$ instead, which would place that row at $R - \Delta p/2$, cannot be done with the generator: moving the origin of the lattice moves the bodies with it, and a translation of the bodies is rounded to a whole number of spacings.

Appendix E. Supplementary Results

This appendix collects the details cited in Sections 3 and 4: the decay law of the Damping test, the Resolution–damping test, the cost of simulation and the decay time over the Convergence map.

Appendix E.1. Decay Law

In the Damping test of Section 4.1.1, the intercepts of Equation (33) are $\lambda_0 = 0.0012 \pm 0.0006$, 0.008 ± 0.005 and 0.0015 ± 0.0005 ms^{-1} for the cubic spline, Wendland C^2 and hyperbolic kernels. The fits use the 14, 15 and 14 values of α, from 0.55, 0.5 and 0.55 to 5, at which $\hat{K}$ decays after the stop, and the decay rates of single simulations scatter about them by a median of 0.2, 1.3 and 0.1%, respectively. Every simulation runs past its t_r, by at least 4.7 ms with the cubic spline and hyperbolic kernels and 1.0 ms with Wendland C^2. To this end, the Wendland C^2 simulation at $\alpha = 0.5$ was continued from 25 to 40 ms. The amplitude Θ of Equation (25) is 0.159–0.184 with the cubic spline, 0.191–0.520 with Wendland C^2 and 0.181–0.277 with the hyperbolic kernel, always above 0.01, so that $t_r > t_p$ in every simulation.

Appendix E.2. Other Resolutions

The Resolution–damping test checks at four resolutions that α does not change the error in the rest stage and that there is a minimum α at which the simulation remains stable. It runs $\alpha \in \{0.55, 1.1, 2.2\}$ at $\Delta p \in \{0.2, 0.3, 0.6, 0.8\}$ mm with the Wendland C^2 kernel only, the other parameters at the baseline of the stability tests, and a push of $t_p = 5$ ms. Its displacement, 0.144–0.189 mm, grows as Δp decreases so that the normal load reaches $F_N/b = 54.2$–55.6 kN m^{-1}. Each of the 12 simulations continued for 10 to 55 ms after the stop, longer at small α and small Δp.

At $\Delta p = 0.2$ and 0.3 mm the simulations with $\alpha = 0.55$ have no rest stage. At 0.2 mm the simulation breaks down during the push: from 3.5 ms on, the chords no longer carry the same load, because the dissipation is too weak to keep the disk in equilibrium. At 0.3 mm the load settles, but the error grows with the simulated time instead of decaying. At $\Delta p = 0.6$ and 0.8 mm, $\alpha = 0.55$ is stable. In the Damping test of Section 4.1.1, the same kernel at $\Delta p = 0.4$ mm is stable down to $\alpha = 0.5$ and fails at 0.45. Together, these results suggest that the minimum stable α grows as Δp decreases. The short runs of Appendix F confirm this trend at five values of γ_{HG}, although they do not separate Δp from other quantities that change with it, such as the piston displacement needed to reach the same load on the chords.

With $\alpha = 1.1$ and 2.2, the error is 0.00534 and 0.00535 at $\Delta p = 0.2$ mm and 0.00865 and 0.00866 at $\Delta p = 0.3$ mm, and at $\Delta p = 0.6$ and 0.8 mm, it is 0.0186 and 0.0232, respectively, and changes with α by less than 0.03%. Over the test, α changes the error in the rest stage by less than 0.2%.

The frequency of the oscillation after the stop is $f = 3.76$, 3.94, 4.27 and 4.42 kHz at $\Delta p = 0.2$, 0.3, 0.6 and 0.8 mm, respectively, an 18% rise, consistent with contacts that stiffen as Δp grows.

Appendix E.3. Cost

In the Damping test, α also sets the cost of a simulation, through the viscous time step Δt_α (Equation (17)). Since $\Delta t_\alpha / (C_{CFL}\, \Delta t_s) = c_s' / (C_{CFL}\, \alpha\, c_0)$, the viscous time step becomes the controlling one when α exceeds the value

$$\alpha = \frac{c_s'}{C_{CFL}\, c_0} = \frac{c_s (1 + \gamma_{HG})^{1/2}}{C_{CFL}\, c_0}, \tag{A8}$$

provided that Δt_s is smaller than Δt_a and Δt_{cv}. This value is the elbow of Section 4.1.1, with $c_s = \max_i c_s^i$; its second form holds when every body has the same γ_{HG}, as here. The cost of each α is compared through a standard run: the push, $t_p = 5$ ms, plus the waiting time $t_r - t_p$ (Equation (26)) with Θ replaced by a fixed amplitude $\Theta^* = 0.52$, the largest Θ of the sweep, so that the comparison does not depend on the amplitude that each simulation

leaves at the stop. Its cost is this simulated time multiplied by the GPU wall-clock time per simulated millisecond.

With $\gamma_{HG} = 2$, Δt_s (Equation (16)) is set by the steel tip, whose particles have the largest $c_s'^i$: $c_s' = 9.12$ km s^{-1} and the elbow is $\alpha = 1.82$ at the $C_{CFL} = 1$ of the Damping test. Figure A5 gives this cost for each simulation, with its own τ and cost per simulated millisecond, and for a cost model, with τ from Equation (33) and a cost per simulated millisecond that is constant below the elbow. This constant, the mean over the simulations with $\alpha \leq 1.5$, is 26.91 ± 0.13 s for the cubic spline, 26.42 ± 0.29 s for Wendland C^2 and 26.93 ± 0.20 s for the hyperbolic kernel.

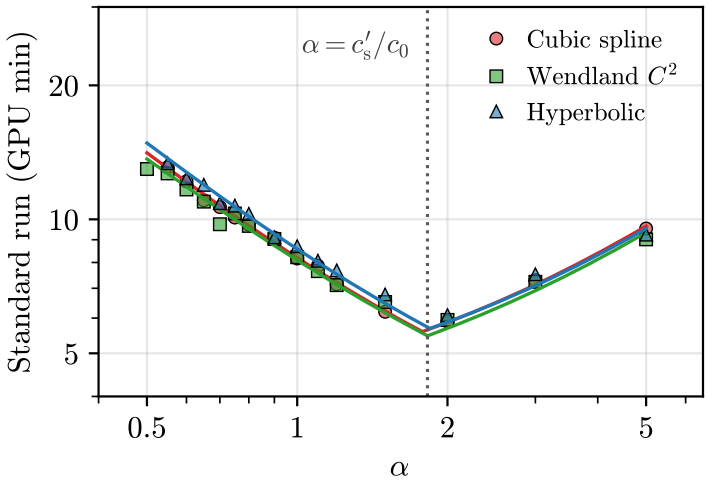


Figure A5. Damping test: GPU wall-clock minutes of a standard run against α, in logarithmic scale, for the three kernels, the other parameters at the baseline of the stability tests. Symbols: simulations; lines: cost model; dotted vertical line: the elbow, above which the viscous time step is the smallest.

Above the elbow, every millisecond costs in proportion to α, with a slope fitted through the origin to the simulations with $\alpha \geq 2$. The two regimes meet, and the modeled cost of a standard run is lowest at $\alpha = 1.781 \pm 0.019$, 1.824 ± 0.052 and 1.845 ± 0.052 for the three kernels, respectively, close to the predicted elbow. At the baseline of the stability tests, $\alpha = 1.8$, the cost is within 1.5% of this minimum, and at $\alpha = 1.1$ it is 37–41% higher. The measured cost per simulated millisecond also depends on the load of the shared GPUs: 26.5–26.8 s at best and 28.9–29.4 s at the median in the Loading-rate test, at $\alpha = 1.8$, and 26.6–27.6 s in the Damping test at $\alpha = 1.1$. Over the Convergence map, on one GPU shared with another of its simulations, a simulation at the finest spacing ($N \approx 9.2 \times 10^4$) takes 1.0–1.5 h ($\beta = 1.98$–$0.98$). Over $\Delta p \leq 0.4$ mm, its cost (time step and time to rest included) grows as $N^{1.20 \pm 0.03}$. This puts $N = 10^6$ at about 1–2 days, or at most about 5 days if the cost per time step becomes proportional to N.

Appendix E.4. Decay Time over the Convergence Map

Over the Convergence map of Section 3.6, τ is measured in the simulations with $\beta = 0.72$–2.00 and $\Delta p = 0.15$–3.00 mm for the three kernels, in those whose decay is resolved by the outputs 1 ms apart. These are 73% of them, all with $h \leq 2.3$ mm; in the others the kinetic energy is already below the reading threshold at the first outputs after the stop. As shown in Figure A6a, τ follows a single power law of the smoothing length h,

$$\tau \propto h^{-1.21}, \tag{A9}$$

whose exponent, fitted by least squares on logarithmic scale, is -1.209 ± 0.004, with a scatter about it that depends on β. Below $\beta \approx 0.75$, τ departs from the law in a way that

depends on the spacing: at $\beta = 0.72$–0.74 it lies below the law for $\Delta p \leq 0.35$ mm, by a median of 25% at 0.15 mm, and above it from $\Delta p = 0.75$ mm on, by medians of 53–120%. Below $\beta = 0.72$, τ departs further, and including those simulations would change the exponent to -1.265 ± 0.010, so they are left out. A viscous decay at a rate proportional to α_{eff}/R^2 would give $\tau \propto h^{-1}$, since α_{eff} (Equation (12)) is proportional to h and the decay rate is linear in α. The extra 0.2 of the measured exponent is not explained.

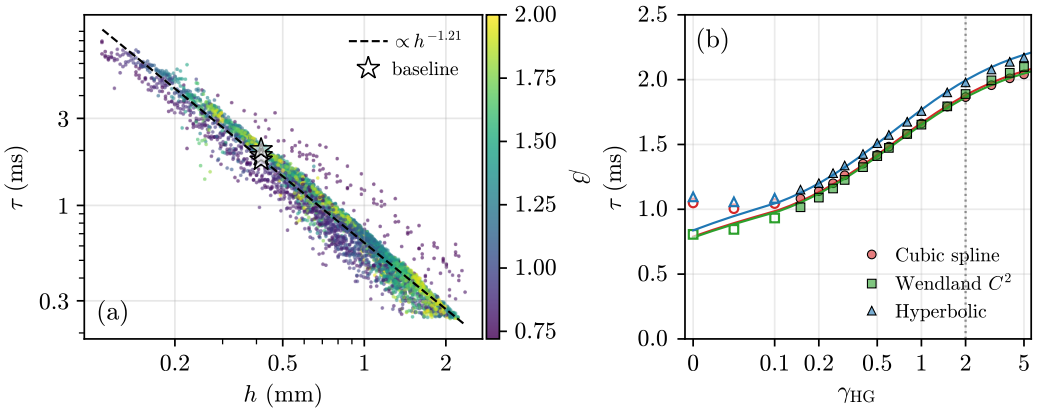


Figure A6. Decay time τ of the dimensionless kinetic energy $\hat{K}$ after the piston stop. (**a**) Against the smoothing length h, for simulations of the Convergence map. Dashed line: power-law fit. White stars: $\beta = 1.04$ and $\Delta p = 0.4$ mm, the baseline resolution of the stability tests, one per kernel. (**b**) Against the hourglass control coefficient γ_{HG} in the Hourglass test. Lines: Equation (A11), fitted to $\gamma_{\text{HG}} > 0.1$; open symbols: $\gamma_{\text{HG}} \leq 0.1$, left out of the fit. Dotted line: $\gamma_{\text{HG}} = 2$, the value of the Convergence map.

The Resolution–damping test separates the two dependences at $\beta = 1.04$ with the Wendland C^2 kernel. Over the ten simulations that reach rest, $\Delta p = 0.2$–0.8 mm and $\alpha = 0.55$–2.2,

$$\tau = 1.12\ \text{ms} \left(\frac{\Delta p}{1\ \text{mm}} \right)^{-1.19 \pm 0.01} \alpha^{-0.98 \pm 0.01}, \tag{A10}$$

with a scatter of 1.1%. The decay rate is thus linear in α at every resolution, as a viscous decay requires, and the exponent of the resolution is close to that of Equation (A9). The waiting time after the stop also depends on the amplitude left at the stop, and scales less cleanly: its exponent in α is -1.00 and -1.14 at $\Delta p = 0.8$ and 0.6 mm, and -0.89 and -0.70 at 0.2 and 0.3 mm, where only two values of α reach rest; with two or three values of α, these exponents have no meaningful error estimate. At $\Delta p = 0.4$ mm and $\beta = 1.04$, the map gives $\tau = 1.88$, 1.78 and 2.03 ms for the cubic spline, Wendland C^2 and hyperbolic kernels, respectively. The Hourglass test at $\gamma_{\text{HG}} = 2$, with the same $\alpha = 1.8$, gives 1.87, 1.89 and 1.98 ms, within 6%, even though the map writes its outputs 1 ms apart during the decay, from which τ is fitted, and the stability tests 0.05 ms apart.

At a fixed resolution, τ depends on the hourglass coefficient of the disk and the tip. In the Hourglass test of Section 4.1.3, at the baseline resolution of the stability tests and $\alpha = 1.8$, with the tip at the same γ_{HG} as the disk, τ follows (see Figure A6b)

$$\tau(\gamma_{\text{HG}}) = A \left[1 + \frac{a_\gamma\, \gamma_{\text{HG}}}{\gamma_{\text{HG}} + \gamma_{\text{c}}} \right], \tag{A11}$$

with $a_\gamma = 1.83 \pm 0.05$ and $\gamma_{\text{c}} = 0.64 \pm 0.03$ common to the three kernels and $A = 0.79$, 0.78 and 0.84 ms for the cubic spline, Wendland C^2 and hyperbolic kernels, respectively. The fit uses the 42 simulations with $\gamma_{\text{HG}} > 0.1$, which scatter about it by 1.2% (root mean square). At $\gamma_{\text{HG}} \leq 0.1$, the departure from the law depends on the kernel. Without control,

τ is 33 and 31% above it with the cubic spline and hyperbolic kernels and 3% above with Wendland C^2; at $\gamma_{HG} = 0.05$ and 0.1, 4–12% above with the first two and 4–5% below with Wendland C^2. A control this weak no longer fully suppresses the zero-energy modes [21], and how these particle-scale modes develop may depend on the kernel, as it does for the pairing instability [65]. The law grows from A at $\gamma_{HG} = 0$ toward $(1 + a_\gamma)A \approx 2.8A$, and at $\gamma_{HG} = 2$ it is 2.4 times its value at $\gamma_{HG} = 0$; in the simulations $\tau(2)/\tau(0)$ is 1.8–2.3. If the dependences on h and on γ_{HG} are separable, which the Convergence map, run at $\gamma_{HG} = 2$ only, cannot test, Equations (A9) and (A11) combine into $\tau(h, \gamma_{HG}) = \tau(h, 2)\, \varphi(\gamma_{HG})/\varphi(2)$, with $\varphi(\gamma_{HG}) = 1 + a_\gamma\, \gamma_{HG}/(\gamma_{HG} + \gamma_c)$.

Appendix F. Minimum Stable Artificial Viscosity

The minimum stable α was measured in short runs of 60 ms with the push of the stability tests, $\beta = 1.04$, $C_{CFL} = 1$ and the same γ_{HG} in the disk and the steel tip. A run counts as stable when it ends without aborting and its last output has $\hat{K} < 1$. At the baseline resolution of the stability tests, $\Delta p = 0.4$ mm, 315 runs swept the three kernels, γ_{HG} from 0 to 5 and α from 0.1 to 1.5 in steps of 0.1 (Table A2). Up to $\gamma_{HG} = 0.5$ every α is stable; above, the minimum stable α grows roughly as $\gamma_{HG}/4$, almost equally for the three kernels. A further 273 runs repeat the search with the cubic spline kernel at $\Delta p = 0.2$, 0.25, 0.3, 0.6 and 0.8 mm, for $\gamma_{HG} = 1$ to 5, and at 0.4 mm for $\gamma_{HG} = 4$, with the push of the Convergence map at each spacing (Table A3). At every γ_{HG}, the minimum stable α grows as the spacing is refined, and the 30 values follow $\alpha_{min} \approx 0.23\, \gamma_{HG}^{0.89\pm0.02}\, \Delta p^{-0.35\pm0.03}$, with Δp in mm and a mean deviation of 5%.

This is consistent with the hourglass control acting as an added stiffness: as γ_{HG} grows, the disk oscillates faster after the stop, by up to 12.9–13.3% at $\gamma_{HG} = 5$ (Figure 7a), and the particle-scale modes that the control penalizes become stiffer. Only the artificial viscosity damps these faster modes, so more dissipation, a larger α, is needed to keep them bounded. With the same α, the kinetic energy also decays more slowly at larger γ_{HG}, $\tau(2)/\tau(0) = 1.8$–2.3 (Appendix E).

Table A2. Minimum stable α against γ_{HG} in short runs at the baseline resolution of the stability tests ($\Delta p = 0.4$ mm, $\beta = 1.04$), with the same γ_{HG} in the disk and the steel tip; a run is stable if it ends without aborting and with $\hat{K} < 1$; ≤ 0.1: stable at every α swept.

	γ_{HG}						
Kernel	**0**	**0.5**	**1**	**1.5**	**2**	**3**	**5**
Cubic spline	≤ 0.1	≤ 0.1	0.3	0.4	0.6	0.8	1.3
Wendland C^2	≤ 0.1	≤ 0.1	0.3	0.4	0.5	0.8	1.2
Hyperbolic	≤ 0.1	≤ 0.1	0.3	0.4	0.6	0.8	1.3

Table A3. Minimum stable α against Δp for the cubic spline kernel; the column at 0.4 mm comes from Table A2, except for $\gamma_{HG} = 4$.

Δp (mm)	0.2	0.25	0.3	0.4	0.6	0.8
$\gamma_{HG} = 1$	0.4	0.4	0.4	0.3	0.3	0.2
$\gamma_{HG} = 2$	0.7	0.7	0.7	0.6	0.5	0.5
$\gamma_{HG} = 3$	1.0	1.0	1.0	0.8	0.8	0.7
$\gamma_{HG} = 4$	1.4	1.3	1.2	1.1	1.0	0.9
$\gamma_{HG} = 5$	1.7	1.6	1.5	1.3	1.1	1.0

Appendix G. Sensitivity to the Analytical Solution

Two alternatives were examined: an analytical solution whose loaded arc does not depend on the discretization, which does not change the conclusions of Section 4.2, and other definitions of its radius, none of which raises the order over all zones appreciably above 1.

Appendix G.1. An Analytical Solution with a Fixed Arc

With the bonded band, the half-width of the loaded arcs, $R\psi = \xi \Delta p$, is computed as in Appendix B and is proportional to h at fixed β. To check that this choice is not what keeps the order of convergence below 2, the zone exclusions of Section 4.2.5 were repeated on the same simulations with a half-width $R\psi_{\mathrm{T}}$ that does not depend on the discretization, given by the elastic contact of a 90° wedge, with faces inclined at 45°, pressed against a half-plane in plane stress (Equations (1) and (4) of Truman et al. [66]):

$$R\psi_{\mathrm{T}} = \frac{F_{\mathrm{N}}}{b} \frac{1}{\tan 45^{\circ}} \left(\frac{1}{E} + \frac{1}{E_{\mathrm{p}}} \right) = 0.0216 \text{ mm}, \tag{A12}$$

where $F_{\mathrm{N}}/b = 53.3$ kN m^{-1} is the nominal load, and $E = 2.5$ GPa and $E_{\mathrm{p}} = 200$ GPa are the Young moduli of the disk and of the steel tip.

With the fixed arc (Figure A7), the order over all zones along the three branches is 0.91–0.98 for the simulation and 0.98–1.02 for the operator alone. When the contact zones are excluded, the order of the simulation peaks at 1.47–1.69 and then settles at 1.21–1.53, never reaching 2, whereas the operator alone reaches 2 by $s_{\min} \approx 0.1$–$0.2\, R_{\mathrm{ef}}$, against 0.10–$0.25\, R_{\mathrm{ef}}$ with the band (Section 4.2.5). The order with the fixed arc is thus close to that with the band, but its error, on average over the swept spacings, is 2.0, 2.7 and 2.3 times larger over all zones along the three branches, and 1.1–1.3 times larger in the interior and rim at $s_{\min} = 0.3\, R_{\mathrm{ef}}$.

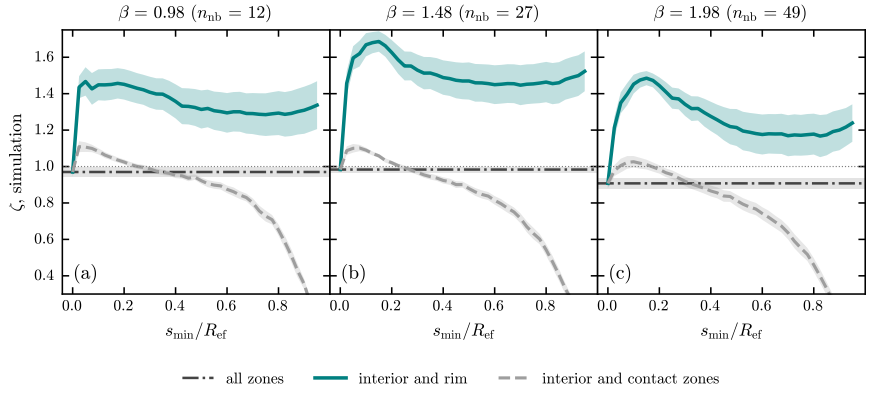


Figure A7. Order of convergence of the error of the simulation, ζ, against the threshold of the contact zones and the rim, $s_{\min}/R_{\mathrm{ef}}$, along the branches (**a**) $\beta = 0.98$, (**b**) 1.48 and (**c**) 1.98 of the Convergence map; the error is relative to the analytical solution with loaded arcs of fixed half-width $R\psi_{\mathrm{T}} = 0.0216$ mm, Equation (A12). Mean of the three kernels, with one standard deviation from a bootstrap over Δp (bands). Dark gray, dash-dotted: all zones; teal, solid: interior and rim; silver, dashed: interior and contact zones.

Appendix G.2. Radius of the Analytical Solution

The analytical solution was evaluated with the radius

$$R_{\mathrm{ef}} = \frac{z_{\max} - z_{\min}}{2} + \lambda_R \, \Delta p, \tag{A13}$$

where $\lambda_R = 1/2$ is the convention of Equation (21). Each particle is the center of the element of side Δp that it represents, so the boundary of the discrete disk lies half a spacing beyond its outermost particles.

The offset λ_R is a parameter of the geometry of the discrete disk, not of the SPH approximation, and it is therefore the same for every kernel and branch. With $\lambda_R = 1/2$, the simulated disk has the radius of the disks of the experiments with which it is compared (Section 4.3). An offset chosen by the error it gives would turn the radius into an effective parameter that depends on the kernel and on the smoothing length and is extracted from the very quantity being measured, so that part of the numerical error would be absorbed into the geometry.

To quantify the influence of the radius, λ_R was swept from -0.25 to 1.5 in steps of 0.05, on the same instants and averaged fields as Section 4.2, with the half-width of the loaded arcs kept at $R\psi = \xi\Delta p$ (Figure A8).

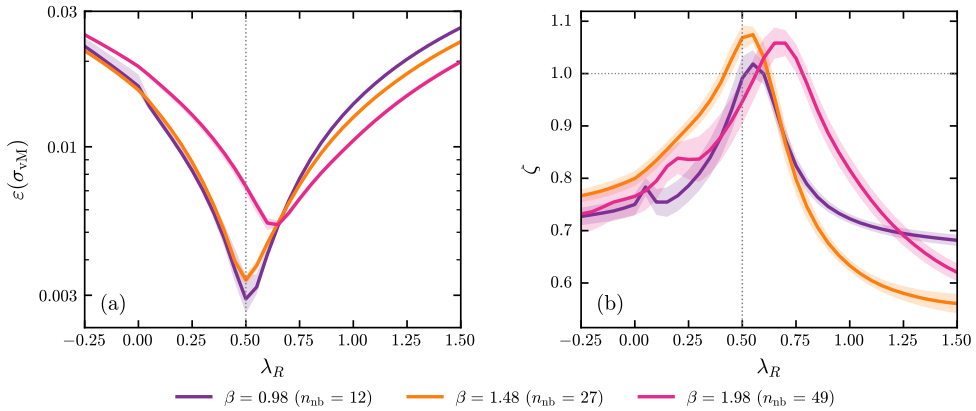


Figure A8. Sensitivity to the radius of the analytical solution, Equation (A13), along the branches $\beta = 0.98$, 1.48 and 1.98 of the Convergence map. (**a**) Error over all zones, $\varepsilon(\sigma_{\mathrm{vM}})$, at $\Delta p = 0.15$ mm on a logarithmic axis, mean of the three kernels, with their range (bands). (**b**) Order of convergence over all zones, ζ, mean of the three kernels, with one standard deviation from a bootstrap over Δp (bands). Dotted: $\lambda_R = 1/2$, Equation (21), and $\zeta = 1$.

The error is the quantity most sensitive to the radius. At $\Delta p = 0.15$ mm, the error at $\lambda_R = 1/2$ is 0.0029, 0.0034 and 0.0073 along the three branches, and $\lambda_R = 0$ and 1 raise it by factors of 2.6–5.6 and 1.4–4.9, respectively, with $\beta = 0.98$ the most sensitive branch and $\beta = 1.98$ the least. An offset of $(\lambda_R - 1/2)\Delta p$ changes the analytical stresses, which scale as $F_{\mathrm{N}}/(\pi R b)$, by a relative amount of order $\Delta p/R = 0.006$ at the finest spacing, comparable to the error itself, which is consistent with the V shape of Figure A8a. The minimum lies at $\lambda_R = 1/2$ for $\beta = 0.98$ and 1.48 and at 0.65 for $\beta = 1.98$, and it moves to larger values as the spacing and β grow, reaching 0.60–0.65, 0.65–0.75 and 0.85–0.95 for $1 \leq \Delta p \leq 2$ mm along the three branches.

Along the same lines, the order of convergence over all zones (Figure A8b) is highest near the minimum of the error and falls on both sides, to 0.75–0.80 at $\lambda_R = 0$ and 0.63–0.82 at $\lambda_R = 1$. With the convention $\lambda_R = 1/2$, the order is 0.99 ± 0.04, 1.07 ± 0.02 and 0.95 ± 0.04 along the three branches, and the highest value reached anywhere in the sweep is only 1.02–1.07, at $\lambda_R = 0.55$–0.65. No choice of radius raises the order over all zones appreciably above 1.

Figure A9 resolves this error by zone, with the zones of Section 4.2.5 defined on the radius of Equation (21), so that only the analytical solution changes with λ_R. At $\Delta p = 0.15$ mm, the minimum of each zone lies at $\lambda_R = 0.50$–0.55 for nearly every exclusion radius along $\beta = 0.98$ and 1.48 and at 0.45–0.50 along the optimal branch, whereas $\beta = 1.98$

places it at 0.60–0.70 in the rim and the interior. The zones with the smallest error are also the most sensitive to the radius, since along $\beta \leq 1.48$ and the optimal branch an offset $\lambda_R = 0$ or 1 raises the error of the interior by factors of 7.9–31.6 and that of the rim by 3.1–18.8, against 1.1–5.4 for the contact zones. Fixing $\lambda_R = 1/2$ is thus consistent with these results, since it lies at or next to the minimum of the error along every branch except $\beta = 1.98$, and the first-order convergence of Section 4.2 is not an artifact of Equation (21).

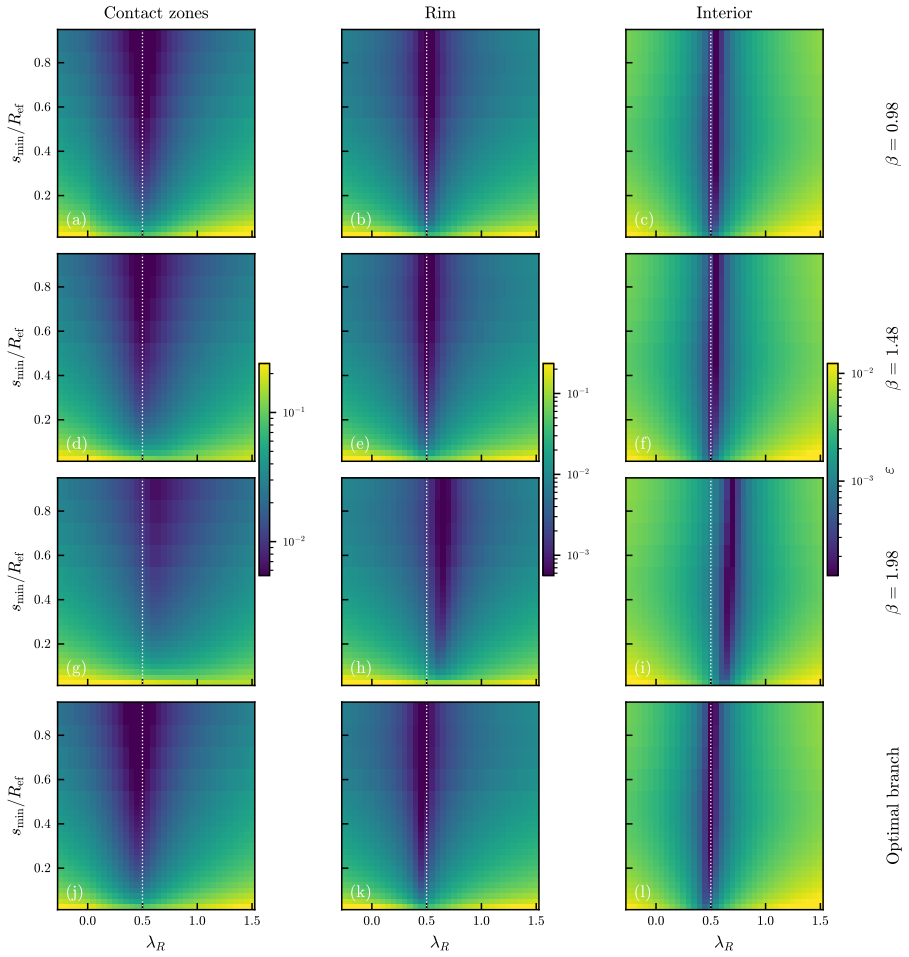


Figure A9. Error of each zone of Section 4.2.5, defined on the radius of Equation (21), at $\Delta p = 0.15$ mm against the offset of the radius, λ_R, and the exclusion radius, $s_{\min}/R_{\text{ef}}$: contact zones, rim and interior (columns), along the branches (**a**–**c**) $\beta = 0.98$, (**d**–**f**) 1.48, (**g**–**i**) 1.98 and (**j**–**l**) the optimal branch of Section 4.2.4, at this spacing $\beta = 1.20$, 1.30 and 1.22 for the cubic spline, Wendland C^2 and hyperbolic kernels; mean of the three kernels, with a logarithmic color scale per column. Dotted: $\lambda_R = 1/2$, Equation (21).

Appendix H. Color Scales of the Simulated Images

The photographs of Lei et al. [36] and Wan et al. [37] are shown cropped to the disk and unaltered inside it. The simulated images show the dark-field intensity $\mathcal{I}$ (Equation (32)), computed with the b_{e} and f_σ of each experiment. As in the small-strain analytical solution, the stress field is drawn on the reference configuration. Each pixel takes the $\sigma_1 - \sigma_2$ of the particle whose initial position is nearest to it.

The intensity is rendered in two steps: (a) a tone curve converts $\mathcal{I}$ to a normalized brightness between 0 and 1, and (b) a color scale extracted from the photograph gives the color of each brightness. Neither step changes the fringe orders: the fringe positions compared in Section 4.3 are read from N_{f} and from the photographs themselves, so they do not depend on how the images are drawn.

Appendix H.1. Location of the Disk

To place the simulated image on the photograph and to convert pixels into millimeters, the disk is located by a least-squares circle fitted to the pixels of its boundary, found by thresholding the color of the disk against the background. The fit is made in three passes:

- First: leaves out the points next to the loading fixtures in the photograph of Lei et al. [36] and under the inset frames in the photographs of Wan et al. [37].
- Second and third: discard the points more than 6 and 2 pixels, respectively, from the circle of the previous pass.

The root-mean-square residual is 0.6 pixels for the photograph of Lei et al. [36] and 0.3 pixels for each photograph of Wan et al. [37]. The fitted circle sets the crop, and its radius in pixels, equated to $R = 25$ mm, sets the pixel size. The loading axis is taken as the vertical of each photograph.

Appendix H.2. Color Scales

The brightness of a pixel is the mean of its red, green and blue channels. Inside $0.9R$, which leaves out the edge of the disk, the brightness of each photograph is normalized from 0 at its 0.5th percentile to 1 at its 99.5th percentile, and this range is divided into 256 levels of equal width. Each level takes the per-channel median color of the pixels in it, and empty levels are interpolated from their neighbors. Figure A10 shows the four scales.

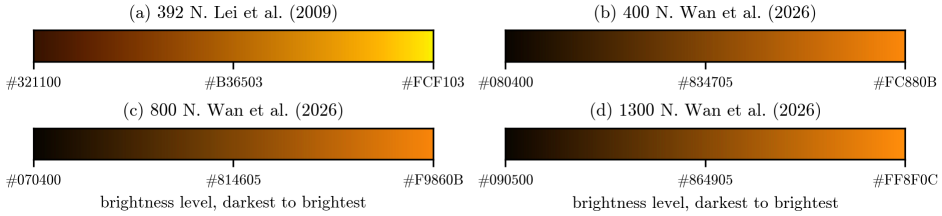


Figure A10. Color scales extracted from the photographs of (**a**) Lei et al. [36], their Figure 3a, and (**b**–**d**) Wan et al. [37], their Figure 2a–c, from the darkest level (left) to the brightest (right).

The three scales of Wan et al. [37] differ from one another by at most 10/255 per channel, and by 1.6/255 on average.

Appendix H.3. Exposure of the Photographs

The experimental photographs of Lei et al. [36] and Wan et al. [37] do not have the same exposure. Table A4 gives, inside $0.9R$, the median normalized brightness of each photograph and the fraction of its pixels with at least one channel at 250 or more, out of 255 (saturated): 39.9% in the photograph of Lei et al. [36] against 0.8–9.5% in the photographs of Wan et al. [37]. The photograph of Lei et al. [36] is overexposed, and its bright fringes are saturated in the red channel.

A linear response with gain g and clipping, with normalized brightness $\min(1, g\,\mathcal{I})$ and g fitted only to match the median brightness of the photograph, supports this. For Lei et al. [36] it gives $g = 1.41$ and clips 39.0% of the simulated disk, close to the 39.9% of saturated pixels of the photograph. For Wan et al. [37], it gives $g = 0.98$–1.06, close to the identity. This model is only a diagnostic to confirm the saturation and is not used to render the images. Clipping paints the whole clipped part of the simulated disk with the brightest color of the scale, whereas in the photograph only the red channel saturates, and the green and blue channels still vary across the bright fringes.

Table A4. Exposure of the photographs and difference from the simulated images, inside $0.9R$: median normalized brightness of each photograph, from 0 (its 0.5th percentile) to 1 (its 99.5th percentile); fraction of pixels with at least one channel at 250/255 or more; gain g of a linear response with clipping; and mean absolute difference in normalized brightness from the simulated image, under the identity and the estimated tone curves.

Photograph	Median Brightness	Saturated Pixels	g	Mean Absolute Difference	
				Identity	Tone Curve
Lei et al. [36], Figure 3a, 392 N	0.794	39.9%	1.41	0.176	0.090
Wan et al. [37], Figure 2a, 400 N	0.603	2.3%	0.98	0.098	0.094
Wan et al. [37], Figure 2b, 800 N	0.484	0.8%	1.06	0.097	0.092
Wan et al. [37], Figure 2c, 1300 N	0.523	9.5%	1.02	0.082	0.081

Appendix H.4. Tone Curves

The simulated images for Wan et al. [37] use the identity tone curve: the normalized brightness equals $\mathcal{I}$, so that $\mathcal{I} = 0$ and 1 take the darkest and brightest levels of the scale. The simulated image for Lei et al. [36] uses a tone curve estimated from its photograph by histogram matching: inside $0.9R$, each quantile of $\mathcal{I}$ over the simulated disk is mapped to the same quantile of the normalized brightness of the photograph, so that the simulated image takes the brightness distribution of the photograph.

The quantiles are matched only between the 5th and 95th percentiles of the photograph, and the curve is held constant beyond them; otherwise the centers of the bright and dark fringes, where $\mathcal{I}$ is nearly flat at 1 or 0, would take the rarest and most extreme colors of the photograph and appear as thin lines. The color bars of Figures 21 and 22 show the color of each intensity after its tone curve, which is why the bar of Figure 21 differs from the scale of Lei et al. [36] in Figure A10.

Appendix H.5. Difference Between Photograph and Simulation

The last two columns of Table A4 compare each photograph with its simulated image pixel by pixel, inside $0.9R$, after placing one on the other with the fitted circle. For Lei et al. [36], the tone curve lowers the mean absolute difference from 0.176 to 0.090, mostly because the photograph is brighter than the simulated image, with a mean difference of $+0.135$ under the identity curve. For Wan et al. [37], the change in the mean absolute difference is at most 0.005, so their images keep the identity curve. What remains comes from the patterns themselves: the positions and widths of the fringes, and the regions next to the contacts, where the fringes are closer together than the photographs or simulations can resolve.

References

1. Lucy, L.B. A numerical approach to the testing of the fission hypothesis. *Astron. J.* **1977**, *82*, 1013–1024. https://doi.org/10.1086/112164.
2. Gingold, R.A.; Monaghan, J.J. Smoothed particle hydrodynamics: Theory and application to non-spherical stars. *Mon. Not. R. Astron. Soc.* **1977**, *181*, 375–389. https://doi.org/10.1093/mnras/181.3.375.
3. Monaghan, J.J. Smoothed particle hydrodynamics. *Rep. Prog. Phys.* **2005**, *68*, 1703–1759. https://doi.org/10.1088/0034-4885/68/8/r01.
4. Liu, G.R.; Liu, M.B. *Smoothed Particle Hydrodynamics: A Meshfree Particle Method*; World Scientific: Singapore, 2003. https://doi.org/10.1142/5340.
5. Zienkiewicz, O.C.; Taylor, R.L.; Zhu, J.Z. *The Finite Element Method: Its Basis and Fundamentals*, 7th ed.; Butterworth-Heinemann: Oxford, UK, 2013. https://doi.org/10.1016/C2009-0-24909-9.
6. Carstensen, C. Convergence of adaptive finite element methods in computational mechanics. *Appl. Numer. Math.* **2009**, *59*, 2119–2130. https://doi.org/10.1016/j.apnum.2008.12.006.

7. Benz, W.; Asphaug, E. Simulations of brittle solids using smooth particle hydrodynamics. *Comput. Phys. Commun.* **1995**, *87*, 253–265. https://doi.org/10.1016/0010-4655(94)00176-3.
8. Monaghan, J.J. SPH without a tensile instability. *J. Comput. Phys.* **2000**, *159*, 290–311. https://doi.org/10.1006/jcph.2000.6439.
9. Gray, J.P.; Monaghan, J.J.; Swift, R.P. SPH elastic dynamics. *Comput. Methods Appl. Mech. Eng.* **2001**, *190*, 6641–6662. https://doi.org/10.1016/S0045-7825(01)00254-7.
10. Bui, H.H.; Fukagawa, R.; Sako, K.; Ohno, S. Lagrangian meshfree particles method (SPH) for large deformation and failure flows of geomaterial using elastic-plastic soil constitutive model. *Int. J. Numer. Anal. Methods Geomech.* **2008**, *32*, 1537–1570. https://doi.org/10.1002/nag.688.
11. Kee, M.H.; Um, K.; Kang, H.; Han, J. An Optimization-based SPH Solver for Simulation of Hyperelastic Solids. *Comput. Graph. Forum* **2023**, *42*, 225–233. https://doi.org/10.1111/cgf.14756.
12. Antoci, C.; Gallati, M.; Sibilla, S. Numerical simulation of fluid-structure interaction by SPH. *Comput. Struct.* **2007**, *85*, 879–890. https://doi.org/10.1016/j.compstruc.2007.01.002.
13. Bui, H.H.; Nguyen, G.D. A coupled fluid-solid SPH approach to modelling flow through deformable porous media. *Int. J. Solids Struct.* **2017**, *125*, 244–264. https://doi.org/10.1016/j.ijsolstr.2017.06.022.
14. Bui, H.H.; Nguyen, G.D. Smoothed particle hydrodynamics (SPH) and its applications in geomechanics: From solid fracture to granular behaviour and multiphase flows in porous media. *Comput. Geotech.* **2021**, *138*, 104315. https://doi.org/10.1016/j.compgeo.2021.104315.
15. Mehra, V.; Chaturvedi, S. High velocity impact of metal sphere on thin metallic plates: A comparative smooth particle hydrodynamics study. *J. Comput. Phys.* **2006**, *212*, 318–337. https://doi.org/10.1016/j.jcp.2005.06.020.
16. Swegle, J.W.; Attaway, S.W.; Heinstein, M.W.; Mello, F.J.; Hicks, D.L. *An Analysis of Smoothed Particle Hydrodynamics*; Technical Report SAND-93-2513; Sandia National Labs.: Albuquerque, NM, USA, 1994. https://doi.org/10.2172/10159839.
17. Chen, J.K.; Beraun, J.E.; Jih, C.J. An improvement for tensile instability in smoothed particle hydrodynamics. *Comput. Mech.* **1999**, *23*, 279–287. https://doi.org/10.1007/s004660050409.
18. Chen, J.K.; Beraun, J.E.; Jih, C.J. Completeness of corrective smoothed particle method for linear elastodynamics. *Comput. Mech.* **1999**, *24*, 273–285. https://doi.org/10.1007/s004660050516.
19. Belytschko, T.; Guo, Y.; Liu, W.K.; Xiao, S.P. A unified stability analysis of meshless particle methods. *Int. J. Numer. Methods Eng.* **2000**, *48*, 1359–1400. https://doi.org/10.1002/1097-0207(20000730)48:9<1359::AID-NME829>3.0.CO;2-U.
20. Vignjevic, R.; Campbell, J.; Libersky, L. A treatment of zero-energy modes in the smoothed particle hydrodynamics method. *Comput. Methods Appl. Mech. Eng.* **2000**, *184*, 67–85. https://doi.org/10.1016/S0045-7825(99)00441-7.
21. Ganzenmüller, G.C. An hourglass control algorithm for Lagrangian Smooth Particle Hydrodynamics. *Comput. Methods Appl. Mech. Eng.* **2015**, *286*, 87–106. https://doi.org/10.1016/j.cma.2014.12.005.
22. Zhu, Q.; Hernquist, L.; Li, Y. Numerical Convergence In Smoothed Particle Hydrodynamics. *Astrophys. J.* **2015**, *800*, 6. https://doi.org/10.1088/0004-637X/800/1/6.
23. Sigalotti, L.G.; Klapp, J.; Rendón, O.; Vargas, C.A.; Peña-Polo, F. On the kernel and particle consistency in smoothed particle hydrodynamics. *Appl. Numer. Math.* **2016**, *108*, 242–255. https://doi.org/10.1016/j.apnum.2016.05.007.
24. Zhang, C.; Zhu, Y.j.; Wu, D.; Adams, N.A.; Hu, X. Smoothed particle hydrodynamics: Methodology development and recent achievement. *J. Hydrodyn.* **2022**, *34*, 767–805. https://doi.org/10.1007/s42241-022-0052-1.
25. Gotoh, H.; Khayyer, A.; Shimizu, Y. Entirely Lagrangian meshfree computational methods for hydroelastic fluid-structure interactions in ocean engineering—Reliability, adaptivity and generality. *Appl. Ocean Res.* **2021**, *115*, 102822. https://doi.org/10.1016/j.apor.2021.102822.
26. Ying, H.; Xu, J.; Zhu, C. SPH modeling of soil structure interactions using a novel non-local contact method. *Comput. Geotech.* **2025**, *184*, 107272. https://doi.org/10.1016/j.compgeo.2025.107272.
27. Leroch, S.; Varga, M.; Eder, S.J.; Vernes, A.; Rodriguez Ripoll, M.; Ganzenmüller, G. Smooth particle hydrodynamics simulation of damage induced by a spherical indenter scratching a viscoplastic material. *Int. J. Solids Struct.* **2016**, *81*, 188–202. https://doi.org/10.1016/j.ijsolstr.2015.11.025.
28. Zhou, M.; Fang, Q.; Peng, C. A mortar segment-to-segment contact method for stabilized total-Lagrangian smoothed particle hydrodynamics. *Appl. Math. Model.* **2022**, *107*, 20–38. https://doi.org/10.1016/j.apm.2022.02.022.
29. Castro, F.J.; Radl, S. A combined SPH-DEM approach for extremely deformed granular packings: Validation and compression tests. *Comput. Part. Mech.* **2024**, *11*, 185–196. https://doi.org/10.1007/s40571-023-00616-8.
30. Sigalotti, L.G.; Rendón, O.; Klapp, J.; Vargas, C.A.; Cruz, F. A new insight into the consistency of the SPH interpolation formula. *Appl. Math. Comput.* **2019**, *356*, 50–73. https://doi.org/10.1016/j.amc.2019.03.018.
31. Cao, X.; Zhou, J.; Xu, H.; Song, D.; Miao, C. An SPH model reconstruction framework with fragment mapping method for multiplate structure hypervelocity impact simulation. *Adv. Space Res.* **2025**, *75*, 8140–8157. https://doi.org/10.1016/j.asr.2025.03.047.

32. Liu, M.; Zhang, Z. Smoothed particle hydrodynamics (SPH) for modeling fluid-structure interactions. *Sci. China Phys. Mech. Astron.* **2019**, *62*, 984701. https://doi.org/10.1007/s11433-018-9357-0.
33. Islam, M.R.I.; Peng, C. A Total Lagrangian SPH method for modelling damage and failure in solids. *Int. J. Mech. Sci.* **2019**, *157–158*, 498–511. https://doi.org/10.1016/j.ijmecsci.2019.05.003.
34. Douillet-Grellier, T.; Pramanik, R.; Pan, K.; Albaiz, A.; Jones, B.D.; Williams, J.R. Development of stress boundary conditions in smoothed particle hydrodynamics (SPH) for the modeling of solids deformation. *Comput. Part. Mech.* **2017**, *4*, 451–471. https://doi.org/10.1007/s40571-016-0137-0.
35. Hondros, G. The evaluation of Poisson's ratio and the modulus of materials of a low tensile resistance by the Brazilian (indirect tensile) test with particular reference to concrete. *Aust. J. Appl. Sci.* **1959**, *10*, 243–268.
36. Lei, Z.; Yun, H.; Kang, Y. Automatic evaluation of photoelastic fringe constant by the nonlinear least-squares method. *Opt. Laser Technol.* **2009**, *41*, 985–989. https://doi.org/10.1016/j.optlastec.2009.04.010.
37. Wan, C.; Dai, B.; Yang, M.; Yang, S.; Fu, G.; Dong, S.; Zheng, J.; Ren, Z.; Ju, Y. Full-field digital photoelastic quantification of principal stress difference under continuous loading: An analytical disk benchmark. *Opt. Laser Technol.* **2026**, *203*, 116288. https://doi.org/10.1016/j.optlastec.2026.116288.
38. Johnson, K.L. *Contact Mechanics*; Cambridge University Press: Cambridge, UK, 1985. https://doi.org/10.1017/CBO9781139171731.
39. Crespo, A.J.C.; Domínguez, J.M.; Rogers, B.D.; Gómez-Gesteira, M.; Longshaw, S.; Canelas, R.; Vacondio, R.; Barreiro, A.; García-Feal, O. DualSPHysics: Open-source parallel CFD solver based on Smoothed Particle Hydrodynamics (SPH). *Comput. Phys. Commun.* **2015**, *187*, 204–216. https://doi.org/10.1016/j.cpc.2014.10.004.
40. Crespo, A.C.; Dominguez, J.M.; Barreiro, A.; Gómez-Gesteira, M.; Rogers, B.D. GPUs, a new tool of acceleration in CFD: Efficiency and reliability on smoothed particle hydrodynamics methods. *PLoS ONE* **2011**, *6*, e20685. https://doi.org/10.1371/journal.pone.0020685.
41. Domínguez, J.M.; Crespo, A.J.C.; Gómez-Gesteira, M.; Marongiu, J.C. Neighbour lists in smoothed particle hydrodynamics. *Int. J. Numer. Methods Fluids* **2011**, *67*, 2026–2042. https://doi.org/10.1002/fld.2481.
42. Bonet, J.; Wood, R.D. *Nonlinear Continuum Mechanics for Finite Element Analysis*, 2nd ed.; Cambridge University Press: Cambridge, UK, 2008. https://doi.org/10.1017/CBO9780511755446.
43. Monaghan, J.J. Simulating Free Surface Flows with SPH. *J. Comput. Phys.* **1994**, *110*, 399–406. https://doi.org/10.1006/jcph.1994.1034.
44. Monaghan, J.J. Smoothed Particle Hydrodynamics. *Annu. Rev. Astron. Astrophys.* **1992**, *30*, 543–574. https://doi.org/10.1146/annurev.aa.30.090192.002551.
45. Liu, M.B.; Liu, G.R. Restoring particle consistency in smoothed particle hydrodynamics. *Appl. Numer. Math.* **2006**, *56*, 19–36. https://doi.org/10.1016/j.apnum.2005.02.012.
46. O'Connor, J.; Rogers, B.D. A fluid–structure interaction model for free-surface flows and flexible structures using smoothed particle hydrodynamics on a GPU. *J. Fluids Struct.* **2021**, *104*, 103312. https://doi.org/10.1016/j.jfluidstructs.2021.103312.
47. Courant, R.; Friedrichs, K.; Lewy, H. Über die partiellen Differenzengleichungen der mathematischen Physik. *Math. Ann.* **1928**, *100*, 32–74. https://doi.org/10.1007/BF01448839.
48. Morris, J.P.; Fox, P.J.; Zhu, Y. Modeling Low Reynolds Number Incompressible Flows Using SPH. *J. Comput. Phys.* **1997**, *136*, 214–226. https://doi.org/10.1006/jcph.1997.5776.
49. Monaghan, J.J.; Lattanzio, J.C. A refined particle method for astrophysical problems. *Astron. Astrophys.* **1985**, *149*, 135–143.
50. Wendland, H. Piecewise polynomial, positive definite and compactly supported radial functions of minimal degree. *Adv. Comput. Math.* **1995**, *4*, 389–396. https://doi.org/10.1007/BF02123482.
51. Yang, X.F.; Liu, M.B. Improvement on stress instability in smoothed particle hydrodynamics. *Acta Phys. Sin.* **2012**, *61*, 224701. https://doi.org/10.7498/aps.61.224701. (In Chinese)
52. Wissing, R.; Quinn, T.; Keller, B.; Wadsley, J.; Shen, S. Optimized smoothing kernels for smoothed particle hydrodynamics. *Astron. Astrophys.* **2026**, *706*, A73. https://doi.org/10.1051/0004-6361/202556909.
53. Micro-Measurements (Vishay Precision Group). PhotoStress® Coatings: PhotoStress Coating Materials and Adhesives. 2015. Document No. 11222, Revision 06-Aug-2015. Available online: https://docs.micro-measurements.com/?id=2539 (accessed on 1 October 2026).
54. Stratasys Ltd. Data Sheet: VeroClear, Rigid Transparent PolyJet Material, 2020. MDS_PJ_VeroClear_0320a. Available online: https://www.stratasys.com/siteassets/materials/materials-catalog/polyjet-materials/veroclear/mds_pj_veroclear_0320a.pdf (accessed on 1 October 2026).
55. Sadd, M.H. *Elasticity: Theory, Applications, and Numerics*; Elsevier Butterworth–Heinemann: Burlington, MA, USA, 2005.
56. Huber, P.J.; Ronchetti, E.M. *Robust Statistics*, 2nd ed.; Wiley: Hoboken, NJ, USA, 2009. https://doi.org/10.1002/9780470434697.
57. Timoshenko, S.P.; Goodier, J.N. *Theory of Elasticity*, 3rd ed.; McGraw-Hill: New York, NJ, USA, 1970.

58. Chen, J.K.; Beraun, J.E.; Carney, T.C. A corrective smoothed particle method for boundary value problems in heat conduction. *Int. J. Numer. Methods Eng.* **1999**, *46*, 231–252.
59. Scott, R. Finite element convergence for singular data. *Numer. Math.* **1973**, *21*, 317–327.
60. Köppl, T.; Wohlmuth, B. Optimal a priori error estimates for an elliptic problem with Dirac right-hand side. *SIAM J. Numer. Anal.* **2014**, *52*, 1753–1769.
61. Amidror, I. *The Theory of the Moiré Phenomenon, Volume I: Periodic Layers*, 2nd ed.; Computational Imaging and Vision; Springer: London, UK, 2009; Volume 38. https://doi.org/10.1007/978-1-84882-181-1.
62. Shannon, C.E. Communication in the presence of noise. *Proc. IRE* **1949**, *37*, 10–21. https://doi.org/10.1109/JRPROC.1949.232969.
63. Markides, C.F.; Pazis, D.N.; Kourkoulis, S.K. Closed full-field solutions for stresses and displacements in the Brazilian disk under distributed radial load. *Int. J. Rock Mech. Min. Sci.* **2010**, *47*, 227–237. https://doi.org/10.1016/j.ijrmms.2009.11.006.
64. Markides, C.F.; Pazis, D.N.; Kourkoulis, S.K. Influence of Friction on the Stress Field of the Brazilian Tensile Test. *Rock Mech. Rock Eng.* **2011**, *44*, 113–119. https://doi.org/10.1007/s00603-010-0115-4.
65. Dehnen, W.; Aly, H. Improving convergence in smoothed particle hydrodynamics simulations without pairing instability. *Mon. Not. R. Astron. Soc.* **2012**, *425*, 1068–1082. https://doi.org/10.1111/j.1365-2966.2012.21439.x.
66. Truman, C.E.; Sackfield, A.; Hills, D.A. Contact mechanics of wedge and cone indenters. *Int. J. Mech. Sci.* **1995**, *37*, 261–275. https://doi.org/10.1016/0020-7403(94)00066-S.

Disclaimer/Publisher's Note: The statements, opinions and data contained in all publications are solely those of the individual author(s) and contributor(s) and not of MDPI and/or the editor(s). MDPI and/or the editor(s) disclaim responsibility for any injury to people or property resulting from any ideas, methods, instructions or products referred to in the content.